

**The Subaru/XMM-Newton Deep Survey (SXDS). IV.
Evolution of Ly α Emitters from $z = 3.1$ to 5.7 in the 1 deg² Field:
Luminosity Functions and AGN¹**

Masami Ouchi ^{2,3,4,5}, Kazuhiro Shimasaku ⁶, Masayuki Akiyama ⁷, Chris Simpson ⁸,
Tomoki Saito ⁹, Yoshihiro Ueda ¹⁰, Hisanori Furusawa ⁷, Kazuhiro Sekiguchi ¹¹,
Toru Yamada ¹², Tadayuki Kodama ¹¹, Nobunari Kashikawa ¹¹,
Sadanori Okamura ⁶, Masanori Iye ¹¹, Tadafumi Takata ¹¹,
Michitoshi Yoshida ¹³, and Makiko Yoshida ⁶

ABSTRACT

We present luminosity functions (LFs) and various properties of Ly α emitters (LAEs) at $z = 3.1$, 3.7, and 5.7, in a 1 deg² sky of the Subaru/*XMM – Newton*

¹Based on data collected at Subaru Telescope, which is operated by the National Astronomical Observatory of Japan.

²Space Telescope Science Institute, 3700 San Martin Drive, Baltimore, MD 21218, USA

³Observatories of the Carnegie Institution of Washington, 813 Santa Barbara St., Pasadena, CA 91101, USA; ouchi_at_ociw.edu.

⁴Hubble Fellow

⁵Carnegie Fellow

⁶Department of Astronomy, School of Science, University of Tokyo, Tokyo 113-0033, Japan

⁷Subaru Telescope, National Astronomical Observatory, 650 N.A'ohoku Place, Hilo, HI 96720, USA

⁸Astrophysics Research Institute, Liverpool John Moores University, Twelve Quays House, Egerton Wharf, Birkenhead CH41 1LD, UK

⁹Physics Department, Graduate School of Science, Ehime University, 2-5 Bunkyou, Matuyama, 790-8577, Japan

¹⁰Department of Astronomy, Kyoto University, Kyoto 606-8502, Japan

¹¹National Astronomical Observatory, Tokyo 181-8588, Japan

¹²Astronomical Institute, Graduate School of Science, Tohoku University, Aramaki, Aoba, Sendai 980-8578, Japan

¹³Okayama Astrophysical Observatory, National Astronomical Observatory, Kamogata, Okayama 719-0232, Japan

Deep Survey (SXDS) Field. We obtain a photometric sample of 858 LAE candidates based on deep Subaru/Suprime-Cam imaging data, and a spectroscopic sample of 84 confirmed LAEs from Subaru/FOCAS and VLT/VIMOS spectroscopy in a survey volume of $\sim 10^6$ Mpc³ with a limiting Ly α luminosity of $\sim 3 \times 10^{42}$ erg s⁻¹. We derive the LFs of Ly α and UV-continuum ($\simeq 1500$ Å) for each redshift, taking into account the statistical error and the field-to-field variation. We find that the *apparent* Ly α LF shows no significant evolution between $z = 3.1$ and 5.7 within factors of 1.8 and 2.7 in L^* and ϕ^* , respectively. On the other hand, the UV LF of LAEs increases from $z = 3.1$ to 5.7 , indicating that galaxies with Ly α emission are more common at earlier epochs. We identify six LAEs with AGN activities from our spectra combined with VLA, Spitzer, and XMM-Newton data. Among the photometrically selected LAEs at $z = 3.1$ and 3.7 , only $\simeq 1\%$ show AGN activities, while the brightest LAEs with $\log L(\text{Ly}\alpha) \gtrsim 43.4 - 43.6$ erg s⁻¹ appear to always host AGNs. Our LAEs are bluer in UV-continuum color than dropout galaxies, suggesting lower extinction and/or younger stellar populations. Our stacking analyses provide upper limits to the radio luminosity and the $f_{\text{HeII}}/f_{\text{Ly}\alpha}$ line fraction, and constrain the hidden star formation (+low-luminosity AGN) and the primordial population in LAEs.

Subject headings: galaxies: formation — galaxies: high-redshift — cosmology: observations

1. Introduction

Ly α emitters (LAEs) provide clues to evolution and formation of galaxies. Most of LAEs are known as star-forming galaxies at $z \simeq 2 - 7$ with a faint-UV continuum, but a prominent Ly α emission line, which are produced by star-forming activities with a typical star-formation rate of $\sim 1 - 10 M_{\odot} \text{yr}^{-1}$ (e.g., Cowie & Hu 1998; Ouchi et al. 2003; Gawiser et al. 2006; Pirzkal et al. 2006). LAEs are believed to have a negligible fraction of AGN activities, since an X-ray detection has been reported for only one LAE at $z \sim 3$ (Gawiser et al. 2006, see also Wang et al. 2004). The strong Ly α emission and a blue UV continuum color imply a young metal-poor star-forming galaxies (Malhotra & Rhoads 2002; Finkelstein et al. 2007). Recent infrared observations and population synthesis models indicate that typical stellar mass of LAEs is as small as $\sim 10^8 - 10^9 M_{\odot}$ and that the stellar age is as young as $\lesssim 10$ Myr (Pirzkal et al. 2006; see also Chary et al. 2005; Gawiser et al. 2006; Lai et al. 2006; Nilsson et al. 2007). LAEs show a compact UV morphology with a size smaller than 1 kpc (Pascarelle, Windhorst, Keel, & Odewahn 1996; Pirzkal et al. 2006). The fraction of LAEs

(or galaxies with a Ly α emission line) increases at faint UV magnitudes (Ouchi et al. 2003; Ando et al. 2006; Shimasaku et al. 2006). These pieces of evidence suggest that LAE samples include a young low-mass population at high- z .

More interestingly, some of LAEs have a Ly α emission line with a large rest-frame equivalent width (EW) of $EW_0 > 240\text{\AA}$ that cannot be explained by a star-formation with a Salpeter IMF (Malhotra & Rhoads 2002; Dawson et al. 2004; Shimasaku et al. 2006). It is reported that about 10-40% of spectroscopically-identified LAEs have an EW_0 of $> 240\text{\AA}$ at $z = 4.5$ (Dawson et al. 2004) and $z = 5.7$ (Shimasaku et al. 2006). The population synthesis models indicate that such large EW objects would have a top heavy IMF, a very poor metallicity and/or a very young age $< 10^7$ yr (Charlot & Fall 1993; Malhotra & Rhoads 2002; Schaerer 2003, see also Kudritzki et al. 2000). Large-EW objects often show a spatially-extended Ly α envelope whose projected size can be as large as $\gtrsim 100$ kpc (Steidel et al. 2000). These objects are referred to as Ly α blobs. Ly α blobs are originally discovered in an overdensity region of Lyman break galaxies (LBGs) at $z \sim 3$ (Steidel et al. 2000; Matsuda et al. 2004, see also Dey et al. 2005). However, recent deep surveys also find Ly α blobs in blank fields (Nilsson et al. 2006; Saito et al. 2006). Some of these Ly α blobs show evidence of AGN activities (Dey et al. 2005), while others are not (Matsuda et al. 2004; Saito et al. 2006). Theoretical studies predict that these large-EW objects with an extended Ly α profile are candidates of cooling clouds (e.g. Yang et al. 2006) and population III galaxies (e.g. Schaerer 2003), which are at the very beginning stage of galaxy formation. Thus, LAEs are keys to understanding the early stage of galaxy formation with less-massive (or dwarf) population some of which include young galaxies even at the very beginning stage of radiating clouds and population III. The studies of LAEs complement the recent work of high- z massive and/or old galaxies (e.g. van Dokkum et al. 2006; Kriek et al. 2006; Daddi et al. 2007).

LAEs are usually identified by a redshifted Ly α emission line that falls in a passband of narrow-band filter (e.g. Hu et al. 2002; Kodaira et al. 2003), tuned at $z \sim 3$ up to $z \sim 9$ (e.g. Iye et al. 2006; Willis et al. 2006). Recent blank-field slitless, multi-slit, and IFU spectroscopy also searched for LAEs (Martin & Sawicki 2004; Tran et al. 2004; Kurk et al. 2004; van Breukelen et al. 2005; Martin et al. 2006). Blind spectroscopy in cluster regions yielded candidates of gravitationally lensed LAEs that enable us to study intrinsically faint LAEs (Ellis et al. 2001; Santos et al. 2004; Stark et al. 2007). The numbers of photometrically and spectroscopically identified LAEs are now over several hundreds (e.g. Hu et al. 2002; Ouchi et al. 2003; Malhotra & Rhoads 2004; Taniguchi et al. 2005; Shimasaku et al. 2006; Kashikawa et al. 2006; Venemans et al. 2007), and the numbers are increasing by recent and on-going wide-field projects such as WFIAS (Westra et al. 2005, 2006), MUSYC (Gawiser et al. 2006; Gronwall et al. 2007), Hawaii (see Hu & Cowie 2006), and SSA22 sur-

veys (Nakamura et al. in preparation).

In spite of increasing observational data of LAEs, evolution of LAEs is not clearly understood. Most of observational results agree that the LF of Ly α luminosity shows no evolution at $z = 3 - 6$ within the errors of measurements. (e.g. Rhoads & Malhotra 2001; Ouchi et al. 2003; Hu et al. 2004; Yamada et al. 2005; van Breukelen et al. 2005; Shimasaku et al. 2006; Tapken et al. 2006; Murayama et al. 2007; c.f. Maier et al. 2003). Although these measurements qualitatively agree, the constraints on the LF evolution are weak, due to the small statistics and field variations. Indeed, the presence of large-scale structures of LAEs has been reported (Shimasaku et al. 2003; Ouchi et al. 2005a) at these redshifts, which produce a significant source gradient even within a 0.2 deg^2 field (Ouchi et al. 2003; Hu et al. 2004). Note that the narrow-band LAE studies observe a thin slice ($\Delta z = 0.1$) of the Universe whose survey volume is about 1/10 of that of dropout or LBG surveys ($\Delta z = 1$) at a given search area (see e.g. Ouchi et al. 2004b). We need to obtain statistical properties of LAEs including clustering with a good accuracy. Moreover, we should investigate rare populations of LAEs with a large EW or AGN, which are essential for understanding galaxy formation and its relation to the formation of massive black holes.

Here we carry out a systematic wide-field narrow-band survey for LAEs at $z = 3.1 - 6.6$ in the wide-field (1 deg^2) Subaru/XMM-Newton Deep Field (SXDS) that is covered by deep Subaru optical images ($i'[5\sigma] = 27.0$; Furusawa in preparation) and the near-infrared images of UKIDSS/Ultra Deep Survey (UKIDSS/UDS; Lawrence et al. 2006) as well as VLA (Simpson et al. 2006a), XMM-Newton (Ueda et al. in preparation), and Spitzer (Lonsdale et al. 2003). Except for the data of $z = 6.6$ LAEs, we have completed narrow-band imaging for $z = 3.1, 3.7$ and 5.7 LAEs. In this paper, we show properties of LAEs at $z = 3.1 - 5.7$. Note that the first results from the $z = 5.7$ data have been presented in Ouchi et al. (2005a). Our systematic survey will not only put strong constraints on properties of LAEs at $z = 3.1 - 5.7$, but also give the useful baselines to be compared with higher redshift LAEs for studying reionization of the Universe (Malhotra & Rhoads 2004; Kashikawa et al. 2006).

We show photometric and spectroscopic data, and make the spectroscopic samples in Section 2. We define the photometric samples of LAEs in Section 3. The AGNs in our LAE samples are presented in Section 4. We derive LFs of LAEs and investigate evolution of the LF in Section 5. In Section 6, we address the properties of LAEs, such as EW, UV-continuum slope, star-formation rate, and AGN activity. We discuss our results and summarize them in Sections 7 and 8, respectively. We will present clustering and stellar population of these LAEs in two companion papers of Ouchi et al. (in preparation) and Ono et al. (in preparation).

Throughout this paper, magnitudes are in the AB system (Oke 1974; Fukugita, Shimasaku, & Ichikawa 1995). EW is presented in rest frame (i.e. EW_0). The values for the cosmological parameters adopted in this paper are: $(h, \Omega_m, \Omega_\Lambda, n) = (0.7, 0.3, 0.7, 1.0)$.

2. Observations and Data Reduction

2.1. Imaging Data

We carried out narrow-band imaging with Subaru/Suprime-Cam (Miyazaki et al. 2002; see also Iye et al. 2004) in 7 nights during 2003 September 28-30, October 22-24, and October 26. We summarize details of these observations as well as image qualities in Table 1. We obtained narrow-band images with three bands, $NB503$ ($\lambda_c = 5029\text{\AA}$, $\Delta\lambda = 74\text{\AA}$), $NB570$ ($\lambda_c = 5703\text{\AA}$, $\Delta\lambda = 69\text{\AA}$), and $NB816$ ($\lambda_c = 8150\text{\AA}$, $\Delta\lambda = 120\text{\AA}$). We show the response curves of our narrow-band and broad-band filters in Figure 1. These response curves include atmospheric absorption, quantum efficiency, and transmittance of optical elements of the telescope and instrument. We have chosen these three narrow bands to identify LAEs at $z \simeq 3.1, 3.7,$ and 5.7 . Note that there are no strong OH sky lines within the passbands of these narrow-band filters (Figure 1). Since Suprime-Cam has a field-of-view (FoV) of 0.255 deg^2 , the 1 deg^2 area of SXDS is covered with 5 pointings of Suprime-Cam. These 5 pointings are referred to as SXDS-C (Center), SXDS-N (North), SXDS-S (South), SXDS-E (East), and SXDS-W (West) whose central coordinates are the same as the archival broad-band images of the SXDS project (see Table 1 of Furusawa et al. in preparation). The on-source exposure times of $NB503$, $NB570$, and $NB816$ filters are typically $1.2 - 1.5$, $1.2 - 1.5$, and $4.0 - 5.7$ hours per pointing, respectively. The observational condition was photometric and clear throughout the first 6 nights, and especially good in three nights for $NB816$ data in 2003 September 28-30. The seeing size was typically $0''.4 - 0''.6$ and $0''.5 - 1''.0$ for 2003 September 28-30, and October 22-24 and 26, respectively. In addition to these narrow-band data, we use archival data of very deep broad-band (B, V, R, i' and z') images of the SXDS project. The narrow-band data are reduced with the Suprime-Cam Deep field REDuction package (SDFRED; Yagi et al. 2002; Ouchi et al. 2004a). With the standard parameter sets of SDFRED, we perform bias subtraction, flat-fielding, distortion+atmospheric-dispersion corrections, sky subtraction, image alignments, and stacking. Before stacking, we mask out bad data areas such as dead pixels and satellite trails. Cosmic rays are removed in the process of stacking with the rejected-mean algorithm. The 5σ sky noise of the reduced narrow-band images are $NB503 \simeq 25.3$, $NB570 \simeq 24.9$, and $NB816 \simeq 26.0$ in a $2''.0$ -diameter circular aperture (see Ouchi et al. 2005a for the $NB816$ data). Typical PSF sizes of images after reduction are $\simeq 0''.8$ in FWHM.

We do not use, either contaminated areas with halos of bright stars and CCD blooming or low signal-to-noise (S/N) regions located around the edge of the FoV, which are caused by dithering. After we reject these bad areas, the effective total areas are 0.983, 0.965, and 1.034 deg² for *NB503*, *NB570*, and *NB816* images, respectively. These effective areas correspond to the survey volumes of 7.0×10^5 Mpc³ ($z = 3.1$), 6.1×10^5 Mpc³ ($z = 3.7$), and 9.2×10^5 Mpc³ ($z = 5.7$), if we assume a simple top-hat selection function of LAEs whose redshift distribution is defined by the FWHM of narrow-band filters.

During the observations, we took images of spectrophotometric standard stars of GD50 and GD71 in *NB503* and *NB816* bands and GD248, G93-48, and GD50 in *NB570* band (Oke 1990; Bohlin et al. 1995). These standard stars were observed 1 – 4 time(s), when the sky was thought to be photometric. We calculate photometric zero-points from photometry of standard stars. We check these photometric zero points with the narrow- and broad-band images by comparing with colors of stellar objects in our field and 175 Galactic stars calculated from spectra given in Gunn & Stryker (1983). We find that the colors of stellar objects in our data are consistent with those of Gunn & Stryker’s stars within 0.01 – 0.05 magnitude. The photometric-zero points thus obtained are regarded as more accurate than 0.05 mag in the entire 1 deg² field.

Our narrow-band images are registered to match the coordinates of SXDS broad-band images based on hundreds of stellar objects commonly detected in both narrow- and broad-band images. The astrometry of our objects is the same as those of SXDS version 1.0 catalog (Furusawa et al. in preparation). The errors in the *relative* positions of objects are $\sim 0''.04$ in r.m.s. The r.m.s accuracy of the *absolute* positions is estimated in Furusawa et al. (in preparation) to be $\sim 0''.2$. After the registration, we homogenize the PSF sizes of broad and narrow-band images, referring to these stellar objects. The PSF sizes of narrow-band images match to those of broad-band images with an accuracy of $\delta\text{FWHM} \simeq 0''.01$.

2.2. Photometric Catalogs

Source detection and photometry are performed using SExtractor (Bertin & Arnouts 1996). We measure both MAG_AUTO of SExtractor and 2''.0-diameter aperture magnitudes. We adopt MAG_AUTO as total magnitudes, while we use a 2''.0-diameter aperture magnitude to measure colors of objects in order to obtain colors of faint objects with a good signal-to-noise ratio. We make *NB503*-, *NB570*-, and *NB816*-detection catalogs, and limit to $NB503 < 25.3$, $NB570 < 24.7$, and $NB816 < 26.0$, respectively, that correspond to about 5σ detection limits on a 2''.0-diameter aperture. Our *NB503*-, *NB570*-, and *NB816*-detection catalogs contain 98,907, 64,362, and 278,458, respectively. We correct the magni-

tudes of objects for Galactic extinction of $E(B - V) = 0.020$ (Schlegel, Finkbeiner, & Davis 1998).

2.3. Spectroscopic Data

We carried out spectroscopic follow-up observations for our LAE candidates with Faint Object Camera and Spectrograph (FOCAS; Kashikawa et al. 2002) of Subaru and Visible Multi-Object Spectrograph (VIMOS; LeFevre et al. 2003) of VLT.

The FOCAS observations were carried out in the MOS mode on 2003 December 20, 23, and 25, 2004 October 17, November 9, 11, and 2005 November 2-3. The sky was clear during these observations, except on 2005 November 3. Since these observations were conducted under the SXDS project and the Subaru open use programs of Akiyama et al., Yamada et al., and Sekiguchi et al., the slits of our objects shared the eight MOS masks with those of the other targets. The on-source exposure time ranges typically from 7200 to 10800 seconds. These spectroscopic observations were made with SY47 order-cut filter and 300 lines mm^{-1} grating having the blaze wavelengths of 5500Å (300B) with a slit width of $0''.8$. The spectral range and resolution are $\lambda = 4900 - 9400\text{Å}$ and $\lambda/\Delta\lambda \simeq 500 - 1000$, respectively.

The VIMOS spectroscopy was conducted in the programs of Simpson et al. (in preparation) and Saito et al. (2007). The Simpson et al.'s observations were made between UT 2004 Dec 17 and UT 2006 Jan 2. The medium resolution grating was used with the GG475 order sorting filter, which provides a spectral resolution $\lambda/\Delta\lambda \approx 580$ over the wavelength range 4800 Å–1 μm . Each mask was observed with $1 \times 2700 + 2 \times 1350$ second exposures, often on separate nights. Data reduction is described in detail in Simpson et al. (in preparation) but broadly followed the standard pipeline method. The Saito et al.'s observations were carried out in 2004 November 6 to 9. The HR-Orange grism and the GG435 order-cut filter were used for MOS masks with a slit width of $1''.0$. The spectral resolution of these observations is $R \approx 2160\text{Å}$, which is $> 2 - 4$ times higher than the other observations of our spectroscopy. The effective on-source integration time was 4-7 hours. Data reduction and details of observations are described in Saito et al. (2007).

2.4. Spectroscopic Catalogs and Samples

We took spectra for objects with colors similar to LAEs which show a narrow-band excess and a continuum break in blue band. We observed 128 and 29 objects at $z = 3.1/3.7$ and 5.7, respectively. Since we share the MOS masks with targets from the other projects, we had

tight constraints on our target selection for spectroscopy. Thus, we include unreliable LAE candidates with colors similar to foreground objects and very faint narrow-band magnitudes, some of which potentially have a bright Ly α emission line redshifted to the edge of passband of our narrow band. As a result, we have identified line emitters from 60% of our targets. Although the success rate of identification is not high by the constraints of our spectroscopy, this target selection allows us to obtain spectra for objects in wide color and magnitude ranges.

In addition to these spectra for our LAEs, we use the SXDS version 1.0 spectroscopic data taken with Subaru/FOCAS and AAO/2dF. The combination of these and our data provide 3,233 spectroscopic redshifts in our field (Akiyama et al. in preparation). We refer this catalog to estimate the contamination rates of our LAE sample in Section 3.2. Figure 2 presents the redshift distribution of our sources from the combined catalogs.

We have investigated our spectra with an emission line at the passbands of our narrow bands. We carefully check the possibilities of low- z [OII], [OIII], and H α emitters. For $z = 3.1$ LAE candidates with an emission at $\sim 5000\text{\AA}$, we look at the spectrum at the wavelengths of an H α line of a $z = 0.004$ [OIII] emitter and H α /[OIII] lines of a $z = 0.3$ [OII] emitter. Similarly, the possibilities of a $z = 0.1$ [OIII] and a $z = 0.5$ [OII] emitters are examined for $z = 3.7$ LAE candidates. For $z = 5.7$ LAE candidates, our spectra allow us to identify a $z = 0.2$ H α emitter and a $z = 0.6$ [OIII] emitter with corresponding [OII]/[OIII] and [OII] lines, respectively. However, no nebular emission lines enter in the wavelengths of our optical spectra for a $z = 1.2$ [OII] emitter. Because our spectral resolution is not high enough to clearly identify an [OII] doublet, we examine the possibility of an [OII] emitter by the detection of blue continuum in B or V bands whose 2σ upper limits reach very deep magnitudes of $B = 28.7$ and $V = 27.7$. In this way, we discriminate low- z emitters from high- z LAEs. We also visually inspect images and spectra, and remove spurious objects. By these analyses, we have identified 41, 26, and 17 LAEs at $z = 3.1, 3.7, 5.7$. We refer to these 84 LAEs as the spectroscopic samples of LAEs. In Figures 3-5 we show spectra of $z = 3.1 - 5.7$ LAEs, together with snapshots of broad- and narrow-band images. Table 2 summarizes the properties of LAEs with a spectrum. Figure 6 plots the redshift distribution of these spectroscopically-identified LAEs at $z = 3.1, 3.7, \text{ and } 5.7$.

3. Photometric Samples of Ly α Emitters at $z = 3.1 - 5.7$

3.1. Definitions of $z = 3.1, 3.7,$ and 5.7 Ly α Emitters

We plot color-magnitude diagrams in Figure 7 for objects in our photometric and spectroscopic catalogs. Each panel of Figure 7 shows narrow-band excess color and narrow-band magnitude for *NB503*, *NB570*, and *NB816*. Figure 8 presents two-color diagrams based on the *NB503*-, *NB570*-, and *NB816*-detection catalogs, together with colors of model galaxies and Galactic stars. Colors of model objects indicate that LAEs can be isolated from low- z galaxies and Galactic stars by their narrow-band excess of Ly α emission and red continuum colors.

We compare colors of galaxies in our LAE samples with those of the 3,233 spectroscopically-identified objects which include LAEs and foreground/background interlopers. As expected, spectroscopically-identified LAEs are located in the upper-right part of the two-color diagrams.

Based on these color diagrams, we define the selection criteria of three LAE samples:

$$V - NB503 > 1.2 \ \& \ [(V < V_{2\sigma} \ \& \ B - V > 0.5) \ \text{or} \ (V \geq V_{2\sigma} \ \& \ B - V_{2\sigma} > 0.5)] \quad \text{for } z = 3.1 \text{ LAEs,} \quad (1)$$

$$V - NB570 > 1.3 \ \& \ [(V < V_{2\sigma} \ \& \ B - V > 0.7) \ \text{or} \ (V \geq V_{2\sigma} \ \& \ B - V_{2\sigma} > 0.7)] \quad \text{for } z = 3.7 \text{ LAEs,} \quad (2)$$

$$i' - NB816 > 1.2 \ \& \ B > B_{2\sigma} \ \& \ V > V_{2\sigma} \ \& \ [(R < R_{2\sigma} \ \& \ R - i' > 1.0) \ \text{or} \ (R \geq R_{2\sigma})] \quad \text{for } z = 5.7 \text{ LAEs,} \quad (3)$$

where $B_{2\sigma}$, $V_{2\sigma}$, and $R_{2\sigma}$ are 2σ limiting magnitudes of B , V , and R images, i.e. $B = 28.7$, $V = 27.7$, and $R = 28.0$, respectively. With these criteria, we include the objects with no detectable continuum in V (for $z = 3.1$ and 3.7) and i' (for $z = 5.7$). Thus, these photometric samples are complete to the narrow-band magnitude limits, which include all the Ly α emitting objects at these redshifts either with or without a detectable-UV continuum. The narrow-band excess colors, $V - NB503 > 1.2$, $V - NB570 > 1.3$, and $i' - NB816 > 1.2$, isolate an emission line object at each redshift with a flat continuum ($f_\nu = \text{const}$) whose rest-frame EW is greater than $\simeq 45\text{\AA}$. Note that the actual EW limits for our LAE samples are different from $\simeq 45\text{\AA}$, since LAEs do not have a flat continuum, but a continuum break, i.e. Gunn-Peterson trough, between blue and red sides of Ly α emission. Thus, the narrow- and broad-band colors do not provide a clear limit of EWs. We estimate the limits of rest-frame EWs to be approximately $\sim 64\text{\AA}$, $\sim 44\text{\AA}$, $\sim 27\text{\AA}$ for our $z = 3.1, 3.7,$ and 5.7 LAE samples with models of our Monte-Carlo simulations described in Section 5.1.

We apply these selection criteria to our photometric catalogs. We use *NB503*-, *NB570*-, and *NB816*-detection catalogs and find 356, 101, and 401 LAEs at $z = 3.1, 3.7,$ and 5.7 , respectively. In this way, we obtain LAE samples composed of 858 photometrically-identified LAEs in total. We refer to these 858 LAEs as the photometric samples of LAEs, which are

summarized in Table 3. Note that these photometric samples are purely composed of objects satisfying the selection criteria of eq. (1), (2), or (3). Our photometric samples do not include spectroscopically-identified LAEs escaping from the photometric criteria.

Figures 9-11 show surface densities of LAEs. The red circles are the average surface densities. The black points with 5 different symbols indicate the surface densities in 5 sub-fields ($\simeq 0.2 \text{ deg}^2$) of Suprime-Cam, i.e., SXDS-C, -N, -S, -E, -W. The detection completeness is corrected with the simulations described in Section 3.2. For these completeness-corrected points, the difference of surface densities among the five $\simeq 0.2 \text{ deg}^2$ fields are negligible for all narrow-band detected objects, but are as large as a factor of, say, $\simeq 2 - 5$, for LAEs. These large differences probably come from field-to-field variation as well as Poisson errors. We evaluate the field-to-field variation in our survey area, σ_g , with

$$\sigma_g = \sigma_{g:1FoV}(\sigma_{DM}/\sigma_{DM:1FoV}) \quad (4)$$

$$\sigma_{g:1FoV}^2 = [\langle(\Sigma_{g:1FoV} - \bar{\Sigma}_g)^2\rangle - \bar{\Sigma}_g]/\bar{\Sigma}_g^2 \quad (5)$$

where σ_{DM} and $\sigma_{DM:1FoV}$ are the rms fluctuation of dark matter in all the survey volume of 1 deg^2 and Suprime-Cam's 1-FoV volume ($\simeq 0.2 \text{ deg}^2$), respectively. We calculate the fluctuations of dark matter with the power spectrum, adopting the transfer function given by Bardeen, Bond, Kaiser, & Szalay (1986). $\sigma_{g:1FoV}$ is the fluctuation of number density of LAEs for the 1 FoV. $\Sigma_{g:1FoV}$ and $\bar{\Sigma}_g$ are LAE's surface densities of the 1 FoV and the average of survey area.

Since these estimates of field-to-field variation are based on a large but single contiguous field, it is important to check whether our field is located at the sky of an overdense or underdense region. In fact, a large-scale overdensity or underdensity of Ly α sources could also be produced by an inhomogeneous distribution of Ly α absorbers (i.e. neutral hydrogen) along the line of sight.

In Figure 11 we compare the surface densities of our LAEs with those on completely different sky areas but selected with the same *NB816* filter by Shimasaku et al. (2006) and Hu et al. (2004). We find that the surface densities of our $z = 5.7$ LAEs are consistent with those of Shimasaku et al. (2006) and Hu et al. (2004) within the scatters and Poisson errors of our 5 sub-fields. Moreover, Figure 11 shows that Shimasaku et al.'s and Hu et al.'s measurements scatter around our average surface-density curve. Thus, we conclude that our single contiguous 1 deg^2 field has no signature of overdensity or underdensity, and that our 5 sub-fields represent the average field-to-field variation.

In the same manner as the calculations of surface densities, Figure 12 plots color distributions with the uncertainties of field variance for our LAE samples. In Section 5.1, we

compare these color distributions (as well as the surface densities) with those reproduced by our Monte-Carlo simulations, and determine the best-estimates of luminosity function by χ^2 fitting.

3.2. Completeness and Contamination of the Samples

First, we estimate the detection completeness of each narrow-band images, f_{det} , as a function of narrow-band magnitude. We distribute 7875 artificial objects that mimic LAEs on our original 1 deg² images after adding photon noise, and detect them in the same manner as for the detection of our LAE catalogs with SExtractor. We repeat this process 10 times, and compute the detection fraction. We find that the detection completeness is typically $\gtrsim 80 - 90\%$ for relatively luminous sources which are 0.75 magnitude brighter than the magnitude cuts of our samples (i.e. $NB503 \leq 24.55$, $NB570 \leq 23.95$, and $NB816 \leq 25.25$). The detection completeness is $\gtrsim 50 - 60\%$ even for the faintest magnitude bin of our samples (i.e. $NB503 = 24.8 - 25.3$, $NB570 = 24.2 - 24.7$, and $NB816 = 25.5 - 26.0$).

Second, we estimate the contamination of our photometric LAE samples, which we need to consider in calculating the LF. We use our spectroscopic catalog of 3,233 objects (Section 2.4). We define the contamination fraction, f_{cont} , with

$$f_{\text{cont}} = 1 - N_{\text{LAE}}^{\text{in}}/N_{\text{all}}^{\text{in}} \quad (6)$$

where $N_{\text{LAE}}^{\text{in}}$ and $N_{\text{all}}^{\text{in}}$ are the numbers of spectroscopically-identified LAEs and all spectroscopic objects, respectively, lying in our color criteria (i.e. eqs 1-3).

Since we have spectroscopic objects with no identification (see Section 2.4), we calculate f_{cont} for the following two extreme cases. If we omit the unclear objects, we find $N_{\text{LAE}}^{\text{in}}/N_{\text{all}}^{\text{in}} = (29/29, 14/14, 11/11)$ for $z = (3.1, 3.7, 5.7)$. Note that we see no obvious interlopers in our photometric samples. In case that all the no-identification objects are interlopers, $N_{\text{LAE}}^{\text{in}}/N_{\text{all}}^{\text{in}} = (7/8, 6/7, 3/4)$, where we take magnitude cuts of $(NB503, NB570, NB816) = (24.0, 24.0, 24.5)$ that are bright enough to be completely identified by our spectroscopy. Thus, the contamination rates are taken within the ranges of $f_{\text{cont}} = (0 - 13\%, 0 - 14\%, 0 - 25\%)$ for $z = (3.1, 3.7, 5.7)$ photometric LAE samples, respectively. Since these contamination rates are negligibly small, we do not correct them for contamination. It is notable that statistical errors from contamination cannot be as large as $\sim 30\%$.

4. AGN and Multi-Wavelength Detection in our Samples

We identify AGNs in LAEs with our spectra and SXDS multi-wavelength images of radio, sub-mm, mid-infrared, and X-ray, and investigate AGN activities in our LAEs. We summarize the properties of these AGNs in Table 4. In this section, we formally define the positional uncertainty of optically-identified LAEs, $\sigma_{\text{opt}} = FWHM/2.35$, with a FWHM of narrow-band morphology.

4.1. Spectra with AGN signatures

We find 3 and 1 objects at $z = 3.1$ and 3.7 whose spectrum shows high-ionization lines, such as [N V], C IV, He II, and C III], originated from AGN activities. Figure 13 plots spectra of these four objects. All of these AGNs show broad lines in these high-ionization lines with a line width of $v_{\text{FWHM}} \gtrsim 1000 \text{ km}^{-1}$, although the line width for one of these object, NB503-N-35820, has a large uncertainty. Radio bright objects, i.e. radio galaxies, are also included in our sample. The properties of these AGNs are presented in Table 4.

We also find that NB503-N-42377 shows a marginal ($\sim 2\sigma$) C IV emission. Although a typical high- z AGN has a line ratio of $\text{Ly}\alpha/\text{CIV} = 5 - 10$ (e.g. McCarthy 1993), NB503-N-42377 has $\text{Ly}\alpha/\text{CIV} \gtrsim 25$. With the facts of the marginal C IV detection and the large flux ratio of $\text{Ly}\alpha/\text{CIV}$, we rule out an AGN being the dominant power source of $\text{Ly}\alpha$ for NB503-N-42377, and do not classify this object as an AGN.

4.2. X-ray Detection

We use a deep XMM-Newton EPIC image of SXDS, and identify an X-ray counterpart of LAEs with the combined X-ray catalog of SXDS ver 5.0 (Ueda et al. in prep.). This X-ray catalog is made of sources with a detection likelihood greater than 7 in either of 6 bands, 0.3-0.5, 0.5-2, 2-4.5, 4.5-10, 0.5-4.5, and 2-10 keV (see Ueda et al. in prep). We calculate a combined positional error by taking a sum of square errors of optical and X-ray positions. Although there are 3 X-ray counterpart candidates with a $< 2\sigma$ level of the combined error, we find by our visual inspection that one of the candidate, NB503-N-87126, clearly appears to be confused by the neighboring foreground objects. This X-ray counterpart is regarded as a foreground object. We thus identify 2 X-ray counterparts; 1 and 1 counterparts at $z = 3.1$ and 3.7 , respectively (Table 4). No counterparts are found for $z = 5.7$ LAEs.

4.3. Infrared Detection

The Spitzer MIPS $24\mu\text{m}$ -band image is investigated for infrared counterparts of LAEs. We use relatively shallow data of the Spitzer Wide-area InfraRed Extragalactic (SWIRE; Lonsdale et al. 2003) survey. The SWIRE MIPS data cover almost entire SXDS field of a 0.9 deg^2 , and miss only 13, 6, and 15 LAEs¹ at $z = 3.1$, 3.7 , and 5.7 , respectively, which are located at the edge of our SXDS-W field (see Figure 1 of Morokuma et al. 2007 submitted). The depth of MIPS data is $\sigma = 48\mu\text{Jy}$ (Shupe et al. in preparation; see Ivison et al. 2007). We run SExtractor to detect and measure source fluxes with a $12''$ -diameter aperture. We apply the aperture correction of a factor of 1.698 to the aperture fluxes (see <http://ssc.spitzer.caltech.edu/mips/apercorr/>). We have cross matched our LAEs with MIPS sources detected at a $> 5\sigma$ level, i.e. $> 240\mu\text{Jy}$. We find 3 (and 0) MIPS counterparts at $z = 3.1$ (at $z = 3.7$ and 5.7) within the 3σ positional allowance of our LAEs (Table 4).

4.4. Sub-mm Detection

We compare the positions of LAEs with SCUBA $850\mu\text{m}$ sources of Submm Half-Degree Extragalactic Survey (SHADES; Coppin et al. 2006). The rms noise level is $\simeq 2.2\text{mJy}$. The SHADES image covers an $\sim 360\text{ arcmin}^2$ area at the center of SXDS-C, which corresponds to about 10% of our 1 deg^2 SXDS field. In this SHADES region, we have about 16, 6, and 3 LAEs at $z = 3.1$, 3.7 , and 5.7 , respectively. These LAEs include one X-ray emitting LAE of NB503-C-49497 at $z = 3.128$ (see Table 4). The beam size of the sub-mm image is as large as $FWHM = 14.7\text{ arcsec}$. Following Ivison et al. (2007), we search counterparts with a positional error circle of radius 8 arcsec . We find no submm counterparts in our LAEs (including the X-ray emitting LAE) located at the SHADES area. We extend our search radius up to 12.5 arcsec for completeness. We find that a $z = 5.7$ LAE of NB816-C-90169 falls on the large search radius of a submm source of Sxdf850.5 (Coppin et al. 2006). However, on our optical images this submm source is very likely centered at a foreground galaxy of SXDS-iC-086385 with $i' = 21.11$. Thus, we conclude that none of our LAEs has a sub-mm emission down to $\simeq 3 - 5\text{mJy}$ in the SHADS area.

¹ All of X-ray and radio emitting LAEs listed in Table 4 are included in the MIPS area.

4.5. Radio Detection

We investigate radio properties of LAEs with deep VLA 1.4-GHz radio image of the SXDS (Simpson et al. 2006a). This radio image reaches an rms noise level of $12\mu\text{Jy beam}^{-1}$. We search a radio counterpart of LAEs in a 3×3 pixel box of the VLA image (1 pixel= 1.25 arcsec). A radio source with a signal-to-noise ratio of > 5 are identified as a radio counterpart in the same manner as Simpson et al. (2006b). We then visually inspect LAEs with radio contours, and find that two LAEs are detected in the radio image ² (Table 4).

4.6. LAEs Hosting AGN

As summarized in Table 4, we find that 4 $z = 3.1$ and 1 $z = 3.7$ LAEs have a detection in the multi-wavelength data. Figure 14 presents the spectral energy distribution (SED) of these AGN-LAEs, together with those of the average radio quiet/loud quasars (Elvis et al. 1994). We also plot a UV-optical spectrum of Telfer et al. (2002); Richards et al. (2003) that is normalized to the average SED of (Elvis et al. 1994). We refer to these average SEDs+spectrum as QSO templates.

Since the detection limits of infrared and X-ray (and radio) bands are as large as $\nu L_\nu \gtrsim 10^{44}$ (10^{41}) erg s^{-1} , LAEs with any multi-wavelength counterparts likely host AGN. In fact, we have 3 spectroscopically-identified LAEs with multi-wavelength counterparts (Table 4). The spectroscopic classifications of these LAEs indicate that all of these LAEs have AGN. Thus, we classify all of 5(= 4 + 1) LAEs with multi-wavelength detection as AGN. In addition to these 5 AGNs identified by multi-wavelength data, we have 4 spectroscopically-identified AGNs. Since 3 AGNs have both a multi-wavelength detection and spectroscopic identification, the number of our LAEs with an AGN (hereafter AGN-LAEs) is 6 in total: 4 and 2 at $z = 3.1$ and 3.7 , respectively. No AGN-LAEs are found at $z = 5.7$. Note that 3 $z = 3.1$ and 1 $z = 3.7$ AGN-LAEs out of 6 AGN-LAEs satisfy our color criteria of photometric samples (eq. 1 or 2; see Table 4). These numbers (i.e. 3 and 1) are sufficiently smaller than those of entire photometric samples (356 and 101 for $z = 3.1$ and 3.7). Since the AGN fraction in our photometric sample is negligibly small, ³ AGN-LAEs do not largely contribute to the statistical properties of LAEs in the following sections.

² We find that a radio source is located around NB503-S-29853. Since the flux center of this radio source is obviously placed outside of NB503-S-29853, this radio source is likely associated with the other source(s).

³ We discuss the AGN fraction of our photometric samples in Section 7.2. We address star-forming activities of LAEs with the multi-wavelength data in Section 7.3.

5. Luminosity Functions

5.1. Ly α Luminosity Functions

We derive luminosity functions (LFs) of LAEs at $z = 3.1, 3.7,$ and 5.7 from our photometric samples. First, we calculate LFs with a simple classical method that was taken by most of previous studies (e.g. Ouchi et al. 2003; Ajiki et al. 2003; Hu et al. 2004; Malhotra & Rhoads 2004). We obtain the number densities of LAEs in each magnitude bin by simply dividing the observed number counts of LAEs in a given narrow band by the effective survey volume defined as the FWHM of the bandpass times the area of the survey. Here, we calculate the Ly α luminosity of each object with the response curves of narrow and broad bands by subtracting the continuum emission measured from the continuum magnitude from the total luminosity in the narrow band, assuming that Ly α enters in the central wavelength of the narrow band. In this calculation, we use total magnitude of narrow-band images. The continuum emission is estimated by the narrow-band excess color (i.e. color of narrow-band and broad-band) defined with a $2''$ aperture, so as to keep high signal-to-noise ratios and to avoid the effects of source confusion on broad-band images with high source density. To check the accuracy of this calculation, Figure 15 compares Ly α fluxes measured from our images and spectra for our spectroscopic samples. Figure 15 shows that both measurements agree well within error bars for most of LAEs. These values mostly scatter within the range of difference of a factor of 2.

Figures 16-18 present the LFs from this classical method. Note that we corrected the detection-completeness by weighting with f_{det} measured in Section 3.2. To check the field-to-field variation and the accuracy of our results, we plot the estimates of LFs from the entire 1 deg^2 field (filled circles), together with those from the five $\simeq 0.2 \text{ deg}^2$ fields (open symbols). In Figures 16-17, we calculate the errors of field-to-field variations with eq. (4), and include these errors in the error bars of LFs for the entire 1 deg^2 field. We find that the field-to-field variations are as large as a factor of $\simeq 2 - 5$ among the five 0.2 deg^2 fields, although the typical scatters of the 0.2 deg^2 results are *not* far beyond the errors of Poisson statistics. Then we obtain the best-fit Schechter function (Schechter 1976) defined by

$$\phi(L)dL = \phi^*(L/L^*)^\alpha \exp(-L/L^*)d(L/L^*). \quad (7)$$

The classical method is accurate when the narrow-band filter has an ideal boxcar shape. However, since the shapes of actual filters used in LAE surveys are rather close to a triangle, the classical method potentially suffers from the following two uncertainties. (a) The narrow-band magnitude of LAEs of a fixed Ly α luminosity varies largely as a function of redshift. Thus Ly α luminosity may be over- or under-estimated for some LAEs. (b) The selection function of LAEs in terms of EW also changes with redshift; the minimum EW value

corresponding to a given (fixed) narrow-band excess, such as $i' - NB816$ for $z = 5.7$ LAEs, becomes larger when the redshift of the object goes away from the redshift corresponding to the center of bandpass.

In order to avoid such uncertainties, we perform Monte Carlo simulations to find the best-fit Schechter parameters for the Ly α LF. These Monte Carlo simulations are developed by Shimasaku et al. (2006), and the details of simulations are described in their paper. We briefly summarize the procedure of these simulations. We generate a mock catalog of LAEs with a set of the Schechter parameters (α, ϕ^*, L^*) and a Gaussian sigma of probably distribution of EW, σ_{EW} . We uniformly distribute them in comoving space over the redshift range of all LAEs that can be selected with our narrow-band filter. We ‘observe’ these LAEs with the narrow- and broad-bands same to the real band responses (Figure 1), and add to their flux densities photon noise corresponding to the actual observation. We select LAEs by the same criteria as for selecting the actual LAEs, and derive the number densities and color distributions from the mock catalog. We compare these results with the observational measurements of number densities and color distributions. By performing this set of simulations over a wide range of the parameters, we find the best-fit Schechter parameters by χ^2 fitting. We compare the results of these simulations with the observational measurements corrected for the detection completeness, since the simulations are not affected by the detection completeness, f_{det} . In Figures 9-12, we plot the predicted surface densities and color distributions of LAEs for some parameter sets.

The difference in χ^2 for α values is found to be insignificant. We fix the α value to -1.0, -1.5, and -2.0, and carry out χ^2 fitting, varying ϕ^* , L^* , and σ_{EW} . Figures 9-11 present that all three models of $\alpha = -1.0, -1.5,$ and -2.0 reproduce the observed counts well, although shallower α gives a slightly better fit. This suggests that the Ly α LF of LAEs is approximated well by the Schechter function. The best-fit parameters, thus obtained, are summarized in Table 5. We adopt the $\alpha = -1.5$ results as the fiducial set of the best-fit Schechter parameters (see Gronwall et al. 2007). Our best-fit Schechter parameters with $\alpha = -1.5$ are $\phi^* = (9.2_{-2.1}^{+2.5}, 3.4_{-0.9}^{+1.0}, 7.7_{-3.9}^{+7.4}) \times 10^{-4} \text{ Mpc}^{-3}$ and $L_{Ly\alpha}^* = (5.8_{-0.7}^{+0.9}, 10.2_{-1.5}^{+1.8}, 6.8_{-2.1}^{+3.0}) \times 10^{42} \text{ erg s}^{-1}$ at $z = (3.1, 3.7, 5.7)$.

The best-fit Schechter functions for $\alpha = -1.5$ obtained above are shown in Figures 16-18 with the solid lines. Note that the LFs from the classical method (filled circles) are consistent with the best-fit Schechter functions from our simulations. This means that the simple method gives a good approximation. This is probably because the uncertainties (a) and (b) in the classical method are negligible and/or cancel with each other. The number densities of the best-fit Schechter functions are slightly larger than those of the classical method. This slight difference can be explained by the underestimates of the number density and Ly α

luminosity with the classical method due to the large survey volume of the top-hat redshift distributions and the small Ly α flux measured with a bandpass of the triangle-shaped narrow bands.

Note that these best-fit LFs are based on our LAE samples selected with a limit of EW (Table 3). If we extrapolate the EW distribution down to $EW = 0\text{\AA}$ with our simulations, we can obtain estimates of the LFs for all LAEs with $EW > 0\text{\AA}$. We refer a ϕ^* value of LFs for all ($EW > 0\text{\AA}$) LAEs as for ϕ_0^* , and present the best-fit ϕ_0^* in Table 5. These ϕ_0^* values only differ from ϕ^* by $\sim 10\%$. There are two reasons for this small difference: (i) The typical distribution of EW, σ_{EW} , is much wider than that of EW limit of our selection, EW_{lim} (see Tables 3 and 5). (ii) the EW range missed by our selection ($0 < EW < EW_{\text{lim}}$) is significantly shorter than that of our selection ($EW > EW_{\text{lim}}$). The combination of these facts provide this small ($\sim 10\%$ -level) difference between ϕ^* and ϕ_0^* .

5.1.1. Comparison with Previous Measurements

We overplot previous measurements of Ly α LFs for $z \simeq 3, 4$ and 6 in Figure 19. Our LFs of $z \sim 3$ and 4 agree very well with all of the previous measurements typically within the error bars. It is noticeable that the best-fit Schechter function of Gronwall et al. (2007) (from the 0.3 deg² survey) shows an extremely good agreement with ours within a factor of ~ 0.1 , although the luminosity range of their measurements is limited to the relatively faint luminosity (i.e. $\log L \simeq 42 - 43 \text{ erg s}^{-1}$).

In the bottom panel of Figure 19, the previous measurements of $z \sim 6$ LAEs show large scatters over Poisson errors. However, our measurements are consistent with those of Shimasaku et al. (2006) (red open circles) as well as the recalculated LF of Hu et al. (2004) (squares), both of which are based on deep and moderately-wide ($\simeq 0.2 \text{ deg}^2$) field imaging and spectroscopy. Moreover, $z = 5.7$ LF of the recent 2-deg² imaging survey of Murayama et al. (2007) (red open diamonds) agrees with ours within 1σ error bars at $\log L > 43.0 \text{ erg s}^{-1}$ where the measurements of Murayama et al. (2007) are complete. (Note that the imaging data of Murayama et al. (2007) are shallower than ours by ~ 1 magnitude, and that the data points of Murayama et al. (2007) are not corrected for incompleteness.) The best-fit Schechter function of Malhotra & Rhoads (2004) (dotted line) is significantly lower than our LFs. Shimasaku et al. (2006) and Tapken et al. (2006) have also pointed out that the measurements of Malhotra & Rhoads (2004) are lower than their LFs. Our $z = 5.7$ LF is consistent with the measurements of Ajiki et al. (2006) (stars) and Tapken et al. (2006) (hexagon) within the error bars, but our measurements would be systematically higher than theirs. This difference is probably originated from i) the method of Ly α luminosity

estimates from photometric data, ii) the detection-completeness correction and iii) field-to-field variation raised by smaller field surveys of Ajiki et al. (2006) and Tapken et al. (2006). The differences in selection criteria for LAEs between our sample and the others are probably not a main reason for this discrepancy, since, for our data, changing the $i' - NB816$ threshold over 1.2 – 1.5 only makes a difference in number density by 11%.

5.1.2. Evolution of Ly α Luminosity Function

Our LFs are appropriate to identify an evolutionary trend of LF, since our LFs from $z = 3.1$ to 5.7 are derived by the same procedure with similar data sets from the same instrument. In Figure 19, we compare our Ly α LFs of LAEs at $z \sim 3, 4,$ and 6. The LFs do not change within error bars at these redshifts. The left panel of Figure 20 shows the error ellipses of Schechter parameters of our LFs at $z = 3.1 - 5.7$. All the 2σ -error contours well overlap each other. At the fixed slope of $\alpha = -1.5$, the best-fit parameters of LFs change from $z = 3.1 - 5.7$ only by factors of 1.8 and 2.7 in L^* and ϕ^* , respectively. Since these error ellipses are obtained by our observational data whose limiting Ly α EW is different at each redshift, we also plot in the right panel of Figure 20 the ellipses for all LAEs with a positive emission ($EW > 0$) which are obtained from the extrapolation with our simulations. In this case, the overlaps of $z = 3.1$ and $z = 3.7$ error ellipses become smaller. However, the error ellipses of $z = 5.7$ LAEs are much larger than those of $z = 3.1$ and 3.7. These large $z = 5.7$ error ellipses still appear to be consistent with $z = 3.1$ and 3.7 error ellipses. The results for LAEs with $EW > 0$ are similar to those for the observed LAEs. This is because the number density of observed LAEs (ϕ^*) differs from that of all LAEs (ϕ_0^*) only by $\sim 10\%$, as discussed in Section 5.1. Thus, we conclude that Ly α LFs of LAEs do not evolve by more than a factor of 2-3 either in luminosity or number density, and that drastic evolution in the Ly α LF of LAEs from $z \sim 3.1$ to $z = 5.7$ is ruled out. It should be noted that the central positions of $z = 3.7$ contours appear to be shifted to brighter L^* and lower ϕ^* than those of $z = 3.1$ and 5.7, although this shift is not significant within $1 - 2\sigma$ levels. This small shift may indicate a moderate evolution of LFs between these redshifts. However, it is possible that AGNs at the bright-end LF more strongly affect the Schechter fit of $z = 3.7$ LF than that of $z = 3.1$ and 5.7 LFs, due to the shallow detection limit of our $z = 3.7$ LAEs (see Section 4.6).

Note that Ly α fluxes from high- z objects are generally attenuated by neutral hydrogen of intervening inter-galactic medium (IGM). It is known that high- z galaxies have an asymmetric Ly α emission whose blue side of line is more strongly absorbed by neutral hydrogen of IGM than low- z galaxies. (e.g. Hu et al. 2004; Shimasaku et al. 2006). Thus, the Ly α

LFs in Figure 19 (solid lines) should be called *apparent-Ly α* LFs. Due to the absorption of IGM, we cannot directly measure *intrinsic-Ly α* fluxes that are emitted from LAEs. However, we can constrain the evolution of *intrinsic-Ly α* LFs with *apparent-Ly α* LFs. First, the lower limits of *intrinsic-Ly α* LFs are obviously given by the *apparent-Ly α* LFs (solid lines of Figure 19). Second, we can estimate the *intrinsic-Ly α* luminosity with the average Gunn-Peterson (GP) optical depths. The GP optical depths are estimated in various studies. Here, based on the results of Fan et al. (2006) (Fan), Madau (1995) (Madau), and Meiksin (2006) (Meiksin), we calculate the ratios of intrinsic Ly α flux, $f_{\text{Ly}\alpha}^{\text{int}}$, to apparent Ly α flux, $f_{\text{Ly}\alpha}^{\text{app}}$. Assuming that IGM absorbs a blue half of symmetric Ly α emission line, we estimate the ratios $f_{\text{Ly}\alpha}^{\text{app}}/f_{\text{Ly}\alpha}^{\text{int}}$ with the formulae of (Fan, Madau, Meiksin) to be (0.85, 0.81, 0.84), (0.76, 0.73, 0.76), and (0.53, 0.54, 0.52) at $z = 3.1, 3.7,$ and 5.7 , respectively. Since the $f_{\text{Ly}\alpha}^{\text{app}}/f_{\text{Ly}\alpha}^{\text{int}}$ ratios change only by 3–5% between these three estimates, we use the classic Madau 1995’s model. The dashed lines in Figure 21 correspond to the *intrinsic-Ly α* LFs that we estimate. This figure indicates that *intrinsic-Ly α* LFs may evolve significantly, and that luminosities and/or number densities of LAEs are intrinsically brighter/higher at $z = 5.7$ than $z = 3.1$.

Note that we estimate these *intrinsic-Ly α* LFs with two assumptions. The first assumption is that the density of neutral hydrogen atoms in the intervening IGM is the cosmic average value at each epoch. However, hydrogen clouds around LAEs are likely more ionized by the UV radiation from LAEs. On the other hand, the chance of intervening galaxies with molecular hydrogen probably increases around LAEs, due to clustering of galaxies. The second assumption is that the *intrinsic-Ly α* emission of LAEs has a symmetric profile whose central wavelength is not red- or blue-shifted. Shapley et al. (2003) find in a composite spectrum of $z = 3$ LBGs that Ly α emission is redshifted by 360 km s^{-1} from the average of continuum absorption lines. Because the typical Ly α FWHM of LAEs is as small as $< 300 \text{ km s}^{-1}$ (e.g. Rhoads et al. 2003; Hu et al. 2004; Shimasaku et al. 2006), the IGM will absorb only a small fraction of Ly α photons if they are redshifted by about 360 km s^{-1} . However, this is true only if Ly α properties of LAEs are similar to those of $z = 3$ LBGs. In fact, the typical Ly α FWHM of LAEs is smaller than that of $z = 3$ LBGs ($450 \pm 150 \text{ km s}^{-1}$ Shapley et al. 2003). It is possible that the velocity offset of Ly α emission may also be smaller in LAEs than in LBGs (360 km s^{-1}). In this way, the inferred *intrinsic-Ly α* features (such as those found in Figure 21) are real only if these two assumptions are correct. We need high-resolution spectroscopy for LAEs and sophisticated numerical simulations to assess the *intrinsic-Ly α* LF, and to derive a reliable conclusion on its evolution.

In summary, it is interesting that *apparent* LF of LAEs does not show a significant evolution over the long redshift range of $z = 3.1$ to 5.7 . We point out the possibility that evolution of IGM and LAEs may be tuned to realize this no evolution at $z = 3.1 - 5.7$, if the amount of external absorption changes with redshift.

5.2. UV Luminosity Functions

We derive the UV LFs of our LAEs at $z = 3.1$, 3.7 , and 5.7 . We use our LAE catalogs, and obtain UV-continuum luminosities from magnitudes of a broad band whose bandpass does not include $\text{Ly}\alpha$ but only continuum emission. We choose R magnitudes for $z = 3.1$ and 3.7 LAEs, and z' magnitudes for $z = 5.7$ LAEs, where the corresponding wavelengths are $\sim 1300 - 1600\text{\AA}$ in rest frame. We apply no k-corrections to the UV magnitudes, since the difference of UV magnitudes in this narrow-wavelength range is negligibly small for LAEs with a flat continuum (Section 6.3). We calculate number densities from the survey volume and the number counts as a function of UV magnitudes by weighting with the detection completeness (Section 3.2). Note that we need a careful estimation of total magnitudes of broad band. Since the aperture sizes and shapes of MAG_AUTO magnitudes are defined by the sources on the narrow-band images, the MAG_AUTO magnitudes of broad-band images could be contaminated by the neighboring continuum sources. Thus, we identify and deblend sources on our broad-band images with SExtractor, and cross-match the broad-band sources with our LAEs. If a LAE do not have a corresponding broad-band source detected over a 3σ level, we just use photometry of a $2''$ -diameter aperture. We refer to these magnitudes as a total magnitudes of broad band, and derive UV LFs with these magnitudes. For comparison, we also calculate the LFs from the simple $2''$ -diameter aperture photometry with no completeness correction. These simple estimates provide lower limits of UV LFs.

Figure 22 shows the UV-LFs of our LAEs, together with the previous measurements of LAEs and dropout galaxies (or LBGs) at each redshift. Our UV-LFs are consistent with those of Hu et al. (2004) and Shimasaku et al. (2006) at $z = 5.7$, although their measurements show slightly higher number densities than ours. To check the consistency, we calculate $z = 5.7$ LF in the same manner as Shimasaku et al. (2006) who simply used $2''$ -diameter aperture magnitudes with aperture corrections estimated with their *NB816* image. Our LF by the method of Shimasaku et al. (2006) presents a very good agreement with that of Shimasaku et al. (2006). However, we find that the aperture corrections defined with *NB816* band overestimate the broad-band magnitudes. This is because the $\text{Ly}\alpha$ morphology in the narrow band is generally more extended than UV morphology on the broad band. Thus, we take our best estimates based on the MAG_AUTO magnitudes with the source deblending on the broad-band images.

In Figure 22, we find that UV-LFs of LAEs do not change at $z \simeq 3 - 4$, but evolve from $z \sim 4$ to 5.7 . There exist an emergence of UV-bright LAEs at $z = 5.7$. We compare these UV LFs with those of dropout galaxies. At $z = 3 - 4$, number densities of our LAEs are as much as 10% of dropout galaxies down to $M_{\text{UV}} \simeq -20$, which corresponds to $\simeq M_{\text{UV}}^*$ or $\simeq M_{\text{UV}}^* + 1$ (Steidel et al. 1999; Ouchi et al. 2004a; Sawicki & Thompson 2006; Beckwith et al. 2006;

Yoshida et al. 2006; Vanzella et al. 2006b). Note that the EW limit of our $z = 3 - 4$ LAE samples is $\simeq 40 - 60\text{\AA}$. This ratio of Ly α emitting galaxies to dropout galaxies is consistent with that reported by Shapley et al. (2003) who find that 25% and $\sim 2\%$ of their $z = 3$ dropout galaxies have Ly α emission line with $EW_0 \geq 20\text{\AA}$ and $EW_0 \geq 100\text{\AA}$, respectively. On the other hand, at $z = 5.7$, the number densities of our LAEs seems comparable to, or at least more than 50% of, dropout galaxies at $z \sim 6$, where the EW limit of our $z = 5.7$ LAE is about $\simeq 30\text{\AA}$. Spectroscopic studies of Dow-Hygelund et al. (2006) report that 6 Ly α emitting galaxies with $EW_0 \geq 20\text{\AA}$ are found in their i' -dropout sample of CL1252 and HUDF parallel fields, and conclude that about $\sim 30\%$ of i' -dropout galaxies have a Ly α emission line. This result is consistent with the measurements of previous studies (Stanway et al. 2004a,b; Vanzella et al. 2006a). More recently, Stanway et al. (2007) show that 16 out of 24 i' -dropout galaxies do not have a Ly α emission line with $EW_0 \geq 25\text{\AA}$ in the GLARE/HUDF field. Most of the previous spectroscopic studies of i' -dropout galaxies suggest that $\sim 30\%$ of i' -dropout galaxies down to $\sim L^*$ have a Ly α emission line with $EW_0 \geq 20\text{\AA}$. It is not clear why our ratio of dropout galaxies and LAEs is higher than those of spectroscopic results. There are three possible explanations. The first is the difference of the definition in the ratio. We compare the ratio of LAEs to dropout galaxies at the same redshift, but Dow-Hygelund et al. (2006) and Stanway et al. (2007) obtain the ratio of Ly α emitting dropouts to all the dropouts. If all the LAEs are identified by dropout technique, these two ratios should be comparable. However, LAEs with no significant continuum are likely missed by the dropout selection. Moreover, the i dropout selection systematically misses the strong Ly α emission lines at $z \lesssim 6$. The selection differences may cause the discrepancy between these two ratios estimated by the different methods. In fact, the theoretical model of Dijkstra & Wyithe (2007) suggests that LAE selections identify more population III galaxies with a large EW than dropout selections, and that the EW distribution of LAEs should not be the same as that of dropouts. The second explanation is that LFs of dropout galaxies have systematic errors. Indeed, we compare the LFs of dropout galaxies of Bouwens et al. (2006) to estimate the ratio. However, the measurements of dropouts' LFs scatter by a factor of 2 or more in the different estimates by various authors. We show the uncertainties of estimates with the gray shade in Figure 22. The third explanation is the evolution of UV LFs from $z = 5.5$ to 6.5 as claimed by Dow-Hygelund et al. (2006). The UV-LFs of dropout galaxies decrease in number density and/or luminosity from $z \sim 4$ to 6 (e.g. Lehnert & Bremer 2003; Ouchi et al. 2004a; Shimasaku et al. 2005; Bunker et al. 2004), and even more significantly evolve from $z \sim 6$ to higher redshifts of $z \sim 7 - 8$ (Bouwens et al. 2006). Since i -dropout galaxy samples distribute over $z = 5.5 - 6.5$, the LFs of i -dropout galaxies are measured at higher redshifts in average than that of our LAEs (i.e. $z = 5.7$). This would not allow us to obtain the accurate ratio of Ly α emitting population to dropout galaxies. For these reasons, it is likely that the simple comparison between LFs of dropout galaxies and LAEs would not

give a ratio between all $z \sim 6$ objects and Ly α emitting population.

It is interesting to compare the shapes of UV LF of LAEs and dropout galaxies. At $z = 3 - 4$, we find a significant deficit of UV-bright LAEs with respect to dropout galaxies. This deficit of UV-bright LAEs are reported by Ouchi et al. (2003) at $z = 4.9$ based on the comparison of dropout and LAE LFs. This tendency is also consistent with the results of Section 6.2 and the claims of Ando et al. (2006); Shimasaku et al. (2006); Vanzella et al. (2006b) who find that UV-bright galaxies do not have a large Ly α EW from spectroscopic samples at $z = 5 - 6$. On the other hand, this tendency cannot be clearly seen for $z \sim 6$ in Figure 22, probably due to the large uncertainties of LF of dropout galaxies.

We fit the Schechter function,

$$\psi(M)dM = C\phi^* \exp \{-C(\alpha + 1)(M - M^*) - \exp[-C(M - M^*)]\} dM, \quad (8)$$

to the UV LFs, where $C \equiv 0.4 \ln(10)$: α is the power-law slope, ϕ^* is the normalization factor, and M^* is the characteristic absolute magnitude. We fit the Schechter function with the measurements over a 5σ level (filled circles in Figure 22). Since the faintest points of our $z = 3.7$ LAEs appear to be suffered from the incompleteness of source detection, we do not use the point for the fitting. Since our LAE samples are not enough to derive α , we fix the slope to $\alpha = -1.5$. For our $z = 3.7$ sample, we fix the M^* to the best-fit M^* value of our $z = 3.1$ LAEs. We summarize the results of the fitting in Table 6.

We find no evolution at $z \sim 3 - 4$, even considering the error bars. The difference between $z = 3.1$ and 3.7 LFs is within 50% in number density or luminosity. On the other hand, UV LFs of LAEs evolve significantly from $z \sim 3 - 4$ to 6. If it comes from the pure luminosity evolution, the UV LFs brighten by a ~ 1 magnitude from $z \sim 3 - 4$ to $z = 5.7$. Note that the EW limits of our selections are different between these redshifts. However, the difference of sample selection only changes by $\sim 10\%$ in number density, according to the results of our simulations (Section 5.1). Thus, this evolutionary trend of UV LFs is not affected by the selection effects.

5.3. Ly α - and UV-Luminosity Densities Contributed from Ly α Emitters

We calculate Ly α and UV-luminosity densities of our LAEs from the luminosity functions (LFs) derived in sections 5.1 and 5.2. We show Ly α and UV-luminosity densities in Tables 5 and 6, respectively. These tables present Ly α (UV) luminosity densities down to our observational detection limits, $\rho_{\text{Ly}\alpha}^{\text{obs}}$ ($\rho_{\text{UV}}^{\text{obs}}$), and total luminosity densities down to zero luminosity by extrapolation, $\rho_{\text{Ly}\alpha}^{\text{tot}}$ ($\rho_{\text{UV}}^{\text{tot}}$). These observational and total luminosity densities

provide approximated lower and upper limits. For a reference, we estimate total Ly α luminosity densities of LAEs with $EW > 0$, from our simulations, which are shown under $\rho_{0\text{Ly}\alpha}^{\text{tot}}$ in Table 5.

In Table 5, the total Ly α luminosity density is $\sim 10^{40} \text{ erg}^{-1}\text{s}^{-1}\text{Mpc}^{-3}$ at $z = 3.1 - 5.7$, and does not change within a 1σ level from $z = 3.1$ to 5.7 . Table 6 shows that the total UV luminosity density would increase from $\sim 4 \times 10^{25} \text{ erg}^{-1}\text{s}^{-1}\text{Hz}^{-1}\text{Mpc}^{-3}$ to $\sim 8 \times 10^{25} \text{ erg}^{-1}\text{s}^{-1}\text{Hz}^{-1}\text{Mpc}^{-3}$ at $z = 3 - 4$ to 5.7 , although the difference is only a 1σ level because of large errors. This possible increase of UV luminosity density could be due to the fact that UV bright LAEs increase at $z = 5.7$ as shown in Figure 22.

Note that the entire Ly α (and UV) emission is not only originated from star-formation activities, but also from cooling radiation, shock winds, and AGN, and that Ly α (and UV) emission is attenuated by dust and IGM. However, we roughly estimate the contribution of star-formation from LAEs with those luminosity densities to check the consistency with the previous studies. We use the simple prescription of Ly α luminosity, $L_{\text{Ly}\alpha}$, and star-formation rate, SFR ,

$$SFR(M_{\odot}\text{yr}^{-1}) = L_{\text{Ly}\alpha}(\text{erg s}^{-1})/(1.1 \times 10^{42}), \quad (9)$$

combining the relation of H α luminosity and star-formation rate (Kennicutt 1998) and the case B approximation (Brocklehurst 1971). With the assumptions of Salpeter IMF and solar metallicity (Madau, Pozzetti, & Dickinson 1998), the relation between UV luminosity and star-formation rate, is:

$$\text{SFR}(M_{\odot}\text{yr}^{-1}) = L_{\text{UV}}(\text{erg s}^{-1}\text{Hz}^{-1})/(8 \times 10^{27}), \quad (10)$$

where L_{UV} is the UV luminosity measured in 1500\AA . In Figures 19 and 22, we plot ticks of star-formation rates corresponding to Ly α and UV luminosities based on these formulae of eqs (9) and (10). Assuming these equations, SFRs of a typical (L^*) LAE are $SFR(M_{\odot}\text{yr}^{-1}) = (5.3_{-0.6}^{+0.8}, 9.3_{-1.4}^{+1.6}, 6.2_{-1.9}^{+2.7})$ and $(4.5 \pm 2.0, \sim 4.5, 9.4 \pm 7.0)$ at $z = (3.1, 3.7, 5.7)$, which are estimated from Ly α and UV-continuum L^* , respectively. Thus, a typical LAE has a SFR of $\simeq 5 - 10 M_{\odot} \text{ yr}^{-1}$ at $z = 3.1 - 5.7$, although these SFRs are correct under the assumptions given by eqs. (9) and (10).

We estimate the nominal lower limits of cosmic SFR density (SFRD) from the luminosity densities down to our detection limits, $\rho_{\text{Ly}\alpha}^{\text{obs}}$. From Table 5, the observed Ly α luminosity density, $\rho_{\text{Ly}\alpha}^{\text{obs}} = (4.8_{-1.0}^{+1.2}, 2.4_{-0.6}^{+0.7}, 3.6_{-1.7}^{+3.1}) \times 10^{39} \text{ erg}^{-1}\text{s}^{-1}\text{Mpc}^{-3}$ for redshifts of (3.1, 3.7, 5.7). If we naively estimate SFR densities (SFRD) from these Ly α luminosity densities with eq. (9), we obtain $SFRD = (4.3_{-0.9}^{+1.1}, 2.1_{-0.5}^{+0.6}, 3.2_{-1.6}^{+2.8}) \times 10^{-3} M_{\odot}\text{yr}^{-1}\text{Mpc}^{-3}$ for $z = (3.1, 3.7, 5.7)$. Similarly, we estimate SFRDs from the observed UV luminosity densities, $\rho_{\text{UV}}^{\text{obs}}$, which are $(1.2_{-0.7}^{+1.4}, 0.5_{-0.1}^{+0.1}, 0.9_{-0.7}^{+2.5}) \times 10^{25} \text{ erg}^{-1}\text{s}^{-1}\text{Hz}^{-1}\text{Mpc}^{-3}$ for redshifts of (3.1, 3.7, 5.7). Based

on eq. (10), we obtain $SFRD = (1.5_{-0.8}^{+1.8}, 0.7_{-0.1}^{+0.1}, 1.1_{-0.8}^{+3.1}) \times 10^{-3} M_{\odot}\text{yr}^{-1}\text{Mpc}^{-3}$ for $z = (3.1, 3.7, 5.7)$. These Ly α and UV SFRDs are consistent with those obtained by the previous studies (see Taniguchi et al. 2005 and references therein).

If we estimate the nominal total SFRDs from the total luminosity densities of $\rho_{\text{Ly}\alpha}^{\text{tot}}$ and $\rho_{\text{UV}}^{\text{tot}}$ that are given by the extrapolation of luminosity functions, we obtain $SFRD = (8.5_{-1.5}^{+1.8}, 5.7_{-1.2}^{+1.3}, 8.3_{-3.4}^{+5.9}) \times 10^{-3}$ and $(5.5_{-3.0}^{+6.5}, 5.1_{-0.7}^{+0.8}, 9.4_{-6.9}^{+26}) \times 10^{-3} M_{\odot}\text{yr}^{-1}\text{Mpc}^{-3}$ for $z = (3.1, 3.7, 5.7)$, respectively. We compare the SFRD estimated from Ly α LF of $z = 3.1$ LAEs that is recently obtained by MUSYC. Gronwall et al. (2007) have found that SFRD contributed by $z = 3.1$ LAEs is $\simeq 6.5 - 8.6 \times 10^{-3} M_{\odot}\text{yr}^{-1}\text{Mpc}^{-3}$. Our result of $8.5_{-1.5}^{+1.8} \times 10^{-3} M_{\odot}\text{yr}^{-1}\text{Mpc}^{-3}$ is very consistent with their finding.

The SFRD from UV luminosity density may increase from $z = 3.1$ to 5.7 by a factor of 2, but again the large errors do not distinguish between evolutionary effects and uncertainties. If we take into account the large error bars, $SFRD \simeq 5 - 9 \times 10^{-3} M_{\odot}\text{yr}^{-1}\text{Mpc}^{-3}$ at $z = 3.1 - 5.7$. We compare these SFRDs with those estimated from dropout galaxies. The results of SFRD measurements with no dust correction show that the SFRDs of dropouts are $\simeq 2 - 3 \times 10^{-2} M_{\odot} \text{yr}^{-1} \text{Mpc}^{-3}$ at $z \sim 3 - 6$ (Steidel et al. 1999; Bouwens et al. 2006; Hopkins 2006). Thus, LAEs contribute roughly about $\simeq 20 - 40\%$ of the entire cosmic SFRD at $z = 3 - 6$.

6. Properties of Ly α Emitters

6.1. Statistics of Ly α Equivalent Width

Figure 23 presents the histogram of rest-frame equivalent width (EW_0) for our LAEs. We calculate EW_0 of our LAEs from our photometric measurements by the modeling described in Section 5.1. We then obtain two estimates of the EW_0 distribution by (i) taking the best measurements of EW_0 for each LAE and (ii) summing the probability distribution of EW_0 that is defined by errors of EW_0 . We show in Figure 23 these two estimates with (i) histograms (+Poisson errors) and (ii) solid curves. We find that the results of (i) and (ii) agree fairly well for $z \sim 3$ and 4 LAEs. However, for our $z \sim 6$ LAEs, we see a significant difference at $EW_0 = 100 - 150\text{\AA}$. This discrepancy between (i) and (ii) for $z \sim 6$ LAEs is probably due to the large errors of the relatively shallow off-band (i.e. z' -band) photometry. Thus, we regard the difference of (i) and (ii) as the uncertainties of our measurements. The gray histograms and curves indicate the EW_0 distribution for all of our photometrically-selected LAEs. Since our three LAE samples at $z = 3.1, 3.7, 5.7$ do not have the same limits of Ly α luminosity and EW_0 , we make subsamples of LAEs that share the same detection

limits for comparison. We set $\log L(\text{Ly}\alpha) \gtrsim 42.6 \text{ erg s}^{-1}$ and $EW_0^{\text{int}} \gtrsim 70 - 80 \text{ \AA}$ for the limits of our subsamples, because our three LAE samples are complete in these limits. The histograms of these subsamples are plotted with black lines at each panel. We compare these histograms with those for spectroscopically identified LAEs. Although the statistical accuracy is limited for the spectroscopic LAE samples, the EW_0 distributions of spectroscopic and photometric samples are consistent.

In Figure 24 we plot gray areas showing the EW_0 distributions for the subsamples with the uncertainties of (i) and (ii). We find no clear evolution of EW_0 distribution from $z = 3.1$ to 5.7 with the uncertainties of our measurements. Since these EW_0 distributions are based on the apparent EW, we correct for the absorption of IGM with the average attenuation at $z = 3.1, 3.7, 5.7$ (see Section 5.1.2). We present in Figure 24 the distribution of *intrinsic* EW_0 (i.e. EW_0 corrected for IGM absorption) with cyan, blue, and red regions for $z = 3.1, 3.7,$ and 5.7, respectively. The IGM corrected histograms of $z = 3.1$ and 3.7 appear to be comparable within the large uncertainties of our measurements. The histogram of $z = 5.7$ (red histogram) would be systematically different from those of $z = 3.1$ and 3.7, and could imply that $z = 5.7$ LAEs may tend to have a large *intrinsic* EW_0 . However, the uncertainty of EW_0 measurements is as large as the difference of histograms between at $z = 3.7$ and $z = 5.7$. We cannot reject the possibility of no evolution of *intrinsic* EW_0 from $z = 3.7$ to 5.7.

We investigate the fraction of large-EW LAEs with the subsamples. We define a threshold of $EW_0^{\text{int}} \geq 240 \text{ \AA}$ with an *intrinsic* EW, following previous studies (e.g. Malhotra & Rhoads 2002; Dawson et al. 2004; Shimasaku et al. 2006; Saito et al. 2006). This threshold of EW_0^{int} corresponds to the *apparent* EW of $EW_0^{\text{app}} = 192 \text{ \AA}, 175 \text{ \AA},$ and 130 \AA , assuming the average attenuation of IGM (Section 5.1.2). We find that the fractions and errors of the large-EW LAEs in our subsamples are (z , fraction, fraction within 95th percentile) = (3.1, 0.21, 0.11-0.29), (3.7, 0.26, 0.16-0.40), and (5.7, 0.25, 0.15-0.33) by calculations of (i).⁴ From the calculations of (ii), we obtain the similar fractions of 0.20, 0.20, and 0.27 for $z = 3.1, 3.7,$ and 5.7 LAEs. There is a possible but slight implication of the evolution of the fraction of large-EW LAEs from $z = 3.7$ to 5.7 in the results of (ii). However, again, this possible evolution is very uncertain due to the large errors of EW measurements. The best estimates of the fraction are 20 – 30% for $z=3.1-5.7$. Thus, we conclude with these uncertainties that the fraction of large-EW LAEs is 10-40% at $z = 3.1 - 5.7$, which does not significantly change from $z = 3.1 - 5.7$ within this percent range.

We compare our fraction of large-EW LAEs with those of Shimasaku et al. (2006) for

⁴ The ranges of 95th percentile are obtained by bootstrap sampling.

$z = 5.7$ LAEs. Since Shimasaku et al. (2006) calculate this fraction with the threshold of *apparent* EW_0 of $\geq 120\text{\AA}$ (c.f. 130\AA in above calculations), we use this threshold of *apparent* $EW_0 \geq 120\text{\AA}$ here. With this threshold, we find the fraction and 95th-percentile range of 0.34 and 0.24-0.42 for our $z = 5.7$ LAEs. These numbers are vary consistent with those claimed by Shimasaku et al. (2006) who obtain 30-40%.

6.2. Relation between Ly α and UV-continuum emission

Figure 25 presents rest-frame Ly α EW (EW_0) as a function of UV-continuum magnitude for our spectroscopic samples. The effective wavelength of UV magnitude is $\sim 1300 - 1600\text{\AA}$. The details of UV-magnitude measurements are presented in Section 5.2. Figure 25 also plots EW_0 from previous studies of dropout galaxies and LAEs. On the right panel of Figure 25, EW_0 of $z \sim 6$ objects show a clear deficit of large EW_0 objects in the bright magnitude ($M_{UV} \lesssim -21.5$). This trend is found by Ando et al. (2006) for $z = 5 - 6$ galaxies, and discussed in Shimasaku et al. (2006); Stanway et al. (2007) for $z \sim 6$ objects. We confirm their findings on our plot of $z \sim 6$ objects. For $z \sim 3$ and 4 objects shown in Figure 25, we find the trend very similar to that of $z \sim 6$. We see no large EW_0 objects with $EW_0 \gtrsim 80\text{\AA}$ for UV-bright ($M_{UV} \lesssim -21.5$) objects. At $z = 3$, this trend is also reported by Shapley et al. (2003) who find that the Ly α emission strength increases toward fainter magnitudes in their spectra of LBGs.

6.3. UV-Continuum Color and Extinction

We present UV-continuum colors as a function of UV magnitude for our spectroscopically identified LAEs at $z = 3.1$ and 3.7 in Figure 26. This figure compares those of dropout galaxies at the similar redshift. Except for AGN, typical $z = 3 - 4$ LAEs have $i' - z'$ (or $R - i'$) colors of $\lesssim 0.05$. The UV-continuum colors of our LAEs are consistent with those of $z = 4.5$ LAEs (Finkelstein et al. 2007). On the other hand, dropout galaxies (or LBGs) generally have colors of $\simeq 0.1$. Thus, LAEs appear to be bluer than dropout galaxies in a UV-continuum color. This color difference indicates that LAEs are younger or less-dusty than dropout-galaxy population. We discuss more details in Section 7.5.

6.4. Composite Spectra

We make a composite spectrum each for our $z = 3.1$, 3.7 , and 5.7 LAEs. From our spectroscopic samples, we exclude AGNs (Table 4) and LAEs with uncertain identification (Table 2). We also do not include the spectrum of NB503-N-42377 that has a marginal CIV line, so as to obtain the average of typical LAE spectra (see Section 4.1). Thus, we use 36, 25, and 15 spectra of $z = 3.1$, 3.7 , and 5.7 , respectively. Since some of spectra have systematic differences originated from a faint AGN and/or errors of cosmic rays and subtraction of sky etc., we calculate a mean flux with rejections of two largest and smallest values at each wavelength. Figure 27 shows the composite spectra of our LAEs whose average redshifts are $\langle z \rangle = 3.13$, 3.68 , and 5.68 . We have also performed the median stacking, and find no qualitative differences between the rejected-mean and median results. The Ly α luminosity of the composite spectrum is $L(\text{Ly}\alpha) = (6.3 \pm 0.1, 8.5 \pm 0.2, 9.5 \pm 0.3) \times 10^{42} \text{ erg s}^{-1}$ at $\langle z \rangle = (3.13, 3.68, 5.68)$. We have a signal-to-noise ratio high enough to detect UV continua in $\langle z \rangle = 3.13$ and 3.68 spectra, but not in $\langle z \rangle = 5.68$ spectrum.

The composite spectrum of $\langle z \rangle = 5.68$ LAEs has Ly α emission line with a clear asymmetry, which is a typical emission feature of high- z objects. The spectra of $\langle z \rangle = 3.13$ and 3.68 do not show a significant asymmetry in Ly α . This is because a typical spectral resolution of our $z = 3.1$ and 3.7 LAEs is not high enough to resolve the asymmetry of Ly α ($R \sim 500$; c.f. $R \sim 1000$ for $z = 5.7$ LAEs). Moreover, the IGM absorption at $z = 3 - 4$ is not as strong as $z = 5.7$, which provides a weak asymmetric feature in Ly α emission at $z = 3 - 4$.

We find no significant absorption lines in these composite spectra, probably due to the combination of the weak metal absorption of LAEs and the relatively poor signal-to-noise ratios of our composite spectra.⁵ The composite spectra of $\langle z \rangle = 3.13$ and 3.68 cover the wavelength of HeII $\lambda 1640$ emission. The inset panels of Figure 27 magnify the spectra around this wavelength. No significant feature is found for HeII at $\langle z \rangle = 3.13$ and 3.68 . We calculate upper limits of HeII flux, f_{HeII} , and estimate the 3σ upper limits of the ratio, $f_{\text{HeII}}/f_{\text{Ly}\alpha}$, where $f_{\text{Ly}\alpha}$ is Ly α flux. We obtain meaningful 3σ upper limits of the ratio, $f_{\text{HeII}}/f_{\text{Ly}\alpha} = 0.02$ and 0.06 for $\langle z \rangle = 3.13$ and 3.68 LAEs, respectively. Since HeII emission is an indicator of primordial populations, i.e. population III stars and cooling radiation, our upper limits place constraints on primordial populations at $z = 3 - 4$. Although theoretical models predict the existence of primordial populations at these redshifts (Scannapieco et al. 2003; Jimenez & Haiman 2006), we have found no signature at the level of the upper limits of the present observations. Since the ratio of $f_{\text{HeII}}/f_{\text{Ly}\alpha}$ is predicted as small as $\sim 0.1 - 0.001$ for population III star formation and cooling radiation (e.g. Schaerer 2003; Yang et al. 2006),

⁵ The SiII absorption of $\langle z \rangle = 3.13$ LAE may exist, but the significance level is not high.

we need future surveys whose upper limits reach at the level of $f_{\text{HeII}}/f_{\text{Ly}\alpha} \simeq 0.001$.

7. Discussion

7.1. Evolution of Luminosity Functions

We have found four pieces of evidence that provide a general picture in the evolution of LAEs: (1) *apparent-Ly α* LFs of LAEs show no evolution from $z = 3.1$ to 5.7 . (2) These *apparent-Ly α* LFs and the average Gunn-Peterson optical depth indicate that *intrinsic-Ly α* LFs of LAEs must have brighten in the luminosity and/or increased in the number density from $z = 3.1$ to 5.7 . (3) The UV LFs of LAEs show the increase of luminosity and/or number densities from $z = 3.1$ to 5.7 . (4) The rest-frame *intrinsic-Ly α* EW, EW_0^{int} , distribution of LAEs does not change or positively evolves from $z = 3.1$ to 5.7 .

The evolution of *intrinsic-Ly α* LFs is caused by the emergence of Ly α emitting objects with a bright UV continuum or the increasing trend of Ly α EW_0 for LAEs at $z \sim 5.7$. There are three possible explanations for the evolution of LAEs. First, the amount of dust mixed in HII regions may decrease in average from $z = 3.1$ to 5.7 , and the extinction of Ly α luminosity through the resonance scattering decreases selectively. This implies that at $z = 5.7$ even UV bright galaxies have a detectable Ly α emission line. The second explanation is that the young Universe at $z = 5.7$ has numerous exotic Ly α populations such as metal-poor population III and/or cooling clouds. The third explanation is that the fraction of Ly α -absorbed galaxies is lower at higher redshifts, due to an decrease in the amount of HI gas in and around galaxies with redshift. In fact, some $z \sim 3$ LAEs show such an HI absorption originating from an inflow and/or outflow in their spectra (e.g. Tapken et al. 2007), although the evolution of such HI clouds has not been observationally understood. The CDM-based hierarchical model predicts that galaxies at higher redshifts are generally more compact (e.g. Mo et al. 1998; Somerville et al. 2006). It is possible that the star formation in such compact high- z galaxies is so efficient that cold gas is immediately converted into stars. If high- z LAEs are such compact galaxies, they will have little HI gas and thus their Ly α emission from HII regions can escape without absorption. If this hypothesis is true, we may be able to explain the evolutionary connection between LAEs and dropouts: the internal mass density of LAEs decreases with cosmic time by mergers and thus they evolve into dropout galaxies that are more massive and have more HI gas.

It should be noted that the evolutionary trend of UV-LF of LAEs is opposite to that of dropout galaxies. The UV-LFs of dropout galaxies show a significant decrease in luminosity and/or number density from $z \sim 4$ to $z \sim 6$ (e.g. Lehnert & Bremer 2003; Ouchi et al.

2004a; Shimasaku et al. 2005; Bunker et al. 2004). In case of luminosity evolution, UV-LFs of dropouts get faint from $z \sim 3$ to 6 by a factor of $1.7_{-0.3}^{+0.4}$ (Bouwens et al. 2006). On the other hand, UV-LFs of LAEs brighten by ~ 1 magnitude, if it comes from the pure luminosity evolution. This difference of LFs implies that Ly α emitting population is more dominant at $z = 6$ than $z = 3$ at the given UV luminosity range.

7.2. AGN fraction and Evolution of Faint AGN

We identify 6 AGN-LAEs in total. In our photometric samples of LAEs (satisfying our color-selection criteria), we find that 3 out of 356 $z = 3.1$ LAEs and 1 out of 101 $z = 3.7$ LAEs host AGNs (Section 4.6). Thus, the fraction of AGNs is about 1% at $z = 3.1$ and 3.7, which is consistent with the result of Gawiser et al. (2006). Note that the detection limits of our LAEs reach $(1 - 4) \times 10^{42}$ ergs s $^{-1}$ ($\sim 0.2 - 0.4L_{\text{Ly}\alpha}^*$). This AGN fraction is the lower limit, since our multi-wavelength data are probably not deep enough to identify faint AGNs. We estimate the relation between Ly α luminosity and the detection limits of our multi-wavelength data. By the comparison of our detection limits and the QSO templates in Figure 14 (see Section 4.6 for the definition of QSO templates), our X-ray data likely reach the deepest detection limit for AGNs among our multi-wavelength data. We normalize the QSO templates to the detection limit of our X-ray data, and measure Ly α luminosities of the QSO templates. We find Ly α -luminosity limits of $L(\text{Ly}\alpha) = 9.5 \times 10^{42}$ and 1.5×10^{43} erg s $^{-1}$ for $z = 3.1$ and 3.7 objects, respectively, assuming that the SED of AGN-LAEs is the same as the QSO templates. Down to these Ly α -luminosity limits, we find 3 out of 25 (1 out of 8) photometrically selected LAEs have an AGN at $z = 3.1$ ($z = 3.7$). Thus, the AGN fraction is estimated to be $\sim 10\%$ down to $L(\text{Ly}\alpha) \simeq 1 \times 10^{43}$ erg s $^{-1}$ for $z = 3.1$ and 3.7 LAEs. This Ly α -luminosity limit corresponds to $\simeq 2L_{\text{Ly}\alpha}^*$. Note that the AGN fraction of LAEs is as small as 10% even with this bright detection limit of Ly α luminosity.

If we take a Ly α limit for the very bright luminosity of $\log L(\text{Ly}\alpha) > 43.6$ and > 43.4 erg s $^{-1}$ in our $z = 3.1$ and 3.7 samples, respectively, all of LAEs (2 out of 2 LAEs and 1 out of 1 LAE at $z = 3.1$ and 3.7) have AGN activities. These very bright limits correspond to the brightest bins of our LF in Figure 19 (see Section 5.1). There appear possible humps of LF at $z = 3.1$ and 3.7 which are produced by the AGN-LAEs. The number density in these brightest bins is about $\sim 10^{-5}$ Mpc $^{-3}$. Thus, a shallow wide-field LAE survey generally finds this AGN-LAE population.

Steidel et al. (2002) have obtained the fraction of AGNs in their $z = 3$ LBG samples down to $\simeq M^* + 1$ with optical spectra. They have found the AGN fraction of 3% for their LBG sample with a relatively faint continuum limit of $\simeq M^* + 1$. Since the detection limits

of this study is different from ours, we cannot directly compare the AGN fraction of their LBGs and our LAEs. Since we find the AGN fraction (and its lower limit) of our LAEs is 10% (and $\gtrsim 1\%$) for our $\simeq 2L_{\text{Ly}\alpha}^*$ (and the entire [$\sim 0.2 - 0.4L_{\text{Ly}\alpha}^*$]) samples, the AGN fraction of LAEs and LBGs would be comparable.

For $z = 5.7$ LAEs, we identify no AGN with our spectra or multi-wavelength data. In the same manner as the calculations above, we estimate a Ly α detection limit of $z = 5.7$ LAEs that corresponds to the X-ray luminosity limit with the QSO templates. We find that the Ly α detection limit is $L(\text{Ly}\alpha) \sim 4 \times 10^{43} \text{ erg s}^{-1}$, but we have no LAEs with $L(\text{Ly}\alpha) > 4 \times 10^{43} \text{ erg s}^{-1}$. On the other hand, there are two AGN-LAEs that are brighter than $L(\text{Ly}\alpha) \sim 4 \times 10^{43} \text{ erg s}^{-1}$ (i.e. $\log L(\text{Ly}\alpha) > 43.6 \text{ erg s}^{-1}$) at $z = 3.1$. Therefore, it may imply that LAEs with a bright AGN such found at $z = 3$ would disappear at $z = 5.7$. In fact, no AGN signatures such as NV emission have been confirmed in spectra of the brightest $z = 5.7$ LAEs that are found in other wide-field studies (Westra et al. 2006). No detection of AGN in $z = 5.7$ LAEs implies that the number density of LAEs with AGN activities would drop from $z = 3$ to 5.7. Recent QSO surveys have measured QSO luminosity functions accurately, and found that the space density of bright QSOs with $M_{\text{UV}} < -26.7$ decreases from $z = 3$ to 6 by more than an order of magnitude (e.g. Croom et al. 2004; Fan et al. 2001, 2004). This trend is the same as that of our finding in our LAE samples. Because our AGN-LAEs are as faint as $M_{\text{UV}} \simeq -23 - -21$, our AGN-LAEs probe for evolution of relatively faint AGN. Thus, evolution of faint AGNs appears to follow the evolution of QSOs. This faint-AGN evolution implies that not only bright QSOs but also faint AGNs can provide less significant contribution than star-forming galaxies for reionizing the Universe at $z \gtrsim 6$. In other words, UV radiation from star formation likely becomes more dominant than that from faint AGNs at $z \sim 6$.

7.3. Star-Formation Rates Indicated from Multi-Wavelength Data

In Section 4, we have identified AGNs with our multi-wavelength data. The multi-wavelength data are too shallow to identify star-forming activities at high redshifts. The limiting SFRs of our multi-wavelength are as large as $\sim 10^4 M_{\odot} \text{ yr}^{-1}$ for our X-ray and $24\mu\text{m}$ data and $\sim 1000 M_{\odot} \text{ yr}^{-1}$ for our radio data, respectively. However, we find that our radio data provide a meaningful limit on SFR of our LAEs by stacking analysis. We exclude LAEs with an individual radio detection, and stack radio images of our photometrically selected LAEs in the same manner as Simpson et al. (2006b). The stacked images show no detection in the radio band. The 3σ -upper limits of the stacked images are $\langle f_{1.4\text{GHz}} \rangle = (1.8, 7.0, 2.7) \mu\text{Jy}$ for our $z = (3.1, 3.7, 5.7)$ LAEs.

The relationship between SFR and radio luminosity ($L_{1.4\text{GHz}}$) is given by

$$SFR(M_{\odot}\text{yr}^{-1}) = \frac{L_{1.4\text{GHz}}(\text{W Hz}^{-1})}{5.3 \times 10^{21}(\nu/\text{GHz})^{-\alpha}}, \quad (11)$$

for high-mass stars ($M > 5M_{\odot}$; Condon 1992; see also Serjeant et al. 2002), where ν is the frequency and α is the non-thermal ratio spectral index ($\alpha \simeq 0.8$). Assuming this SFR v.s. radio-luminosity relation, we obtain 3σ upper limits of $\langle SFR \rangle = (29, 162, 160) M_{\odot}\text{yr}^{-1}$ for our $z = (3.1, 3.7, 5.7)$ LAEs. Thus, the average SFRs of LAEs are smaller than $\simeq 30$ and $160 M_{\odot}\text{yr}^{-1}$ at $z = 3.1$ and $3.7/5.7$, respectively. The result of our $z = 5.7$ LAEs is similar to that of Carilli et al. (2006) who report the 2σ upper limit of $\langle f_{1.4\text{GHz}} \rangle = 2.5 \mu\text{Jy}$ (i.e. $\sim 100 M_{\odot}\text{yr}^{-1}$) for their stacked radio image of $z = 5.7$ LAEs in COSMOS field. The upper limits of radio SFR are consistent with the SFRs of typical (L^*) LAEs, $\simeq 5 - 10 M_{\odot}\text{yr}^{-1}$ (Section 5.3), estimated from UV and $\text{Ly}\alpha$ luminosities. This agreement between radio and optical SFRs implies that majority of LAEs are not associated with dusty starbursts with significant ($\times 10 - 100$) hidden star-formation. It is consistent with the fact that no LAEs are detected in submm bands (Section 4.4). These results support the small-dust extinction of LAEs from the blue UV-continuum color (Section 7.5). On the other hand, no significant excess of radio SFR may reject the possibility of an extremely-top heavy initial mass function for star-formation of LAEs, since radio fluxes are originated from non-thermal radiation of supernovae at the final stage of massive stars.

No radio detections in the stacked images also suggest that typical LAEs do not harbor low-luminosity radio AGNs at $z = 3.1 - 5.7$ (see also Carilli et al. 2006 for $z = 5.7$ LAEs). The radio fluxes of our AGN-LAEs are $f_{1.4\text{GHz}} \simeq 100 - 200 \mu\text{Jy}$ (Table 4) at $z = 3.1$ and 3.7 , while our 3σ upper limits of stacked images are $1.8 - 7.0 \mu\text{Jy}$. Thus, typical LAEs do not have a low-luminosity radio AGN whose flux is brighter than $1/10 - 1/100$ of typical radio AGN-LAEs at $z = 3 - 4$.

7.4. $\text{Ly}\alpha$ Emissivity

Figure 25 shows that UV-bright ($M_{\text{UV}} \lesssim -21.5$) galaxies do not have a large EW_0 ($EW_0 \gtrsim 80\text{\AA}$) at $z = 3 - 6$. Ando et al. (2006) suggest that UV-bright galaxies are a dusty and chemically-evolved population, and that such UV-bright galaxies do not have a large EW. There are two other possibilities to explain this trend. First, the average stellar population of UV-bright galaxies would be older than that of UV-faint galaxies. Since $\text{Ly}\alpha$ emission can be efficiently produced by hard-UV continuum from early-type stars, galaxies can emit a strong $\text{Ly}\alpha$ emission of $EW_0 \gtrsim 100\text{\AA}$ within ~ 10 Myr after a starburst (Schaerer 2003). Second, HI clouds of inter-stellar medium or inflows may be rich in UV bright population,

and absorb a Ly α emission line. It is likely that the combination of age, neutral hydrogen, dust, and metallicity makes the deficit of large EW galaxies at bright UV magnitude.

7.5. Implications from the Blue UV continuum

We find that UV-continuum colors of LAEs are bluer than those of dropout galaxies in Section 6.3. This implies that LAEs are less-dusty and/or younger population than dropout galaxies. Although more detailed analysis with near-infrared data and population synthesis models will be presented in Ono et al. (in preparation), we compare the UV-continuum colors of LAEs with a simple model. Ouchi et al. (2004a) have obtained the relation between $i' - z'$ color and dust extinction, $E(B - V)$, with the stellar population synthesis model (Bruzual & Charlot 2003) and the extinction law (Calzetti et al. 2000) which reproduce a typical UV-optical SED of dropout galaxies at $z \sim 3$. The relation of color and dust extinction is,

$$E(B - V) \simeq 0.0162 + 1.18(i' - z'), \quad (12)$$

Ouchi et al. (2004a) also confirm that this relation agrees with the one of local starbursts. This relation assumes that the difference of UV color (or UV slope) is caused by dust extinction, since the model fixes the age, metallicity, initial mass function, and star-formation history. We apply this simple model to our LAEs in Figure 26. Figure 26 implies that LAEs have an extinction of $E(B - V) \lesssim 0.05$, while that dropout galaxies typically have $E(B - V) \sim 0.1 - 0.2$. There are some very blue LAEs whose UV colors scatter around $-0.2 - 0.0$. The colors of these objects are still comparable to the color of $E(B - V) = 0.0$ within a $\simeq 2\sigma$ level. However, if this very blue UV color is true, the colors of LAEs can be explained not only by extinction, but also by stellar population that is bluer than that of typical dropout galaxies. Gronwall et al. (2007) estimate $E(B - V)$ of $z = 3.1$ LAEs with the independent approach, i.e. the comparison of UV and Ly α luminosity. They have obtained $E(B - V) < 0.05$, which is consistent with ours.

8. Conclusions

We have made a photometric sample of 858 LAE candidates and a spectroscopic sample of 84 confirmed LAEs at $z = 3.1, 3.7,$ and 5.7 down to $L(\text{Ly}\alpha) \gtrsim 3 \times 10^{42} \text{ erg s}^{-1}$ in a 1 deg^2 sky of the Subaru XMM-Newton Deep Survey Field. Based on these samples, we have studied photometric and spectroscopic properties with the aid of multi-wavelength data from X-ray to radio. The major findings of our study are summarized below.

1. We derive the LF of Ly α emission for each redshift and provide the best-fit Schechter parameters as summarized in Table 5, by carefully taking into account the statistical error and the field-to-field variation. We find that the *apparent* Ly α LF shows no significant evolution between $z = 3.1$ and 5.7 . Evolution, if any, is limited within factors of 1.8 and 2.7 in L^* and ϕ^* , respectively. Although no evolution of the Ly α LF over $3 \lesssim z \lesssim 5.7$ has already been suggested by previous studies, we now have much stronger and more reliable constraints with smaller systematic and statistical errors. Since the average Ly α opacity of the IGM is larger at earlier epochs, the absence of evolution in the apparent Ly α LF implies an intrinsic brightening of Ly α luminosity with increasing redshift being canceled out by increasing absorption of the IGM. We note, however, that this claim is true only if the two assumptions made in Section 5.1.2 are correct.

2. The LF of UV continuum for LAEs shows an increase in number density and/or UV luminosity from $z \sim 3 - 4$ to 5.7 . This evolution of the UV LF is consistent with the plausible evolution in the *intrinsic* Ly α LF, since we find that the distribution of the rest-frame *intrinsic* EW of LAEs does not change or positively evolves with redshift. On the other hand, the UV LF of dropout galaxies is known to show an opposite evolutionary trend to that of LAEs, namely, a decrease in number density and/or UV luminosity with increasing redshift. This implies that the ratio in number density of LAEs to dropout galaxies increases from $z \sim 3 - 4$ to 5.7 , and that galaxies with Ly α emission are more common at earlier epochs.

3. We identify six LAEs (in total) with AGN activities. In our photometric sample, three out of 356 $z = 3.1$ LAEs and one out of 101 $z = 3.7$ LAEs host AGNs. Thus, the lower limit of the AGN fraction down to $(1 - 4) \times 10^{42}$ erg s $^{-1}$ ($\sim 0.2 - 0.4L_{\text{Ly}\alpha}^*$) is $\simeq 1\%$ at $z = 3.1$ and 3.7 . We use QSO templates given in the literature to find that $\sim 10\%$ of LAEs are AGNs above the Ly α luminosity where our sample is complete, $L(\text{Ly}\alpha) \simeq 1 \times 10^{43}$ erg s $^{-1}$ ($\simeq 2L_{\text{Ly}\alpha}^*$). It is notable that 100% of LAEs (2 out of 2 LAEs and 1 out of 1 LAE at $z = 3.1$ and 3.7) host AGNs at the bright end of the LF with $\log L(\text{Ly}\alpha) > 43.6$ and > 43.4 erg s $^{-1}$ at $z = 3.1$ and 3.7 , respectively. Shallow and wide-field narrow-band imaging would be an efficient way to search for LAEs hosting AGNs.

4. We obtain the 3σ upper limits of stacked radio images, $\langle f_{1.4\text{GHz}} \rangle = (1.8, 7.0, 2.7)$ μJy for our $z = (3.1, 3.7, 5.7)$ LAEs. These upper limits indicate $\langle \text{SFR} \rangle = (29, 162, 160)$ $M_{\odot}\text{yr}^{-1}$ at $z = (3.1, 3.7, 5.7)$ based on the SFR-radio luminosity relation of Condon (1992). These upper limits are consistent with the SFRs estimated from Ly α and UV luminosities. Thus, the majority of LAEs are not associated with dusty starbursts with significant ($\times 10 - 100$) hidden star-forming activities. No radio detections in the stacked images also indicate that typical LAEs do not harbor a low-luminosity radio AGN at $z = 3.1 - 5.7$. At $z = 3 - 4$, typical

LAEs do not have a low-luminosity radio AGN whose flux is brighter than 1/10 – 1/100 of typical radio AGN-LAEs of our SXDS field.

5. The fraction of LAEs that have very large Ly α EWs does not change significantly over $3.1 \leq z \leq 5.7$; the fraction of objects with $EW_0^{\text{int}} \geq 240\text{\AA}$ is 10–40 %.

6. If we naively assume that all of the Ly α or UV emission in our LAEs originate from star-forming activities, LAEs contribute about $\simeq 20 - 40\%$ of the entire cosmic SFRDs at $z = 3 - 6$.

7. We find a deficit of large-EW galaxies with bright UV continuum emission at all three redshifts. This finding not only confirms the previous results of Shapley et al. (2003); Ando et al. (2006); Shimasaku et al. (2006) for $z = 3$ and $5 - 6$, but also claims that this trend is common in the early universe. This deficit is probably caused by a combination of old ages and large amount of neutral hydrogen, dust, and metallicity in UV-bright galaxies.

8. The UV-continuum colors of LAEs are generally bluer than those of dropout galaxies at the same UV luminosity. If we assume that LAEs have the same stellar population as dropout galaxies, then the UV spectral slope of LAEs indicates $E(B - V) \lesssim 0.05$. The very blue LAEs probably have extremely low dust extinction and/or very young stellar populations.

9. We stack the spectra of the confirmed LAEs to estimate the 3σ upper limit of $f_{\text{HeII}}/f_{\text{Ly}\alpha}$ to be 0.02 for $z = 3.1$ and 0.06 for $z = 3.7$. These low $f_{\text{HeII}}/f_{\text{Ly}\alpha}$ values are consistent with no or little primordial population being included in our sample.

We are grateful to Mark Dijkstra, Eric Gawiser, Kim Nilsson, and Edward Westra for their helpful comments. We thank the anonymous referee for his/her constructive suggestions and comments that improved this article. M.O. has been supported by the Hubble Fellowship program through grant HF-01176.01-A awarded by the Space Telescope Science Institute, which is operated by the Association of Universities for Research in Astronomy, Inc. under NASA contract NAS 5-26555. M.O. acknowledge support via Carnegie Fellowship.

REFERENCES

- Ajiki, M., et al. 2003, AJ, 126, 2091
Ajiki, M., et al. 2004, PASJ, 56, 597

- Ajiki, M., Mobasher, B., Taniguchi, Y., Shioya, Y., Nagao, T., Murayama, T., & Sasaki, S. S. 2006, *ApJ*, 638, 596
- Ando, M., Ohta, K., Iwata, I., Akiyama, M., Aoki, K., & Tamura, N. 2006, *ApJ*, 645, L9
- Bardeen, J. M., Bond, J. R., Kaiser, N., & Szalay, A. S. 1986, *ApJ*, 304, 15
- Beckwith, S. V. W., et al. 2006, *AJ*, 132, 1729
- Bertin, E. & Arnouts, S. 1996, *A&AS*, 117, 393
- Bohlin, R. C., Colina, L., & Finley, D. S. 1995, *AJ*, 110, 1316
- Bouwens, R. J., Illingworth, G. D., Blakeslee, J. P., & Franx, M. 2006, *ApJ*, 653, 53
- Brocklehurst, M. 1971, *MNRAS*, 153, 471
- Bruzual A., G. & Charlot, S. *MNRAS*, submitted
- Bunker, A. J., Stanway, E. R., Ellis, R. S., & McMahon, R. G. 2004, *MNRAS*, 355, 374
- Calzetti, D., Armus, L., Bohlin, R. C., Kinney, A. L., Koornneef, J., & Storchi-Bergmann, T. 2000, *ApJ*, 533, 682
- Calzetti, D. 2001, *PASP*, 113, 1449
- Carilli, C. L., et al. 2006, *ArXiv Astrophysics e-prints*, arXiv:astro-ph/0612346
- Charlot, S., & Fall, S. M. 1993, *ApJ*, 415, 580
- Chary, R.-R., Stern, D., & Eisenhardt, P. 2005, *ApJ*, 635, L5
- Coleman, G. D., Wu, C.-C., & Weedman, D. W. 1980, *ApJS*, 43, 393
- Condon, J. J. 1992, *ARA&A*, 30, 575
- Coppin, K., et al. 2006, *MNRAS*, 372, 1621
- Cowie, L. L. & Hu, E. M. 1998, *AJ*, 115, 1319
- Croom, S. M., Smith, R. J., Boyle, B. J., Shanks, T., Miller, L., Outram, P. J., & Loaring, N. S. 2004, *MNRAS*, 349, 1397
- Dawson, S., et al. 2004, *ApJ*, 617, 707
- Dawson, S. A. 2005, Ph.D. Thesis, University of California, Berkley

- Daddi, E., et al. 2007, ArXiv e-prints, 705, arXiv:0705.2831
- Dey, A., et al. 2005, ApJ, 629, 654
- Dijkstra, M., & Wyithe, J. S. B. 2007, MNRAS, 379, 1589
- Dow-Hygelund, C. C., et al. 2006, ArXiv Astrophysics e-prints, arXiv:astro-ph/0612454
- Ellis, R., Santos, M. R., Kneib, J.-P., & Kuijken, K. 2001, ApJ, 560, L119
- Elvis, M., et al. 1994, ApJS, 95, 1
- Fan, X., et al. 2001, AJ, 121, 54
- Fan, X., et al. 2004, AJ, 128, 515
- Fan, X., et al. 2006, AJ, 132, 117
- Finkelstein, S. L., Rhoads, J. E., Malhotra, S., Pirzkal, N., & Wang, J. 2007, ApJ, 660, 1023
- Fukugita, M., Shimasaku, K., & Ichikawa, T. 1995, PASP, 107, 945
- Gronwall, C., et al. 2007, ArXiv e-prints, 705, arXiv:0705.3917
- Gunn, J. E. & Stryker, L. L. 1983, ApJS, 52, 121
- Gawiser, E., et al. 2006, ApJ, 642, L13
- Hopkins, A. M. 2006, ArXiv Astrophysics e-prints, arXiv:astro-ph/0611283
- Hu, E. M., Cowie, L. L., McMahon, R. G., Capak, P., Iwamuro, F., Kneib, J.-P., Maihara, T., & Motohara, K. 2002, ApJ, 568, L75
- Hu, E. M., Cowie, L. L., Capak, P., McMahon, R. G., Hayashino, T., & Komiyama, Y. 2004, AJ, 127, 563
- Hu, E. M., & Cowie, L. L. 2006, Nature, 440, 1145
- Iverson, R. J., et al. 2007, ArXiv Astrophysics e-prints, arXiv:astro-ph/0702544
- Iye, M., et al. 2004, PASJ, 56, 381
- Iye, M., et al. 2006, Nature, 443, 186
- Jimenez, R., & Haiman, Z. 2006, Nature, 440, 501
- Kashikawa, N. et al. 2002, PASJ, 54, 819

- Kashikawa, N., et al. 2006, *ApJ*, 648, 7
- Kennicutt, R. C., Jr. 1998, *ApJ*, 498, 541
- Kinney, A. L., Calzetti, D., Bohlin, R. C., McQuade, K., Storchi-Bergmann, T., & Schmitt, H. R. 1996, *ApJ*, 467, 38
- Kodaira, K. et al. 2003, *PASJ*, 55, L17
- Kriek, M., et al. 2006, *ApJ*, 649, L71
- Kudritzki, R.-P., et al. 2000, *ApJ*, 536, 19
- Kurk, J. D., Cimatti, A., di Serego Alighieri, S., Vernet, J., Daddi, E., Ferrara, A., & Ciardi, B. 2004, *A&A*, 422, L13
- Lai, K., Huang, J.-S., Fazio, G., Cowie, L. L., Hu, E. M., & Kakazu, Y. 2006, *ArXiv Astrophysics e-prints*, arXiv:astro-ph/0610572
- LeFevre, O., et al. 2003, *Proc. SPIE*, 4841, 1670
- Lehnert, M. D., & Bremer, M. 2003, *ApJ*, 593, 630
- Lawrence, A., et al. 2006, *ArXiv Astrophysics e-prints*, arXiv:astro-ph/0604426
- Lonsdale, C. J., et al. 2003, *PASP*, 115, 897
- Madau, P. 1995, *ApJ*, 441, 18
- Madau, P., Pozzetti, L., & Dickinson, M. 1998, *ApJ*, 498, 106
- Maier, C. et al. 2003,
- Malhotra, S. & Rhoads, J. E. 2002, *ApJ*, 565, L71
- Malhotra, S., & Rhoads, J. E. 2004, *ApJ*, 617, L5
- Malhotra, S., et al. 2005, *ApJ*, 626, 666
- Martin, C. L., & Sawicki, M. 2004, *ApJ*, 603, 414
- Martin, C. L., Sawicki, M., Dressler, A., & McCarthy, P. J. 2006, *New Astronomy Review*, 50, 53
- Matsuda, Y., et al. 2004, *AJ*, 128, 569

- McCarthy, P. J. 1993, *ARA&A*, 31, 639
- Meiksin, A. 2006, *MNRAS*, 365, 807
- Miyazaki, S. et al. 2002, *PASJ*, 54, 833
- Mo, H. J., Mao, S., & White, S. D. M. 1998, *MNRAS*, 295, 319
- Murayama, T., et al. 2007, *ArXiv Astrophysics e-prints*, arXiv:astro-ph/0702458
- Nilsson, K. K., Fynbo, J. P. U., Møller, P., Sommer-Larsen, J., & Ledoux, C. 2006, *A&A*, 452, L23
- Nilsson, K. K., et al. 2007, *A&A*, 471, 71
- Oke, J. B. 1974, *ApJS*, 27, 21
- Oke, J. B. 1990, *AJ*, 99, 1621
- Ouchi, M. et al. 2003, *ApJ*, 582, 60
- Ouchi, M., et al. 2004a, *ApJ*, 611, 660
- Ouchi, M., et al. 2004b, *ApJ*, 611, 685
- Ouchi, M., et al. 2005a, *ApJ*, 620, L1
- Paltani, S., et al. 2006, *ArXiv Astrophysics e-prints*, arXiv:astro-ph/0608176
- Pascarelle, S. M., Windhorst, R. A., Keel, W. C., & Odewahn, S. C. 1996, *Nature*, 383, 45
- Rhoads, J. E., & Malhotra, S. 2001, *ApJ*, 563, L5
- Rhoads, J. E., et al. 2003, *AJ*, 125, 1006
- Richards, G. T., et al. 2003, *AJ*, 126, 1131
- Pirzkal, N., Malhotra, S., Rhoads, J. E., & Xu, C. 2006, *ArXiv Astrophysics e-prints*, arXiv:astro-ph/0612513
- Saito, T., Shimasaku, K., Okamura, S., Ouchi, M., Akiyama, M., & Yoshida, M. 2006, *ApJ*, 648, 54
- Saito, T., Shimasaku, K., Okamura, S., Ouchi, M., Akiyama, M., Yoshida, M., & Ueda, Y. 2007, *ArXiv e-prints*, 705, arXiv:0705.1494

- Santos, M. R., Ellis, R. S., Kneib, J.-P., Richard, J., & Kuijken, K. 2004, *ApJ*, 606, 683
- Sawicki, M., & Thompson, D. 2006, *ApJ*, 642, 653
- Scannapieco, E., Schneider, R., & Ferrara, A. 2003, *ApJ*, 589, 35
- Schaerer, D. 2003, *A&A*, 397, 527
- Schechter, P. 1976, *ApJ*, 203, 297
- Schlegel, D. J., Finkbeiner, D. P., & Davis, M. 1998, *ApJ*, 500, 525
- Serjeant, S., Gruppioni, C., & Oliver, S. 2002, *MNRAS*, 330, 621
- Shapley, A. E., Steidel, C. C., Pettini, M., & Adelberger, K. L. 2003, *ApJ*, 588, 65
- Shimasaku, K. et al. 2003, *ApJ*, 586, L111 (SDS IV)
- Shimasaku, K., Ouchi, M., Furusawa, H., Yoshida, M., Kashikawa, N., & Okamura, S. 2005, *PASJ*, 57, 447
- Shimasaku, K., et al. 2006, *PASJ*, 58, 313
- Simpson, C., et al. 2006a, *MNRAS*, 372, 741
- Simpson, C., et al. 2006b, *MNRAS*, 373, L21
- Somerville, R. S., et al. 2006, *ArXiv Astrophysics e-prints*, arXiv:astro-ph/0612428
- Stanway, E. R., Bunker, A. J., McMahon, R. G., Ellis, R. S., Treu, T., & McCarthy, P. J. 2004a, *ApJ*, 607, 704
- Stanway, E. R., et al. 2004b, *ApJ*, 604, L13
- Stanway, E. R., et al. 2007, *ArXiv Astrophysics e-prints*, arXiv:astro-ph/0701211
- Stark, D. P., Ellis, R. S., Richard, J., Kneib, J.-P., Smith, G. P., & Santos, M. R. 2007, *ApJ*, 663, 10
- Steidel, C. C., Adelberger, K. L., Giavalisco, M., Dickinson, M., & Pettini, M. 1999, *ApJ*, 519, 1
- Steidel, C. C., Adelberger, K. L., Shapley, A. E., Pettini, M., Dickinson, M., & Giavalisco, M. 2000, *ApJ*, 532, 170

- Steidel, C. C., Adelberger, K. L., Shapley, A. E., Pettini, M., Dickinson, M., & Giavalisco, M. 2003, ArXiv Astrophysics e-prints, 5378 (astro-ph/0305378)
- Taniguchi, Y., et al. 2005, PASJ, 57, 165
- Tapken, C., et al. 2006, A&A, 455, 145
- Tapken, C., Appenzeller, I., Noll, S., Richling, S., Heidt, J., Meinköhn, E., & Mehlert, D. 2007, A&A, 467, 63
- Telfer, R. C., Zheng, W., Kriss, G. A., & Davidsen, A. F. 2002, ApJ, 565, 773
- Tran, K.-V. H., Lilly, S. J., Crampton, D., & Brodwin, M. 2004, ApJ, 612, L89
- van Breukelen, C., Jarvis, M. J., & Venemans, B. P. 2005, MNRAS, 359, 895
- van Dokkum, P. G., et al. 2006, ApJ, 638, L59
- Vanzella, E., et al. 2006a, A&A, 454, 423
- Vanzella, E., Cristiani, S., Dickinson, M., Giavalisco, M., Lee, K., Nonino, M., Rosati, P., & the GOODS team 2006b, ArXiv Astrophysics e-prints, arXiv:astro-ph/0612182
- Venemans, B. P., et al. 2007, A&A, 461, 823
- Wang, J. X., et al. 2004, ApJ, 608, L21
- Westra, E., et al. 2005, A&A, 430, L21
- Westra, E., et al. 2006, A&A, 455, 61
- Willis, J., Courbin, F., Kneib, J.-P., & Minniti, D. 2006, New Astronomy Review, 50, 70
- Yagi, M., Kashikawa, N., Sekiguchi, M., Doi, M., Yasuda, N., Shimasaku, K., & Okamura, S. 2002, AJ, 123, 66
- Yamada, S. F., et al. 2005, PASJ, 57, 881
- Yan, H., & Windhorst, R. A. 2004, ApJ, 612, L93
- Yang, Y., Zabludoff, A. I., Davé, R., Eisenstein, D. J., Pinto, P. A., Katz, N., Weinberg, D. H., & Barton, E. J. 2006, ApJ, 640, 539
- Yoshida, M., et al. 2006, ApJ, 653, 988

Table 1. Summary of Imaging Observations and Data

Band	Field Name(s)	Exposure Time (sec)	PSF size [‡] (arcsec)	Area (arcmin ²)	m_{lim}^{\dagger} (5σ AB mag)	Date of Observations
<i>NB503</i>	SXDS-C	4200	0.79 (0.81)	657	25.3	2003 Oct 23
<i>NB503</i>	SXDS-N	4200	1.05 (1.05)	766	25.1	2003 Oct 23
<i>NB503</i>	SXDS-S	4200	0.91 (0.91)	827	25.3	2003 Oct 23
<i>NB503</i>	SXDS-E	4200	0.69 (0.83)	685	25.4	2003 Oct 24
<i>NB503</i>	SXDS-W	5400	0.67 (0.83)	603	25.5	2003 Oct 24
<i>NB570</i>	SXDS-C	4200	0.91 (0.91)	627	24.6	2003 Oct 22,26
<i>NB570</i>	SXDS-N	4200	0.91 (0.91)	781	24.9	2003 Oct 26
<i>NB570</i>	SXDS-S	5400	0.69 (0.81)	833	25.2	2003 Oct 22
<i>NB570</i>	SXDS-E	4200	0.75 (0.83)	674	24.9	2003 Oct 26
<i>NB570</i>	SXDS-W	4200	0.87 (0.87)	559	24.8	2003 Oct 26
<i>NB816</i>	SXDS-C	17182	0.65 (0.81)	676	26.0	2003 Sep 28-30, Oct 22
<i>NB816</i>	SXDS-N	14400	0.73 (0.85)	810	26.0	2003 Sep 29, Oct 22
<i>NB816</i>	SXDS-S	14400	0.65 (0.81)	835	26.1	2003 Sep 28,30 Oct 22
<i>NB816</i>	SXDS-E	14255	0.67 (0.83)	722	26.0	2003 Sep 29-30, Oct 22
<i>NB816</i>	SXDS-W	20400	0.69 (0.83)	678	25.9	2003 Sep 30, Oct 22
Archival broad-band data ^{††} .						
<i>B</i>	SXDS-C,N,S,E,W	19800 – 20700	0.78 – 0.84	915 – 979	27.5 – 27.8	...
<i>V</i>	SXDS-C,N,S,E,W	17460 – 19260	0.72 – 0.82	915 – 979	27.1 – 27.2	...
<i>R</i>	SXDS-C,N,S,E,W	13920 – 14880	0.74 – 0.82	915 – 979	27.0 – 27.2	...
<i>i'</i>	SXDS-C,N,S,E,W	18540 – 38820	0.68 – 0.82	915 – 979	26.9 – 27.1	...
<i>z'</i>	SXDS-C,N,S,E,W	11040 – 18660	0.70 – 0.76	915 – 979	25.8 – 26.1	...

[‡]The FWHM of PSFs in the reduced image. The value in parenthesis indicates the FWHM of PSF that is matched with broad-band images in each field.

[†]The limiting magnitude defined by a 5σ sky noise in a $2''$ -diameter circular aperture.

^{††}The archival broad-band data of SXDS presented in Furusawa et al. (in preparation). We summarize the properties of the 5-field images on a single line. Note that the exposure time is *not* a total of the 5 fields, but 1 field. More details are presented in Table 2 of Furusawa et al. in preparation.

Table 2. Ly α Emitters with spectroscopic redshifts

Object Name	α (J2000) ^a	δ (J2000) ^a	z^\dagger	m_{NB} (mag)	m_{BB} (mag)	S_{NB}^\dagger (kpc)	S_{BB}^\dagger (kpc)	$L(\text{Ly}\alpha)$ (10^{42}erg s^{-1})	EW_0^{app} (\AA)	M_{UV} (mag)	SFR ($M_\odot\text{yr}^{-1}$)	Note
(1)	(2)	(3)	(4)	(5)	(6)	(7)	(8)	(9)	(10)	(11)	(12)	(13)
$z = 3.1$ LAEs												
NB503-C-112924	02:18:50	-04:50:54	3.134	24.9	27.8	4.1	...	3.0 ± 0.5	$264.6^{+171.2}_{-84.3}$	-18.0	0.9	...
NB503-C-114646	02:17:44	-04:50:32	3.135	23.9	25.4	4.1	$\lesssim 4$	6.6 ± 0.5	$55.9^{+5.1}_{-5.0}$	-20.2	6.5	...
NB503-C-15140	02:18:58	-05:12:26	3.147	23.6	25.6	4.4	$\lesssim 4$	9.0 ± 0.8	$62.9^{+6.3}_{-6.1}$	-20.2	6.5	...
NB503-C-29891	02:17:21	-05:09:12	3.105	23.7	25.9	7.1	$\lesssim 4$	14.8 ± 2.1	$124.8^{+19.4}_{-17.2}$	-19.7	4.2	...
NB503-C-33149	02:18:39	-05:08:27	3.141	24.6	26.6	6.9	4.5	3.5 ± 0.6	$76.3^{+16.6}_{-14.3}$	-19.0	2.1	...
NB503-C-46996	02:18:33	-05:04:57	3.129	23.9	25.6	4.3	4.3	5.9 ± 0.7	$47.2^{+6.3}_{-6.0}$	-20.0	5.4	...
NB503-C-49497	02:18:06	-05:04:08	3.129	21.8	24.4	8.3	6.2	44.4 ± 1.3	$62.6^{+2.1}_{-1.9}$	-21.7	(25.3)	AGN
NB503-C-51702	02:18:07	-05:03:49	3.125	24.4	25.8	5.4	$\lesssim 4$	3.5 ± 0.7	$37.6^{+7.4}_{-6.3}$	-20.1	6.2	...
NB503-C-52511	02:17:12	-05:03:37	3.125	24.7	26.8	5.6	$\lesssim 4$	3.2 ± 0.5	$104.3^{+26.8}_{-20.8}$	-18.8	1.7	...
NB503-C-53382	02:17:05	-05:03:25	3.152	24.5	25.5	4.7	4.6	4.4 ± 0.5	$41.8^{+5.1}_{-5.5}$	-20.1	6.2	...
NB503-C-57309	02:17:08	-05:02:26	3.136	24.6	25.8	7.3	4.3	3.3 ± 0.5	$39.7^{+6.5}_{-6.3}$	-20.1	6.0	...
NB503-C-66311	02:17:27	-05:00:21	3.144	24.6	26.4	5.1	$\lesssim 4$	3.5 ± 0.5	$69.1^{+14.0}_{-12.0}$	-19.2	2.7	...
NB503-C-88741	02:17:00	-04:55:40	3.113	23.6	25.6	$\lesssim 4$	$\lesssim 4$	11.7 ± 0.7	$128.2^{+11.4}_{-10.7}$	-20.1	6.2	...
NB503-C-90464	02:17:43	-04:55:21	3.111	24.8	27.1	4.1	...	4.2 ± 0.8	$204.2^{+72.1}_{-53.8}$	-18.6	1.6	...
NB503-C-99469	02:18:03	-04:53:31	3.133	24.9	27.2	4.5	...	2.7 ± 0.5	$137.2^{+31.3}_{-34.5}$	-18.4	1.2	...
NB503-E-161419	02:20:24	-04:52:05	3.105	24.6	26.3	4.6	4.2	6.1 ± 1.8	$86.2^{+26.0}_{-23.6}$	-19.4	3.2	...
NB503-E-49946	02:19:09	-04:47:22	3.152	24.3	26.0	4.7	4.6	5.2 ± 0.7	$65.2^{+9.9}_{-9.3}$	-19.5	3.5	...
NB503-E-60750	02:19:16	-04:58:38	3.129	23.5	25.1	$\lesssim 4$	$\lesssim 4$	9.2 ± 0.6	$58.4^{+4.2}_{-3.9}$	-20.5	8.4	...
NB503-N-32683	02:17:41	-04:43:47	3.106	24.4	25.9	5.0	7.4	7.3 ± 1.0	$114.1^{+19.0}_{-16.4}$	-19.8	4.6	...
NB503-N-33460	02:17:27	-04:43:36	3.119	23.3	25.6	5.3	4.1	12.9 ± 0.6	$121.3^{+9.2}_{-9.0}$	-20.1	6.0	...
NB503-N-34067	02:17:44	-04:43:29	3.152	24.6	> 28.0	$\lesssim 4$...	4.4 ± 0.7	$343.0^{+292.7}_{-120.6}$	-17.6	0.6	...
NB503-N-35820	02:17:35	-04:42:59	3.102	23.6	25.3	6.6	6.1	21.1 ± 1.9	$135.5^{+12.8}_{-12.8}$	-20.8	(11.0)	AGN
NB503-N-42377	02:17:42	-04:41:08	3.154	22.2	23.9	4.2	4.4	38.8 ± 0.8	$73.6^{+1.5}_{-1.5}$	-21.8	29.0	Civ? [¶]
NB503-N-72492	02:17:42	-04:33:20	3.108	24.3	26.2	7.2	6.3	8.0 ± 1.0	$146.8^{+26.4}_{-22.2}$	-19.4	3.2	...
NB503-N-80475	02:17:41	-04:31:30	3.123	21.8	22.6	$\lesssim 4$	4.3	31.0 ± 0.6	$18.6^{+0.4}_{-0.3}$	-23.2	(100.7)	AGN
NB503-N-87126	02:17:54	-04:30:06	3.112	23.5	25.4	6.1	4.6	12.4 ± 1.1	$83.4^{+7.6}_{-7.6}$	-20.3	7.0	...
NB503-N-92276	02:17:42	-04:28:58	3.133	24.3	26.4	4.2	5.6	4.5 ± 0.7	$75.9^{+14.7}_{-11.9}$	-19.7	4.0	...
NB503-S-105705	02:17:06	-05:16:34	3.106	24.6	26.5	7.1	5.3	6.6 ± 1.3	$148.8^{+38.1}_{-30.1}$	-19.3	2.8	...
NB503-S-35558	02:18:18	-05:31:57	3.132	24.7	26.6	6.6	5.4	3.4 ± 0.5	$98.1^{+21.8}_{-18.0}$	-19.6	3.7	...
NB503-S-45244	02:18:26	-05:29:45	3.156	23.1	24.8	$\lesssim 4$	$\lesssim 4$	18.5 ± 0.6	$82.3^{+3.4}_{-3.4}$	-21.1	15.7	...
NB503-S-54416	02:17:05	-05:27:35	3.133	23.9	26.0	5.9	9.3	6.7 ± 0.6	$88.7^{+12.0}_{-9.5}$	-19.6	3.7	...
NB503-S-56809	02:17:57	-05:27:00	3.123	24.2	27.3	5.9	...	5.9 ± 0.8	$233.7^{+95.9}_{-50.7}$	-18.3	1.2	...
NB503-S-66012	02:17:23	-05:24:49	3.167	24.6	25.6	4.3	6.4	7.8 ± 1.0	$73.4^{+10.5}_{-10.1}$	-20.0	5.6	...
NB503-S-89393	02:19:04	-05:19:58	3.125	24.4	26.0	5.9	5.9	3.8 ± 0.8	$42.6^{+9.4}_{-8.2}$	-19.6	3.8	...
NB503-S-94275	02:18:41	-05:18:49	3.102	22.8	24.5	4.1	$\lesssim 4$	46.5 ± 1.9	$164.6^{+6.3}_{-6.6}$	-21.2	16.1	...
NB503-W-100818	02:16:04	-04:49:43	3.125	24.0	26.0	4.1	$\lesssim 4$	6.3 ± 0.6	$85.0^{+11.3}_{-10.3}$	-19.6	3.8	...
NB503-W-31855	02:16:52	-04:56:43	3.130	24.4	26.9	5.1	9.1	4.6 ± 0.6	$137.3^{+39.2}_{-27.6}$	-18.6	1.5	...
NB503-W-67066	02:16:27	-05:02:43	3.139	23.9	25.8	7.3	11.9	6.3 ± 0.8	$55.7^{+7.2}_{-7.2}$	-19.6	3.7	...
NB503-W-85295	02:16:14	-05:02:15	3.141	24.5	26.0	$\lesssim 4$	4.3	3.8 ± 0.6	$51.2^{+7.6}_{-8.2}$	-19.6	3.7	...
NB503-W-97848	02:16:06	-04:48:12	3.121	24.6	26.6	4.1	$\lesssim 4$	3.7 ± 0.6	$101.1^{+21.5}_{-19.3}$	-19.1	2.3	...
NB503-W-98167	02:16:06	-04:50:57	3.124	23.8	25.6	4.1	$\lesssim 4$	6.9 ± 0.7	$63.5^{+6.9}_{-6.5}$	-20.0	5.4	...

Table 2—Continued

Object Name	$\alpha(\text{J2000})^a$	$\delta(\text{J2000})^a$	z^\ddagger	m_{NB} (mag)	m_{BB} (mag)	S_{NB}^\dagger (kpc)	S_{BB}^\dagger (kpc)	$L(\text{Ly}\alpha)$ (10^{42}erg s^{-1})	EW_0^{app} (Å)	M_{UV} (mag)	SFR ($M_\odot\text{yr}^{-1}$)	Note
(1)	(2)	(3)	(4)	(5)	(6)	(7)	(8)	(9)	(10)	(11)	(12)	(13)
$z = 3.7$ LAEs												
NB570-C-107443	02:17:47	-04:52:30	3.648	23.4	24.3	4.7	$\lesssim 4$	33.6 ± 4.7	$75.2^{+10.8}_{-9.2}$	-21.7	26.7	...
NB570-C-116152	02:18:56	-04:50:59	3.683	24.5	26.4	4.1	$\lesssim 4$	4.7 ± 0.8	$87.3^{+17.3}_{-16.5}$	-19.6	3.7	...
NB570-C-13685	02:17:09	-05:12:29	3.691	23.9	27.6	5.7	...	8.3 ± 1.1	$335.6^{+182.9}_{-93.9}$	-18.3	1.1	...
NB570-C-30225	02:18:26	-05:10:03	3.699	23.0	24.8	5.7	4.7	19.0 ± 1.1	$57.7^{+3.6}_{-3.7}$	-21.2	16.1	...
NB570-C-40856	02:17:01	-05:07:28	3.686	24.0	26.8	4.8	4.5	7.2 ± 0.9	$161.8^{+36.1}_{-30.2}$	-19.2	2.6	...
NB570-C-78067	02:17:13	-04:58:53	3.684	23.5	24.6	5.7	4.5	7.9 ± 1.6	$14.4^{+2.5}_{-2.9}$	-21.1	15.5	...
NB570-E-103151	02:19:44	-04:50:55	3.669	23.2	25.8	4.6	$\lesssim 4$	21.9 ± 2.0	$150.0^{+16.1}_{-15.0}$	-20.1	6.0	...
NB570-E-142687	02:20:11	-04:50:08	3.644	24.4	25.4	5.6	4.2	16.6 ± 7.0	$95.4^{+36.8}_{-36.1}$	-20.5	8.8	...
NB570-E-169608	02:20:30	-04:48:15	3.702	24.6	26.8	5.3	5.0	4.7 ± 0.9	$110.4^{+29.6}_{-25.4}$	-19.2	2.7	...
NB570-E-58808	02:19:13	-04:51:59	3.692	23.3	25.7	$\lesssim 4$	$\lesssim 4$	14.2 ± 0.9	$126.4^{+11.1}_{-10.0}$	-20.4	7.8	...
NB570-E-62593	02:19:15	-04:55:11	3.672	23.6	25.5	6.0	$\lesssim 4$	12.8 ± 1.7	$67.4^{+9.2}_{-9.5}$	-20.7	10.6	...
NB570-E-65332	02:19:17	-05:07:39	3.693	23.8	25.9	$\lesssim 4$	$\lesssim 4$	9.1 ± 0.8	$92.8^{+10.7}_{-9.5}$	-20.1	6.1	...
NB570-N-33608	02:17:27	-04:44:14	3.683	24.0	25.9	5.7	$\lesssim 4$	7.1 ± 1.1	$63.1^{+10.1}_{-9.3}$	-20.0	5.5	...
NB570-N-34841	02:18:31	-04:43:54	3.724	21.8	22.2	$\lesssim 4$	$\lesssim 4$	145.0 ± 1.5	$48.9^{+0.7}_{-0.7}$	-23.8	(178.2)	AGN
NB570-N-42463	02:18:40	-04:42:11	3.692	24.4	26.4	4.4	$\lesssim 4$	4.7 ± 0.8	$82.7^{+17.1}_{-14.2}$	-19.6	3.9	...
NB570-N-86993	02:18:13	-04:30:57	3.668	23.8	25.7	5.2	$\lesssim 4$	11.5 ± 1.5	$90.7^{+12.8}_{-12.0}$	-20.4	7.6	...
NB570-S-125887	02:18:07	-05:20:48	3.638	24.3	25.2	5.9	4.4	28.4 ± 11.4	$147.9^{+48.7}_{-55.2}$	-20.8	11.0	...
NB570-S-132143	02:18:27	-05:19:47	3.677	23.4	25.9	4.1	$\lesssim 4$	14.2 ± 1.3	$118.9^{+14.1}_{-11.6}$	-20.0	5.5	...
NB570-S-141871	02:18:10	-05:18:13	3.684	24.5	26.9	$\lesssim 4$	$\lesssim 4$	4.6 ± 0.8	$134.4^{+39.3}_{-28.5}$	-18.9	2.1	...
NB570-S-154087	02:17:43	-05:16:11	3.682	24.9	27.3	3.3 ± 0.9	$141.3^{+72.6}_{-45.2}$	-18.4	1.2	...
NB570-S-175068	02:18:28	-05:13:06	3.701	24.8	26.8	5.7	$\lesssim 4$	3.8 ± 1.0	$84.1^{+26.8}_{-21.2}$	-19.1	2.3	...
NB570-S-32766	02:18:35	-05:35:50	3.671	23.0	25.4	$\lesssim 4$	$\lesssim 4$	24.8 ± 1.5	$129.7^{+19.2}_{-8.6}$	-20.7	10.6	...
NB570-S-84321	02:17:45	-05:27:35	3.648	24.4	25.1	7.2	$\lesssim 4$	12.4 ± 4.6	$61.7^{+20.3}_{-22.0}$	-20.9	11.9	...
NB570-S-99194	02:17:14	-05:25:16	3.729	24.9	25.6	...	$\lesssim 4$	11.6 ± 2.7	$94.5^{+23.5}_{-21.6}$	-20.4	7.9	...
NB570-W-53415	02:16:42	-04:58:55	3.667	24.2	25.7	$\lesssim 4$	$\lesssim 4$	8.2 ± 1.5	$66.3^{+11.6}_{-12.0}$	-20.5	8.4	...
NB570-W-55371	02:16:40	-05:01:29	3.699	24.2	24.7	4.7	$\lesssim 4$	5.2 ± 0.8	$19.9^{+3.0}_{-3.3}$	-21.2	17.0	...
$z = 5.7$ LAEs												
NB816-E-127266	02:20:12	-04:49:50	5.681	24.9	> 27.0	$\lesssim 3$...	8.0 ± 1.3	$159.6^{+222.1}_{-73.4}$	-19.2	2.6	...
NB816-E-129103	02:20:13	-04:51:09	5.744	24.8	26.1	$\lesssim 3$...	11.5 ± 1.4	$64.3^{+19.9}_{-14.2}$	-20.5	8.8	...
NB816-E-141288	02:20:21	-04:53:14	5.671	24.8	> 27.0	$\lesssim 3$...	9.6 ± 1.8	$120.6^{+124.3}_{-45.8}$	-19.6	3.9	...
NB816-E-147538	02:20:26	-04:52:34	5.718	23.7	25.1	conf.	conf.	18.9 ± 1.7	$29.2^{+4.2}_{-3.5}$	-21.4	(20.1)	...
NB816-S-36496	02:18:22	-05:33:37	5.650	25.1	26.5	$\lesssim 3$...	13.2 ± 3.4	$133.2^{+92.5}_{-47.1}$	-20.1	6.1	...
NB816-S-39206	02:18:19	-05:33:11	5.676	25.3	> 27.0	4.5	...	5.7 ± 1.5	$135.1^{+300.8}_{-65.8}$	-18.9	2.0	...
NB816-S-41408	02:18:14	-05:32:49	5.673	23.9	25.7	conf.	conf.	17.5 ± 3.0	$42.7^{+12.8}_{-9.5}$	-21.3	(18.5)	...
NB816-S-44568	02:18:17	-05:32:22	5.644	24.6	> 27.0	$\lesssim 3$...	36.0 ± 4.7	$855.6^{+1327.0}_{-402.0}$	-19.0	2.2	...
NB816-S-46148	02:18:23	-05:32:05	5.680	24.9	> 27.0	3.6	...	8.2 ± 1.5	$174.2^{+311.2}_{-84.9}$	-18.9	2.0	...
NB816-S-49611	02:17:43	-05:31:35	5.629	25.0	25.7	$\lesssim 3$	$\lesssim 3$	28.9 ± 14.2	$126.1^{+69.6}_{-50.3}$	-21.1	15.7	...
NB816-S-50308	02:17:48	-05:31:27	5.690	24.0	26.0	3.2	...	15.0 ± 1.2	$81.4^{+27.9}_{-16.3}$	-20.7	10.2	...
NB816-S-59282	02:17:51	-05:30:03	5.712	25.1	26.0	3.8	...	4.8 ± 1.3	$21.3^{+9.5}_{-6.2}$	-20.8	10.8	...

Table 2—Continued

Object Name	$\alpha(\text{J2000})^a$	$\delta(\text{J2000})^a$	z^\ddagger	m_{NB} (mag)	m_{BB} (mag)	S_{NB}^\dagger (kpc)	S_{BB}^\dagger (kpc)	$L(\text{Ly}\alpha)$ (10^{42}erg s^{-1})	EW_0^{app} (\AA)	M_{UV} (mag)	SFR ($M_\odot\text{yr}^{-1}$)	Note
(1)	(2)	(3)	(4)	(5)	(6)	(7)	(8)	(9)	(10)	(11)	(12)	(13)
NB816-S-61269	02:17:45	-05:29:36	5.688	23.7	26.1	3.5	...	21.3 ± 1.7	$93.3^{+32.6}_{-18.8}$	-21.4	19.2	...
NB816-S-66352	02:17:49	-05:28:54	5.696	24.0	25.9	$\lesssim 3$	conf.	16.2 ± 1.1	$79.3^{+22.1}_{-14.2}$	-21.0	(13.4)	...
NB816-S-67673	02:17:45	-05:28:42	5.751	25.0	26.1	3.9	...	10.9 ± 1.4	$61.6^{+21.8}_{-13.1}$	-20.4	7.6	...
NB816-S-70769	02:17:43	-05:28:07	5.685	23.9	26.1	$\lesssim 3$...	17.8 ± 1.2	$122.9^{+41.6}_{-27.6}$	-20.5	8.5	...
NB816-S-77389	02:17:50	-05:27:08	5.693	24.3	> 27.0	6.1	...	11.9 ± 1.9	$106.4^{+107.0}_{-40.3}$	-19.6	3.6	...

Note. — (1): Object name. (2)-(3): RA and Dec. (4): Redshift. (5)-(6): Magnitudes in narrow and broad bands, ($NB503,R$), ($NB570,R$), and ($NB816,z'$), for $z = 3.1, 3.7$, and 5.7 LAEs, respectively. (7)-(8) Half of FWHMs in physical kpc in the narrow and broad bands. We only show reliable FWHMs for sources with a $> 5\sigma$ significance. (9): $\text{Ly}\alpha$ luminosity in $10^{42}\text{ erg s}^{-1}$. (10): Rest-frame *apparent* equivalent width of $\text{Ly}\alpha$ emission line. (11): UV total magnitude defined in Section 5.2. (12): Star-formation rate estimated from the UV total magnitude. The values in parenthesis present formal SFRs which are estimated for AGNs or confused objects. (13): AGN classification and notes.

^aSee the published version for the exact coordinates with decimals.

[‡]In column (4), “:” marks objects with an uncertain spectroscopic identification.

[†]“conf” in the columns (7) and (8) indicates the sources confused by (a) neighboring object(s), which do not give an accurate FWHM.

[¶]The object with a marginal CIV detection, NB503-N-42377. See Section 4.1.

Table 3. Samples of Ly α Emitters

Redshift	Survey Area (arcmin ²)	Magnitude Range [‡] (AB mag)	$L_{Ly\alpha}$ [†] (erg s ⁻¹)	$EW_0^{app\dagger\dagger}$ (Å)	N_{phot}	N_{spec}	Selection Criteria
$z = 3.1 \pm 0.03$	3538	$NB503 = 22.4 - 25.3$	$\gtrsim 1 \times 10^{42}$	$\gtrsim 64$	356	41	eq.(1)
$z = 3.7 \pm 0.03$	3474	$NB570 = 22.7 - 24.7$	$\gtrsim 4 \times 10^{42}$	$\gtrsim 44$	101	26	eq.(2)
$z = 5.7 \pm 0.05$	3722	$NB816 = 23.6 - 26.0$	$\gtrsim 3 \times 10^{42}$	$\gtrsim 27$	401	17	eq.(3)

[‡]2''-diameter aperture magnitudes.

[†]The approximate limit of Ly α luminosity.

^{††}The approximate limit of rest-frame *apparent* equivalent width of Ly α emission. The corresponding *intrinsic* equivalent widths corrected for the IGM absorption are estimated to be $EW_0^{int} = 80, 60, \text{ and } 50\text{Å}$, for $z = 3.1, 3.7, \text{ and } 5.7$ samples, respectively.

Table 4. Ly α Emitters with AGN activities

ID(opt)	RA	Dec	z	Det	ID(X)	sep(X)	$f_{2-10\text{keV}}$	sep(IR)	$f_{24\mu\text{m}}$	$f_{850\mu\text{m}}$	ID(R)	sep(R)	$f_{1.4\text{GHz}}$	$L_{\text{Ly}\alpha}$	M_{UV}	FWHM(NB)	Type
(1)	(J2000) (2)	(J2000) (3)	(4)	(5)	(6)	($''$) (7)	(10^{-15}cgs) (8)	($''$) (9)	(μJy) (10)	(mJy) (11)	(12)	($''$) (13)	(μJy) (14)	(10^{43}erg s^{-1}) (15)	(mag) (16)	(kpc) (17)	(18)
NB503-C-4949702:18:06.826-05:04:08.803.129SPXooo	X0700					2.6	7.1 ± 0.3	...	< 240	$\lesssim 4$	< 60	4.4	-21.67	16.5	BL
NB503-N-3582002:17:35.593-04:42:59.833.102 SPoIoo					< 0.7	0.9	463 ± 48	< 60	2.1	-20.77	13.2	BL?
NB503-N-5538002:17:01.676-04:37:20.24 (3.1) oPoIoR			(3.1)		oPoIoR	...	< 0.6	1.6	378 ± 48	...	VLA0267	1.8	190 ± 20	4.2	-20.64	21.9	...
NB503-N-8047502:17:41.987-04:31:30.553.123 SooloR					< 0.9	1.2	431 ± 48	...	VLA0351	0.7	147 ± 20	3.1	-23.17	7.8	BL
NB570-N-7184202:18:57.776-04:34:31.53 (3.7) oPXooo	X0950		(3.7)		oPXooo	...	4.4 ± 1.4	...	< 240	< 60	3.0	-21.65	8.5	...
NB570-N-3484102:18:31.379-04:43:54.773.724 Sooooo					< 1.3	...	< 240	< 60	14.5	-23.79	< 6.1	BL

Note. — (1): Object name from the optical data. (2)-(3): RA and Dec in the optical data. (4): Redshift. The values in parenthesis are photometric redshifts. (5) The identification of AGN-LAEs in our spectroscopy and multi-wavelength data. “X”, “I”, “M”, or “R” means that the LAE has either an X-ray, infrared, submm, or radio detection. The flags of “S” and “P” indicate a spectroscopically identified AGN and an object satisfying our color-selection criteria of LAEs, respectively. (“o” means no detection or identification in the corresponding condition.) (6) and (12): ID names in the X-ray and radio data presented in Ueda et al. (in preparation) and Simpson et al. (2006a), respectively. (7), (9), and (13): Separation between positions of the optical center and a counterpart of X-ray, infrared, and radio. (8), (10), (11), and (14): Fluxes of X-ray 2-10 keV (in $10^{-15}\text{ erg s}^{-1}\text{ cm}^{-2}$), infrared $24\mu\text{m}$ (in μJy), submm $850\mu\text{m}$ (in mJy), and radio 1.4GHz (in μJy), respectively. For the upper limits of X-ray fluxes, we assume an absorption of neutral hydrogen with a column density of 10^{22} cm^{-2} and a spectral power of $\gamma = 1.8$. We omit the effects of X-ray reflection, which provides the most conservative upper limit in column (8). (15) Ly α luminosity in $10^{43}\text{ erg s}^{-1}$ derived from our photometric data. (16) Total UV magnitude in AB mag. (17) FWHM in the narrow band in physical kpc. (18) Type of object. “BL” indicates an AGN with a broad-line emission ($v_{\text{FWHM}} \gtrsim 1000\text{ km s}^{-1}$) in high ionized lines (i.e. NV, SiIV, CIV, HeII, and/or CIII]). NB503-N-35820 shows a possible broad line with $1321 \pm 362\text{ km s}^{-1}$ in CIV, although the signal-to-noise ratio is as small as 4.

Table 5. Summary of the Ly α luminosity functions.

z	ϕ^* (10^{-4}Mpc^{-3})	$L_{\text{Ly}\alpha}^*$ † (10^{42}erg s^{-1})	α	σ_{EW} (10^2\AA)	χ_r^2	n^{obs} (10^{-4}Mpc^{-3})	$\rho_{\text{Ly}\alpha}^{\text{obs}}$ ($10^{39}\text{erg s}^{-1}\text{Mpc}^{-3}$)	$\rho_{\text{Ly}\alpha}^{\text{tot}}$ ($10^{39}\text{erg s}^{-1}\text{Mpc}^{-3}$)	ϕ_0^* (10^{-4}Mpc^{-3})	$\rho_{0\text{Ly}\alpha}^{\text{tot}}$ ($10^{39}\text{erg s}^{-1}\text{Mpc}^{-3}$)
(1)	(2)	(3)	(4)	(5)	(6)	(7)	(8)	(9)	(10)	(11)
$\alpha = -1.5$ (fix)										
3.1	$9.2^{+2.5}_{-2.1}$	$5.8^{+0.9}_{-0.7}$	-1.5	$1.3^{+0.1}_{-0.1}$	1.57	$15.0^{+3.2}_{-2.8}$	$4.8^{+1.2}_{-1.0}$	$9.4^{+2.0}_{-1.7}$	$10.8^{+3.0}_{-2.5}$	$11.0^{+2.3}_{-2.0}$
3.7	$3.4^{+1.0}_{-0.9}$	$10.2^{+1.8}_{-1.5}$	-1.5	$1.5^{+0.1}_{-0.4}$	0.70	$2.9^{+0.8}_{-0.7}$	$2.4^{+0.7}_{-0.6}$	$6.2^{+1.5}_{-1.3}$	$3.7^{+1.1}_{-1.0}$	$6.7^{+1.6}_{-1.4}$
5.7	$7.7^{+7.4}_{-3.9}$	$6.8^{+3.0}_{-2.1}$	-1.5	2.7(fix)	1.04	$6.8^{+5.2}_{-3.1}$	$3.6^{+3.1}_{-1.7}$	$9.2^{+6.5}_{-3.7}$	$7.7^{+7.5}_{-3.9}$	$9.2^{+6.6}_{-3.7}$
$\alpha = -1.0$ (fix)										
3.1	$14.9^{+4.2}_{-3.2}$	$4.1^{+0.6}_{-0.5}$	-1.0	$1.3^{+0.2}_{-0.1}$	1.72	$13.1^{+2.6}_{-2.1}$	$4.5^{+1.1}_{-0.8}$	$6.1^{+1.3}_{-1.0}$	$17.5^{+5.0}_{-3.7}$	$7.1^{+1.5}_{-1.2}$
3.7	$5.7^{+2.6}_{-1.5}$	$7.2^{+1.3}_{-1.6}$	-1.0	$1.4^{+0.2}_{-0.2}$	0.70	$2.9^{+0.9}_{-0.8}$	$2.4^{+0.9}_{-0.7}$	$4.1^{+1.3}_{-1.0}$	$6.2^{+2.9}_{-1.6}$	$4.5^{+1.4}_{-1.1}$
5.7	$10.4^{+12.0}_{-2.5}$	$5.4^{+0.7}_{-1.7}$	-1.0	2.7(fix)	1.10	$6.3^{+4.0}_{-1.9}$	$3.5^{+2.3}_{-1.2}$	$5.6^{+3.6}_{-1.6}$	$10.5^{+12.1}_{-2.5}$	$5.7^{+3.6}_{-1.6}$
$\alpha = -2.0$ (fix)										
3.1	$3.9^{+1.1}_{-1.5}$	$9.1^{+2.6}_{-1.2}$	-2.0	$1.3^{+0.1}_{-0.1}$	1.51	$18.5^{+6.3}_{-5.1}$	$5.4^{+2.1}_{-1.6}$...	$4.5^{+1.3}_{-1.7}$...
3.7	$1.3^{+0.5}_{-0.3}$	$16.2^{+2.4}_{-2.4}$	-2.0	$1.5^{+0.1}_{-0.3}$	0.71	$2.9^{+0.9}_{-0.6}$	$2.3^{+0.8}_{-0.5}$...	$1.5^{+0.6}_{-0.3}$...
5.7	$3.6^{+3.5}_{-2.5}$	$9.5^{+8.2}_{-3.1}$	-2.0	2.7(fix)	0.97	$6.9^{+8.2}_{-4.0}$	$3.4^{+4.8}_{-2.1}$...	$3.6^{+3.5}_{-2.5}$...

Note. — (1): Redshift. (2)-(4): Best-fit Schechter parameters in units of 10^{-4}Mpc^{-3} and 10^{42}erg s^{-1} for ϕ^* and $L_{\text{Ly}\alpha}^*$, respectively. α is fixed to -1.5 , -1.0 , and -2.0 in 1-3, 4-6, 7-9 lines, respectively. (5): Best-fit σ_{EW} in units of 10^2\AA . For $z = 5.7$ LAEs, we fix $\sigma_{\text{EW}} = 270\text{\AA}$. (6): Reduced χ^2 of the fitting. (7)-(8): Number densities (in 10^{-4}Mpc^{-3}) and Ly α luminosity densities (in $10^{39}\text{erg s}^{-1}\text{Mpc}^{-3}$) calculated with the best-fit Schechter parameters down to the observed limit of Ly α luminosity, i.e. $\log L_{\text{Ly}\alpha} = 42.1, 42.6$, and 42.4 (erg s^{-1}), for $z = 3.1, 3.7, 5.7$, respectively. (9): Inferred total Ly α luminosity densities integrated down to $L_{\text{Ly}\alpha} = 0$ with the best-fit Schechter parameters. (10): Same as (2) but for all LAEs with $EW > 0\text{\AA}$ estimated from the simulations. (11): Same as (9) but for all LAEs with $EW > 0\text{\AA}$ estimated from the simulations.

We refer to the results of $\alpha = -1.5$ as the best estimates of LFs.

$^\dagger L_{\text{Ly}\alpha}^*$ is the apparent value, i.e. observed Ly α luminosity with no correction for IGM absorption. If we assume the simple IGM absorption model in Section 5.1.2, the apparent $L_{\text{Ly}\alpha}^*$ is divided by a factor of (0.81, 0.73, 0.54) to obtain the intrinsic $L_{\text{Ly}\alpha}^*$ at $z = (3.1, 3.7, 5.7)$. For examples, in the case of $\alpha = -1.5$, the intrinsic $L_{\text{Ly}\alpha}^*$ is estimated to be $(7.1^{+1.0}_{-0.9}, 14.1^{+2.5}_{-2.1}, 12.6^{+5.6}_{-3.9}) \times 10^{42}\text{erg s}^{-1}$ at $z = (3.1, 3.7, 5.7)$.

Table 6. Summary of the UV luminosity functions.

z	ϕ^* (10^{-4}Mpc^{-3})	M_{1500}^* (mag)	α	χ_r^2	Mag. Range (mag)	n^{obs} (10^{-4}Mpc^{-3})	$\rho_{\text{UV}}^{\text{obs}}$ ($10^{25}\text{erg s}^{-1}\text{Hz}^{-1}\text{Mpc}^{-3}$)	$\rho_{\text{UV}}^{\text{tot}}$ ($10^{25}\text{erg s}^{-1}\text{Hz}^{-1}\text{Mpc}^{-3}$)
(1)	(2)	(3)	(4)	(5)	(6)	(7)	(8)	(9)
3.1	$5.6^{+6.7}_{-3.1}$	-19.8 ± 0.4	-1.6	0.43	$-21.9 < M < -18.9$	$4.0^{+4.7}_{-2.2}$	$1.2^{+1.4}_{-0.7}$	$4.4^{+5.2}_{-2.4}$
3.7	$5.2^{+0.8}_{-0.7}$	$-19.8(\text{fix})^\dagger$	-1.6	2.74	$-21.7 < M < -19.7$	$1.0^{+0.1}_{-0.1}$	$0.5^{+0.1}_{-0.1}$	$4.1^{+0.6}_{-0.5}$
5.7	$4.4^{+11.9}_{-3.2}$	-20.6 ± 0.6	-1.6	0.29	$-22.1 < M < -20.6$	$0.8^{+2.1}_{-0.6}$	$0.9^{+2.5}_{-0.7}$	$7.5^{+20.4}_{-5.5}$

Note. — (1): Redshift. (2)-(4): Best-fit Schechter parameters in units of 10^{-4}Mpc^{-3} and AB magnitude for ϕ^* and M_{1500}^* . α is fixed to -1.6 . (5): Reduced χ^2 of the fitting. (6): Magnitude range of UV LFs that are used for the fitting. (7)-(8): Number densities (in 10^{-4}Mpc^{-3}) and UV luminosity densities (in $10^{25}\text{erg s}^{-1}\text{Hz}^{-1}\text{Mpc}^{-3}$) calculated with the best-fit Schechter parameters down to the observed limit of UV luminosity, i.e. $M_{1500} = -18.9, -19.7, \text{ and } -20.6$, for $z = 3.1, 3.7, 5.7$, respectively. (9): Inferred total UV luminosity densities integrated down to $M_{1500} = \infty$ with the best-fit Schechter parameters.

† For the $z = 3.7$ LF, we fix M_{1500}^* to -19.8 that is the best estimate of our $z = 3.1$ LF.

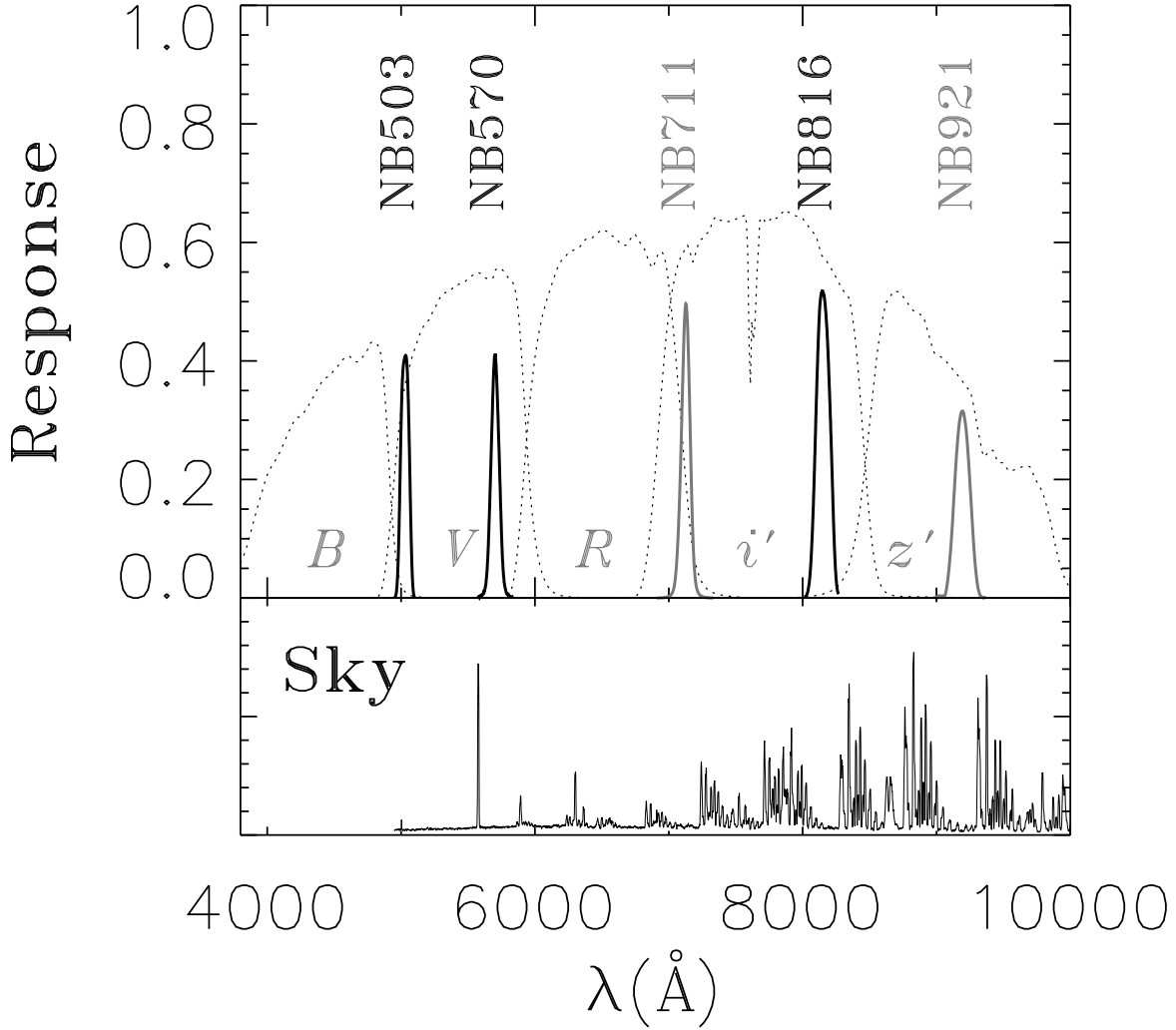


Fig. 1.— *Top panel* : Response of the narrow-band filters, NB503, NB570, and NB816 (black solid lines), of this work, together with that of broad-band filters of B, V, R, i' , and z' (dotted lines) and two other narrow-band filters of $NB711$ (Ouchi et al. 2003; Shimasaku et al. 2003) and $NB921$ (gray solid lines). $NB921$ filter is used for our on-going observations in the SXDS field. These response curves include atmospheric absorption, quantum efficiency, and transmittance of optical elements of the telescope and instrument. *Bottom panel* : The spectrum of night-sky emission. Note that the passbands of the narrow-bands do not include a strong sky emission.

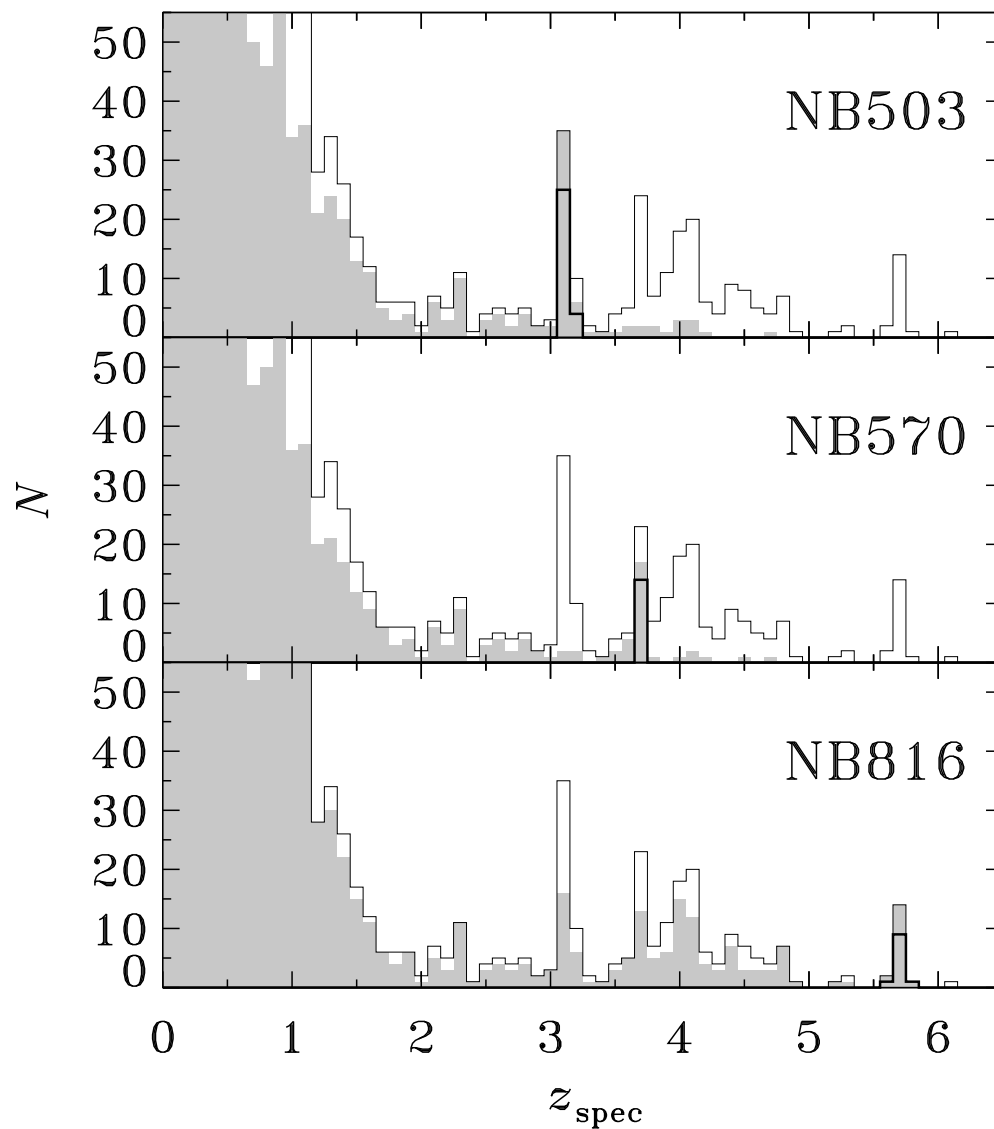


Fig. 2.— Redshift distribution of our objects with a spectrum. Thin solid lines in all three panels show the distribution of our LAEs and objects of the SXDS spectroscopic catalog. The shaded histograms indicate the sources detected at a 5σ level with *NB503* (top), *NB570* (middle), and *NB816* (bottom). The thick solid lines in top, middle, and bottom panels represent our spectroscopic LAEs that meet the color criteria of equations (1), (2), and (3), respectively.

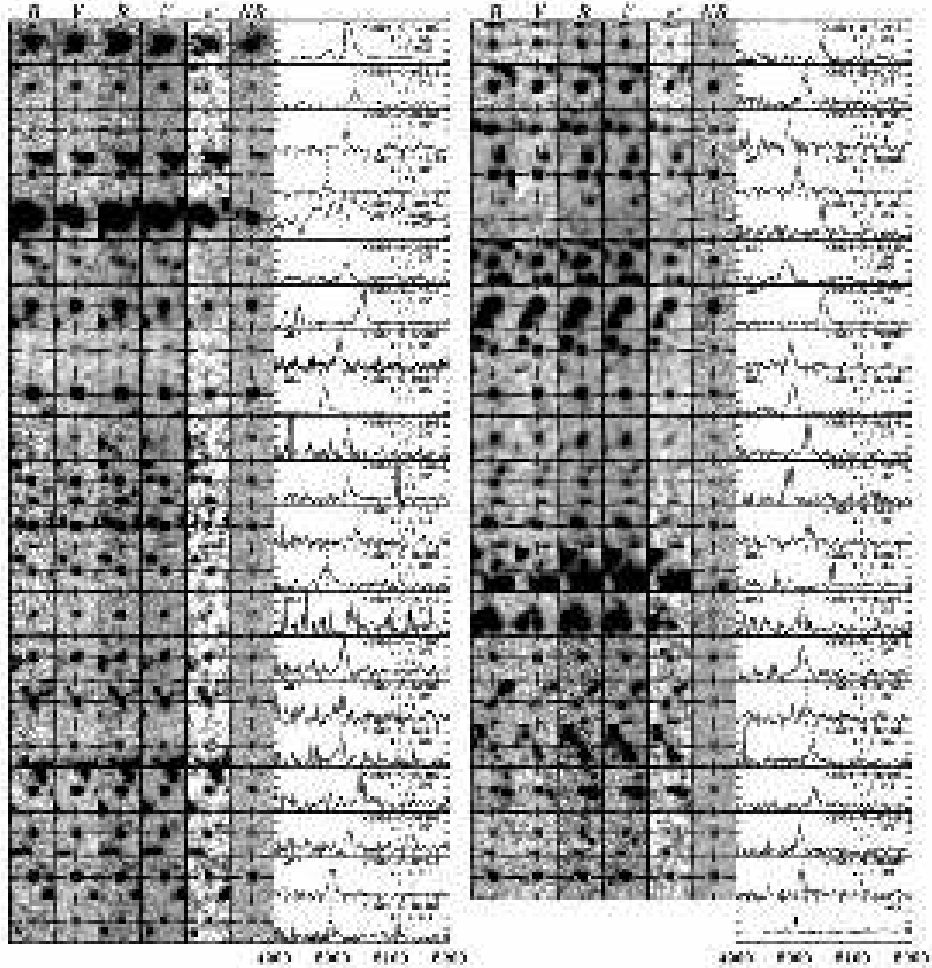


Fig. 3.— Spectra and snapshots of our $z = 3.1$ LAEs. Each object has a spectrum in right and snapshots of B , V , R , i' , z' , and $NB503$ images in left. Each snapshot is presented in a $6'' \times 6''$ box. In the panel of spectrum, the tick of y axis is marked in 2.5×10^{-18} erg s^{-1} cm^{-2} \AA^{-1} ; for panels in which a factor is shown in the upper left corner, multiply the scale by this factor to obtain a correct scale. The wavelength (in x axis) is in unit of \AA . The object name and redshift (+AGN classification, if any) are presented in the right corner of each spectrum panel. 'P' ('N') in parentheses indicates that the object is (or is not) selected with the color criteria and included in our photometric sample (Section 3.1). The vertical dotted lines mean the center of the emission line. The right bottom panel shows a typical spectrum of the sky background with an arbitrary normalization.

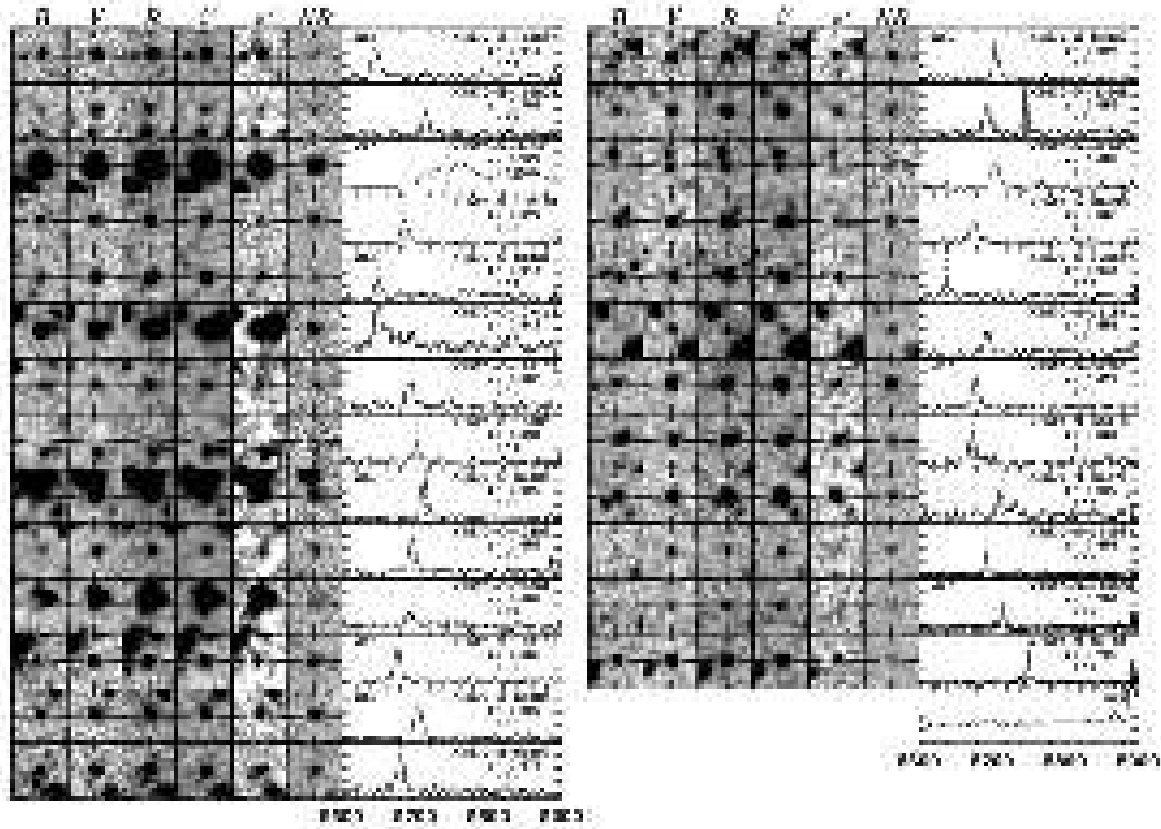


Fig. 4.— Same as Figure 3, but for our $z = 3.7$ LAEs.

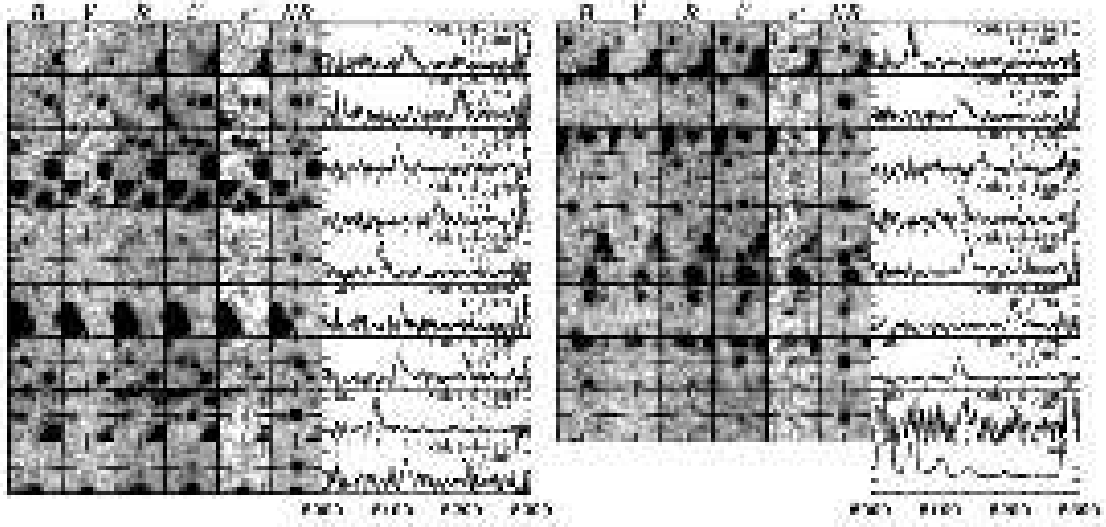


Fig. 5.— Same as Figure 3, but for our $z = 5.7$ LAEs. The ticks of y axis in a spectrum panel are marked in $0.5 \times 10^{-18} \text{ erg s}^{-1} \text{ cm}^{-2} \text{ \AA}^{-1}$.

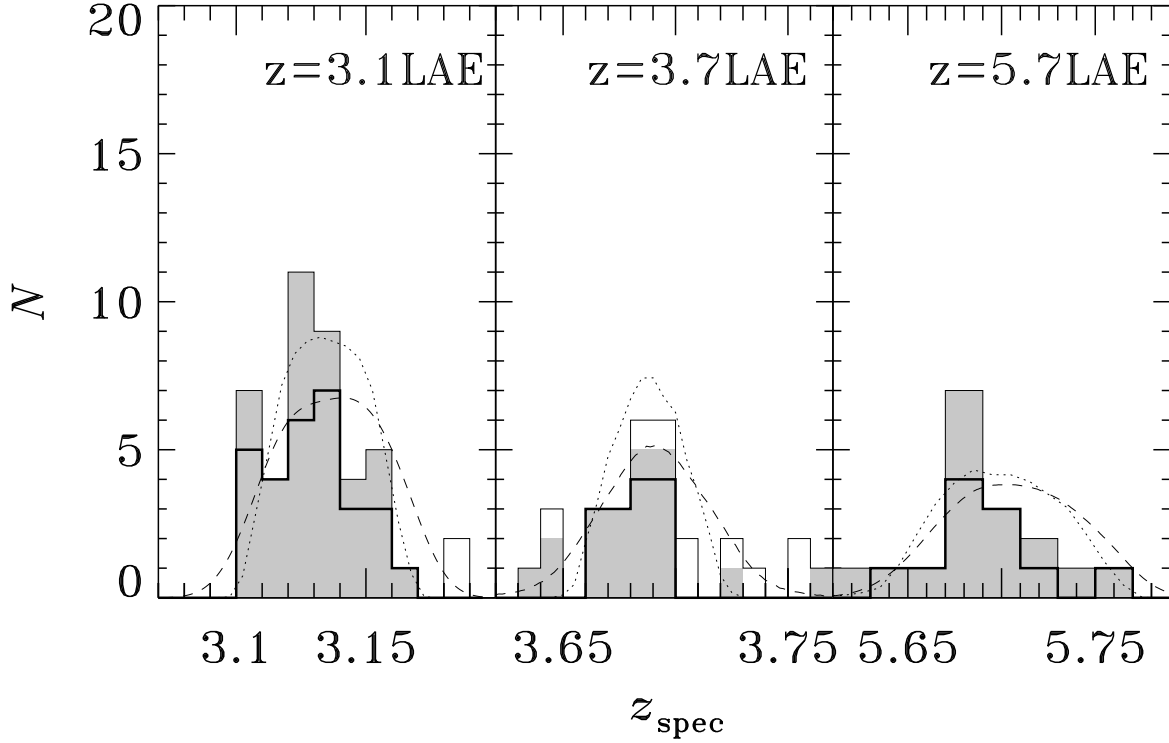


Fig. 6.— The redshift distribution of spectroscopically identified LAEs at $z = 3.1$ (left), 3.7(middle), and 5.7 (right). Thin solid lines indicate all the spectroscopically identified objects. The shaded histograms present the sources at the 5σ level in *NB503* (left), *NB570* (middle), and *NB816* (right) bands. The thick solid lines are histograms for LAEs selected by the color criteria of equations (1) (left), (2) (middle), and (3) (right). The dashed lines represent selection functions of LAEs that are simply calculated from the response curves of narrow-band filters. The dotted lines are selection functions from the results of our simulations in Section 5.1. Both of the selection functions are normalized by the numbers of identified LAEs.

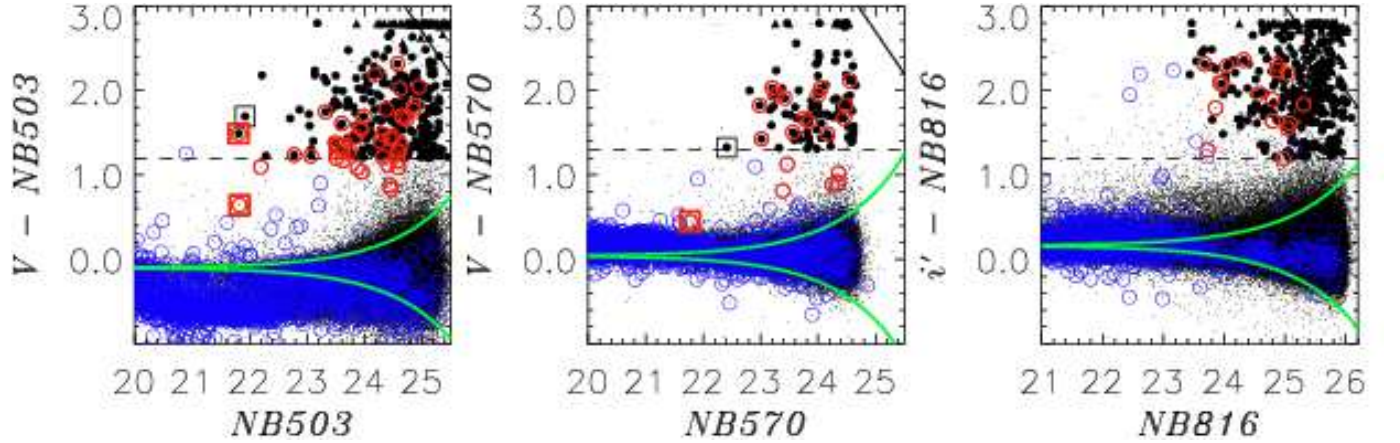


Fig. 7.— Color magnitude diagrams of *NB503* (left), *NB570* (middle), and *NB816* (right). The black dots plot colors of all the detected objects. The photometrically-selected LAEs are presented with filled circles and triangles. The LAEs of triangles have a broad-band (V or i') magnitude fainter than that of the 2σ level, and show the lower limits of the narrow-band excess color. The red and blue open circles denote spectroscopically-identified objects in the redshift range of LAEs and interlopers, respectively. We define the redshift ranges of LAEs as $z = 3.09 - 3.18$, $3.63 - 3.75$, and $5.60 - 5.78$ in the diagrams of *NB503*, *NB570*, and *NB816*, respectively (see Figure 6 for these redshift ranges). The red and black squares mark AGNs from our multi-wavelength data (Table 4) with and without a spectroscopic redshift, respectively. For a display purpose, we place symbols at the narrow- v.s. broad-band color of 2.8 for objects with a color redder than 2.8. The green lines indicate 3σ errors of the colors of narrow v.s. broad bands for a source with a color of $V - NB503 = -0.10$, $V - NB570 = 0.04$, and $i' - NB816 = 0.16$, which correspond to the average color of all objects. The solid and dashed lines represent the 2σ limit of a broad band, and the color cut of narrow-band excess. Note that the narrow-band magnitudes, i.e. *NB503*, *NB570*, and *NB816*, are total magnitudes, while the colors of $V - NB503$, $V - NB570$, and $i' - NB816$ are defined with a $2''$ -diameter aperture.

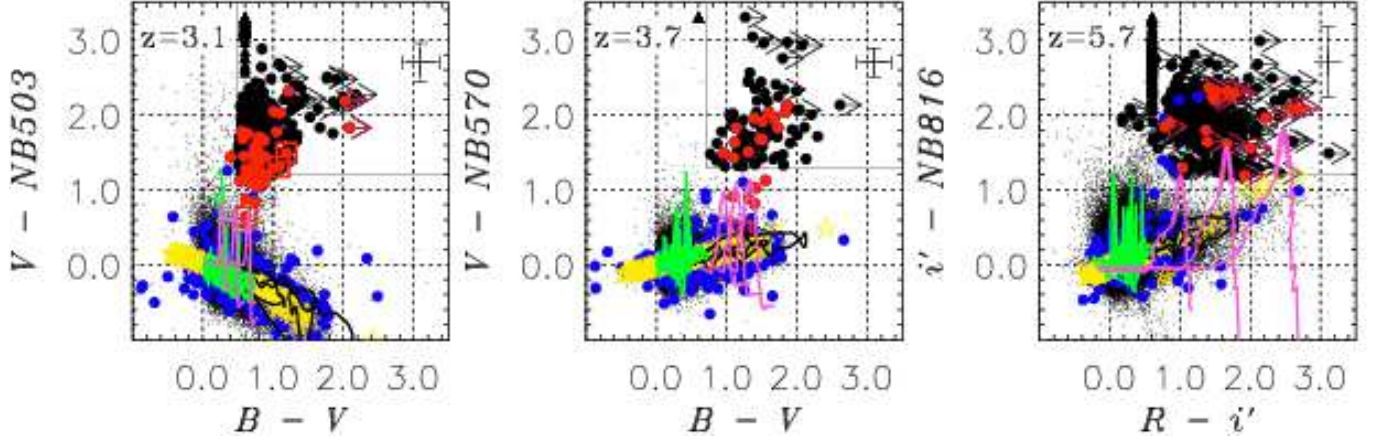


Fig. 8.— Two color diagrams of continuum and narrow-band excess. *Left panel:* The diagram of $B - V$ v.s. $V - NB503$ for our $z = 3.1$ LAEs. The black dots present colors of all the detected objects. The photometrically selected LAEs are plotted with filled circles and triangles. The LAEs of triangles have an off-band (V) magnitude fainter than 2σ level, and show the lower limits of $V - NB503$. The red and blue circles/triangles indicate spectroscopically identified objects in and out of the LAE redshift range, respectively. We take the LAE redshift range same as that of Figure 7. The red squares mark spectroscopically identified AGNs found in our multi-wavelength data (Table 4). For a display purpose, we place symbols at $V - NB503 = 3.3$ for the objects with a color of $V - NB503 > 3.3$. The objects with no continuum (V -band) detection below a 2σ level are plotted at a color of $B - V = 0.6$. The error bars at the upper-right corner indicate 1σ errors for a typical LAE whose brightness is the median magnitudes of our photometrically selected LAEs. The solid line shows the color criteria of eq. (1) for sources with a detection in the broad band (V). The colors are defined with a $2''$ -diameter aperture. The curves present tracks of model galaxies at different redshifts. Pink lines indicate model-LAE SEDs which are composite spectra of a 0.03 Gyr single burst model galaxy Bruzual & Charlot 2003 and a Lyman α emission ($EW_{\text{rest}}(\text{Ly}\alpha) = 22 \text{ \AA}$); from the left to right, three different amplitudes of IGM absorption are applied: $0.5\tau_{\text{eff}}$, τ_{eff} , and $1.5\tau_{\text{eff}}$, where τ_{eff} is the Madau’s (1995) original median opacity. The narrow-band excess in each of the peaks in the red lines indicates the Lyman α emission of LAEs at $z = 3.1$. Green lines show 6 templates of nearby starburst galaxies (Kinney et al. 1996) up to $z = 2$, which are 6 classes of starburst galaxies with different dust extinction ($E(B - V) = 0.0 - 0.7$). The narrow-band excess peaks in the green line correspond to the emission lines of [OIII] ($z = 0.004$), $\text{H}\beta$ ($z = 0.03$), or [OII] ($z = 0.3$). Black lines show colors of typical elliptical, spiral, and irregular galaxies (Coleman, Wu, & Weedman 1980) which are redshifted from $z = 0$ to $z = 2$. Yellow star marks show 175 Galactic stars given by Gunn & Stryker (1983). *Middle panel:* Same as the left panel but for $z = 3.7$ LAEs. *Right panel:* Same as the left panel but for $z = 5.7$ LAEs. We do not show the error bar of a $R - i'$ color at the upper-right corner, because a typical LAE has no R -band flux above a 1σ noise level.

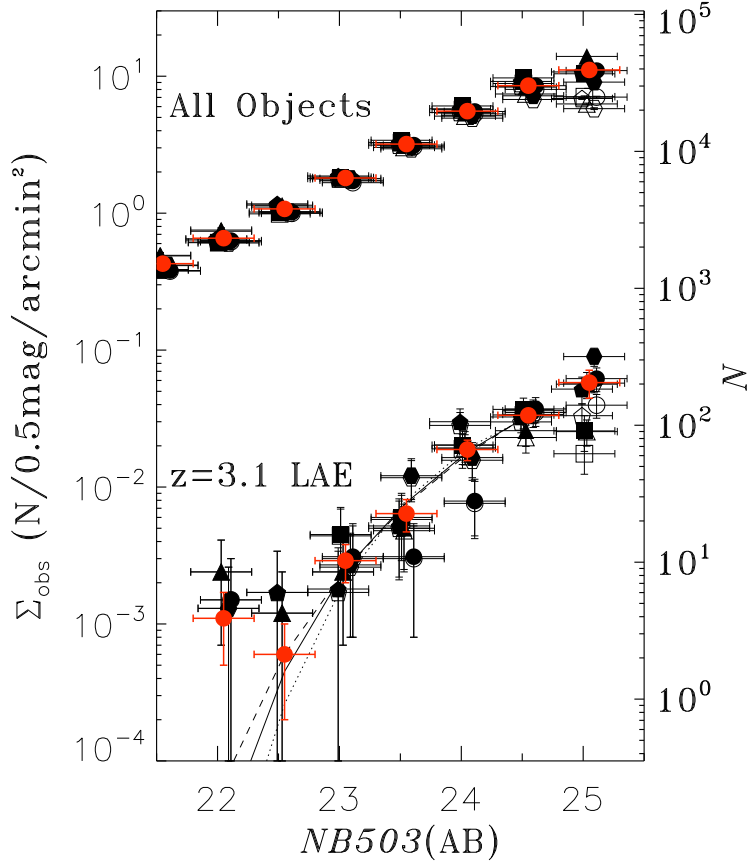


Fig. 9.— Surface densities of objects detected in the *NB503* data. The lower and upper points indicate surface densities of our $z = 3.1$ LAEs and all the objects detected in the narrow band, respectively. Black circles, hexagons, triangles, squares, and pentagons plot the surface densities of a ~ 0.2 deg field, SXDS-C, SXDS-N, SXDS-S, SXDS-E, and SXDS-W, respectively. We distinguish between the raw and completeness-corrected surface densities with the open and filled symbols, respectively. The red filled circles represent the surface density averaged over our $\simeq 1$ deg² survey field. The errors are given by Poisson statistics for black symbols, while the errors of red symbols are made by the geometric mean of Poisson errors and field-to-field variation of eq. (4). For the presentation purpose, we slightly shift all the black points along the abscissa. The exact magnitude of a black point is the same as a magnitude of neighboring red point. The vertical axis on the right side indicates the numbers of objects, i.e. $N/(0.5\text{mag})$, identified in our $\simeq 1$ deg² survey area. The solid, dotted, and dashed lines present the surface densities of LAEs reproduced by our simulations for the cases of $\alpha = -1.5$, -1.0 , and -2.0 , respectively (see Section 5.1 for more details).

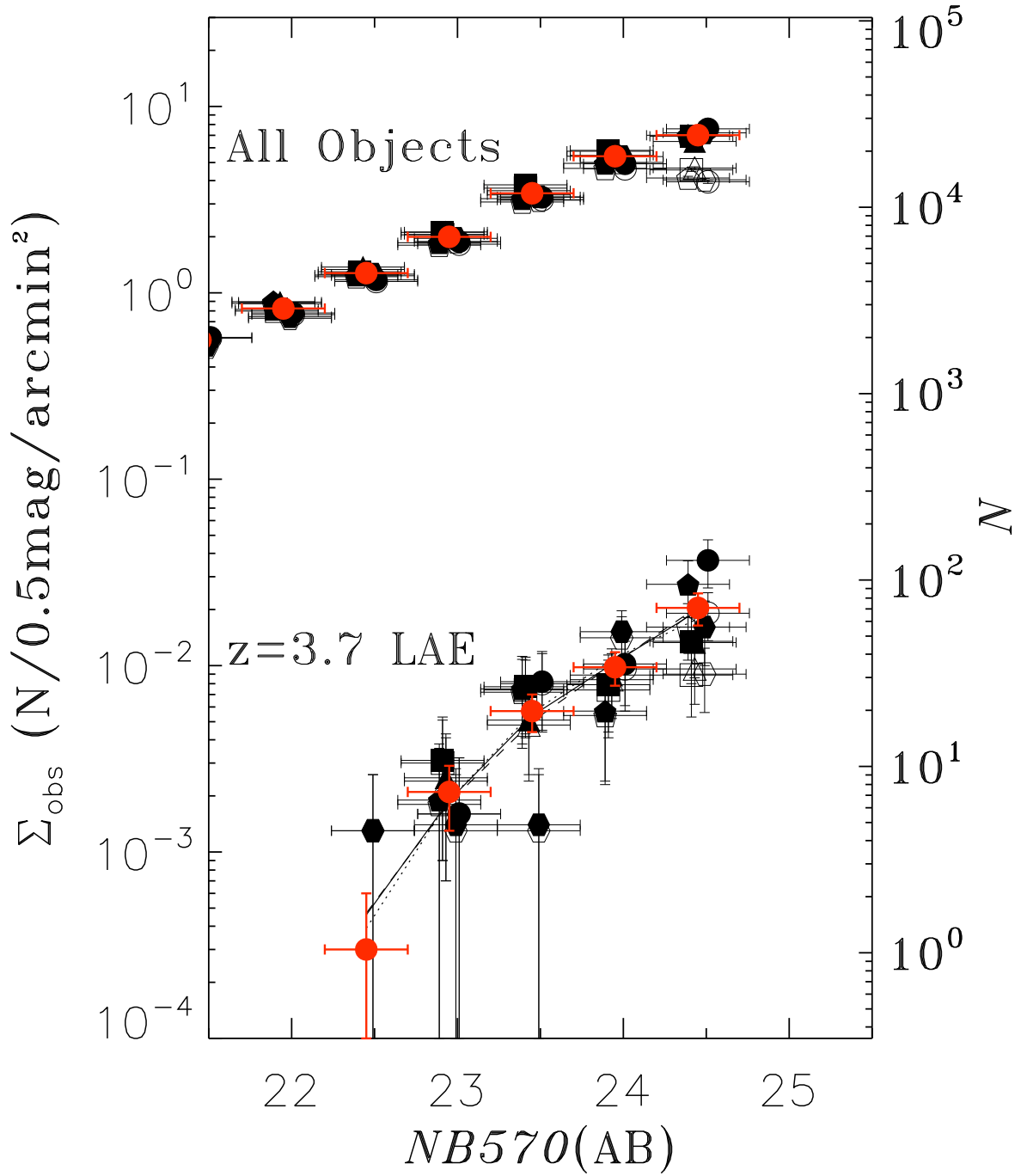


Fig. 10.— Same as Figure 9, but for $NB570$ data.

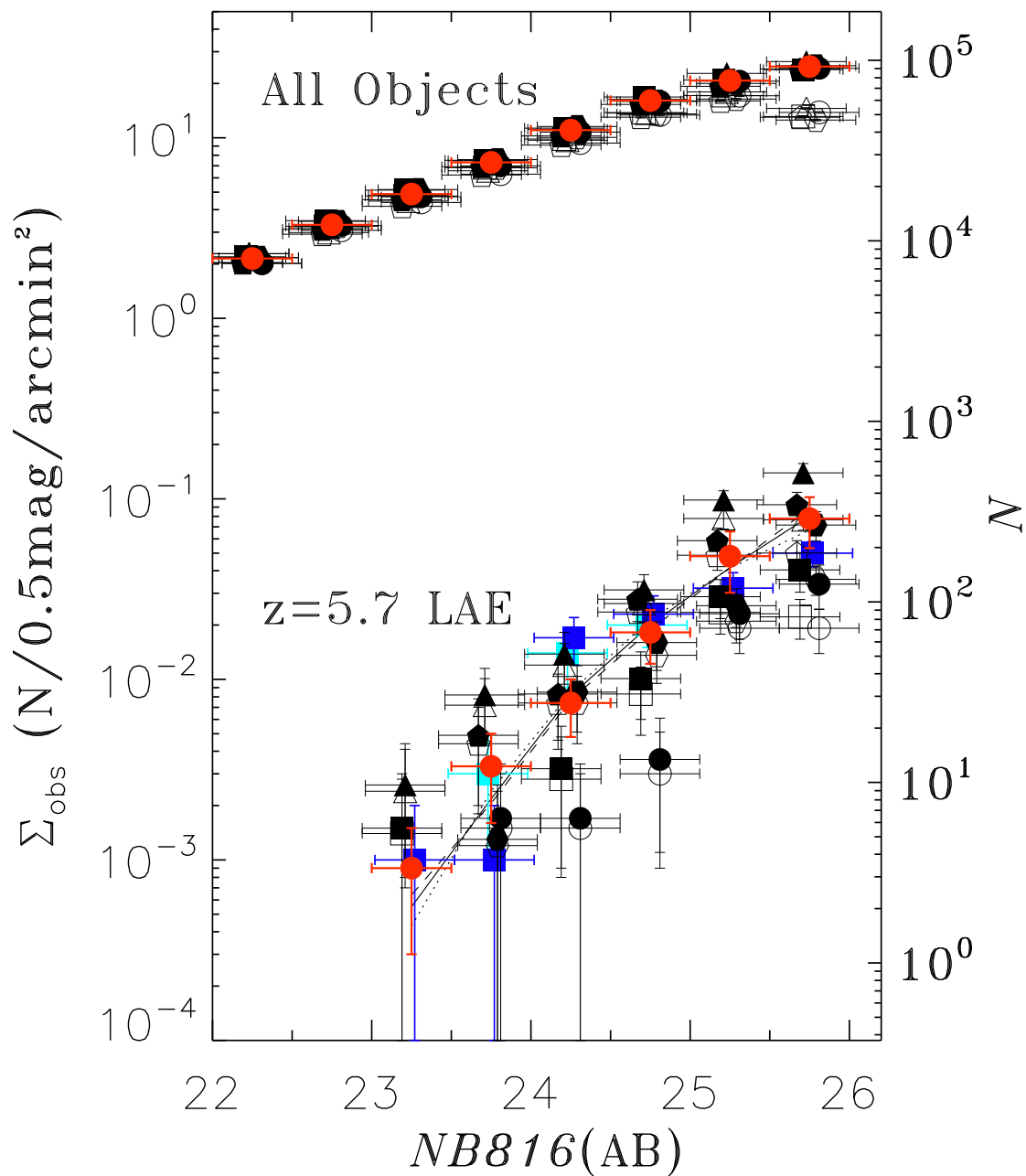


Fig. 11.— Same as Figure 9, but for *NB816* data. The blue and cyan squares are the surface densities of $z = 5.7$ LAEs detected with the same *NB816* filter but in different sky areas by Shimasaku et al. (2006) and Hu et al. (2004), respectively.

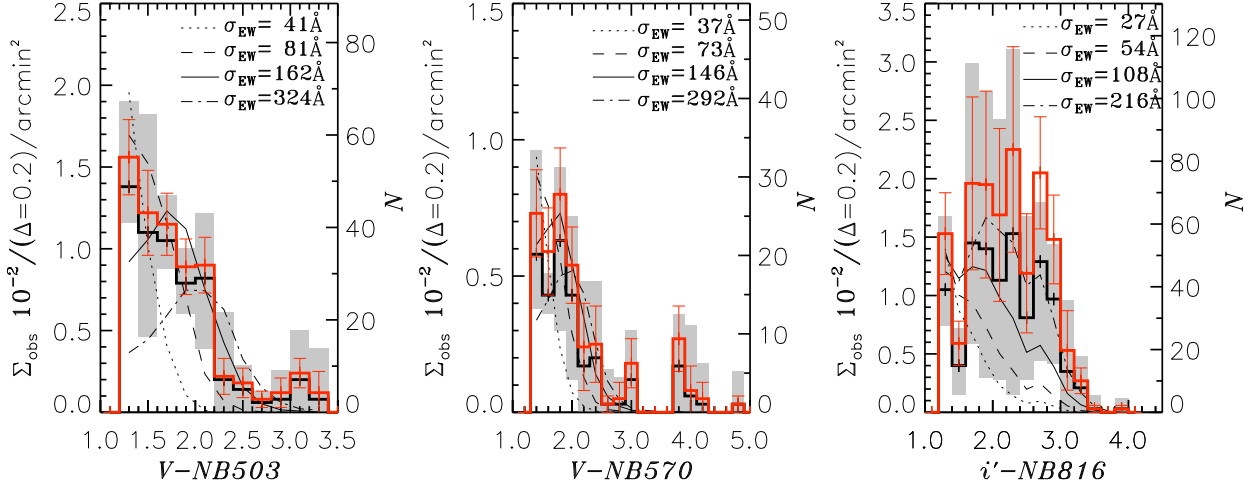


Fig. 12.— Color histograms of $V - NB503$ (left), $V - NB570$ (middle) and $i' - NB816$ (right) for the photometric sample of $z = 3.1$, 3.7 , and 5.7 LAEs, respectively. The black-solid histogram presents the average of all the LAEs in the $\simeq 1 \text{ deg}^2$ field. The shaded region shows the variations of histograms of five $\sim 0.2 \text{ deg}$ fields, SXDS-C, SXDS-N, SXDS-S, SXDS-E, and SXDS-W. The red histogram is the same as the black-solid histogram, but with a completeness correction. The error bars of the red histogram are given by the geometric mean of Poisson errors and field-to-field variation of eq. (4). The right-hand vertical axis on each panel indicates the numbers of LAEs for the $\simeq 1 \text{ deg}^2$ histogram. We plot color distribution reproduced by our simulations of fixed $\alpha = -1.5$ with dotted, dashed, solid, and dot-dashed lines, whose σ_{EW} values are presented in the legends.

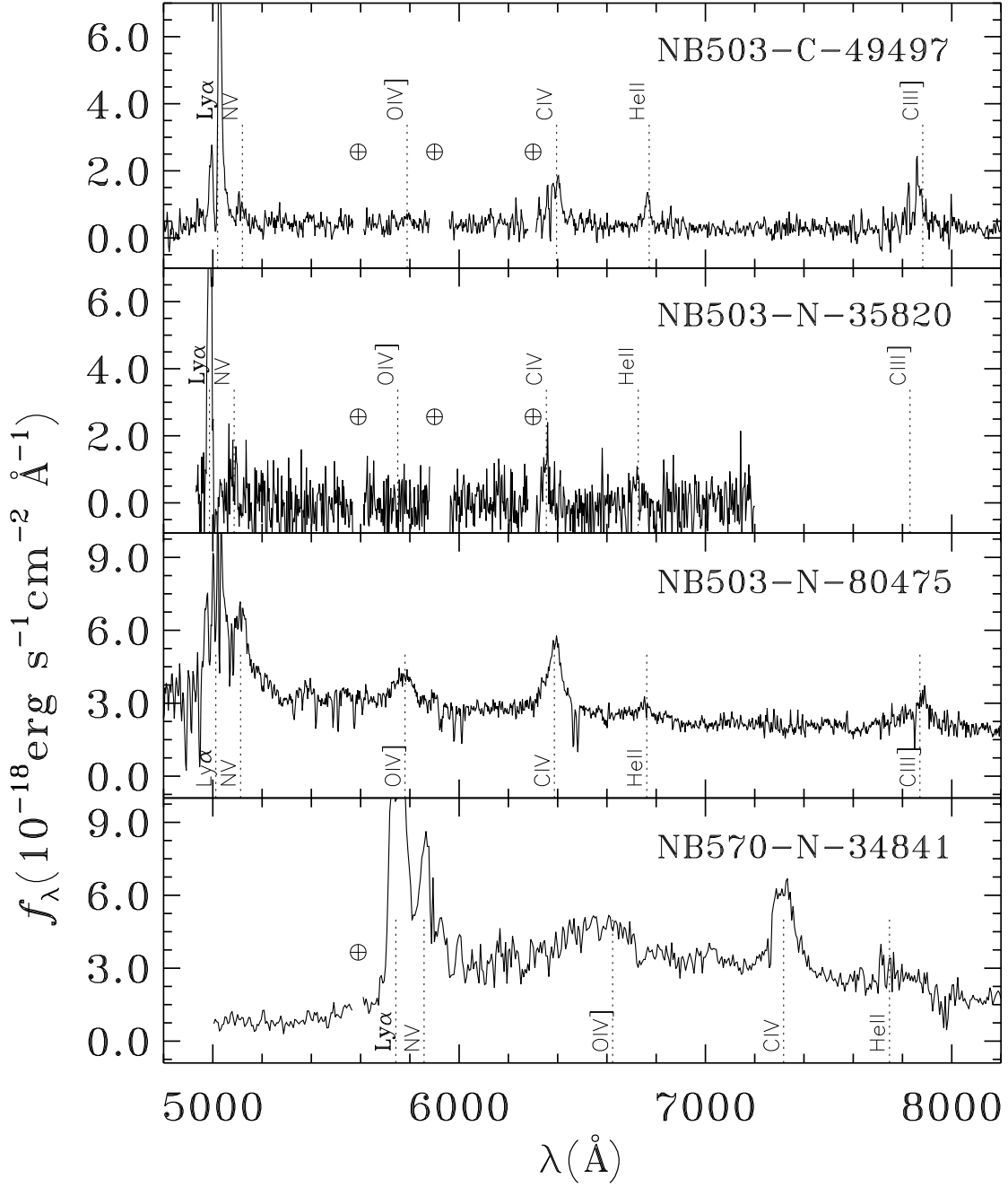


Fig. 13.— Spectra of LAEs with AGN activities. We show four AGN-LAEs that have spectroscopic data (see Table 4). Dotted lines with the legend indicate wavelengths of a typical emission from AGN. “ \oplus ” marks the wavelengths where significant residuals of sky subtraction remain due to strong OH sky lines on a faint continuum.

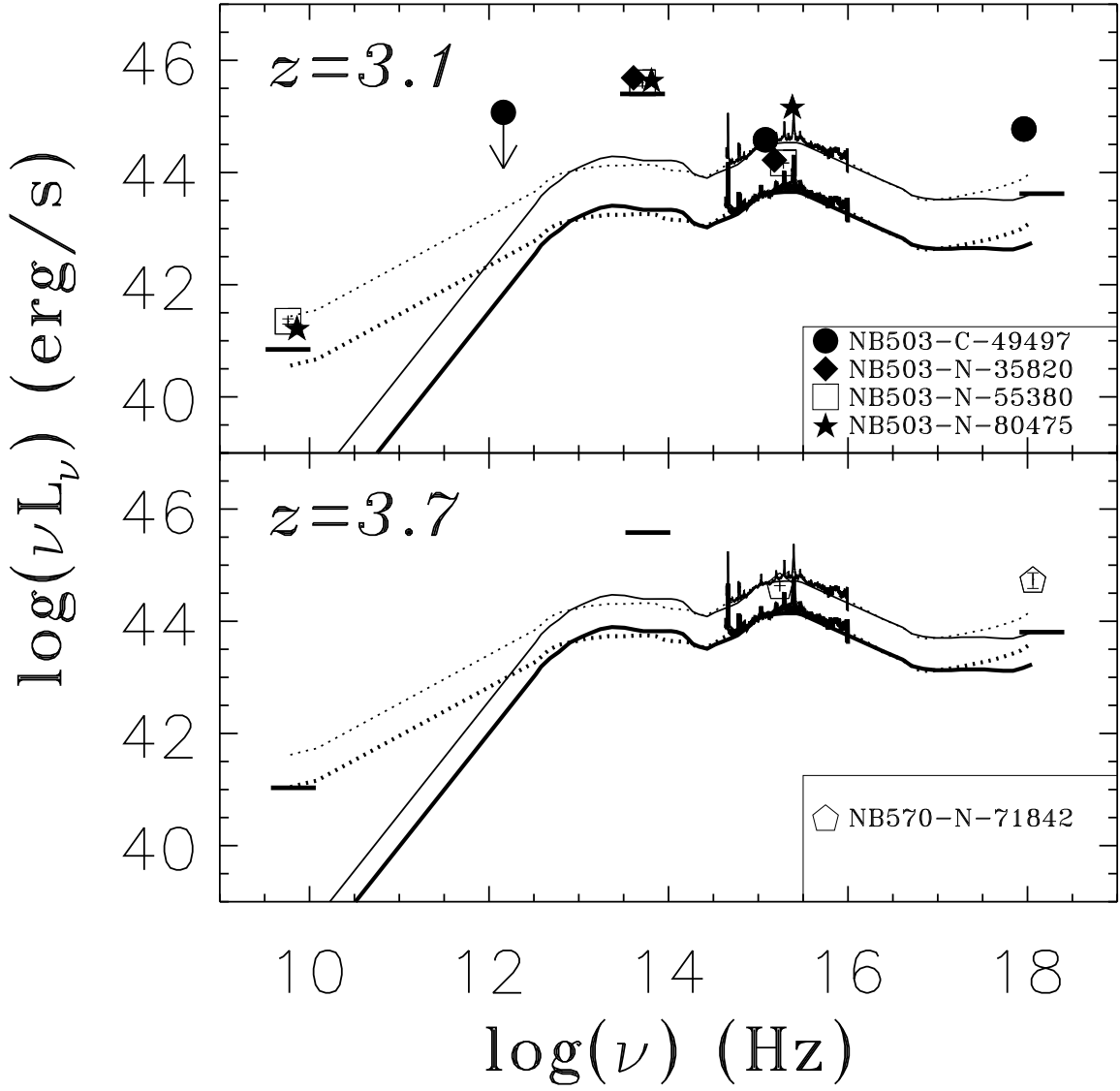


Fig. 14.— The spectral energy distribution (SED) of LAEs with (an) X-ray, infrared, and/or radio counterpart(s). The legend shows object names and the corresponding symbols. Filled and open symbols represent an object with and without a spectroscopic identification, respectively. Solid and dotted curves are the templates of radio-quiet and radio-loud AGNs taken from Elvis et al. (1994); Telfer et al. (2002); Richards et al. (2003) (see text). The thick and thin curves indicate the template SEDs normalized with the detection limits of Ly α and X-ray, respectively. The horizontal solid bars present our detection limits in X-ray, infrared, and radio bands.

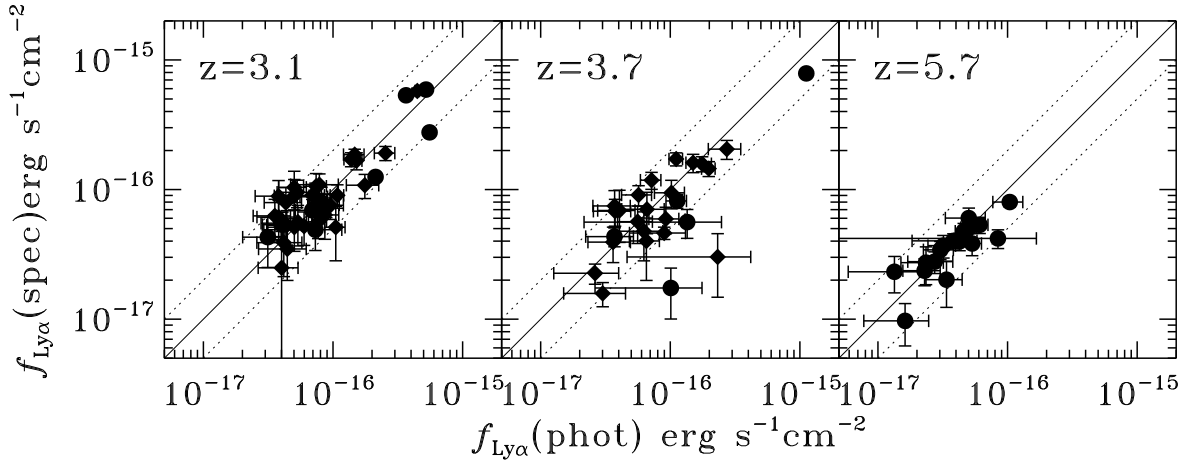


Fig. 15.— Comparison of Ly α fluxes measured with our images, $f_{\text{Ly}\alpha}(\text{phot})$, and spectra, $f_{\text{Ly}\alpha}(\text{spec})$, for our LAEs at $z = 3.1$ (left), 3.7 (middle), and 5.7 (right). The circles and diamonds indicate LAEs with FOCAS and VIMOS spectra, respectively. Since our FOCAS observations used a relatively narrow slit, we apply slit-loss corrections for the Ly α fluxes of FOCAS. The error bars of circles and diamonds show the ranges of a 95% confidence level. The solid line at each panel presents the equality of $f_{\text{Ly}\alpha}(\text{phot})$ and $f_{\text{Ly}\alpha}(\text{spec})$. We plot dotted lines for the differences from the equality by a factor of 2.

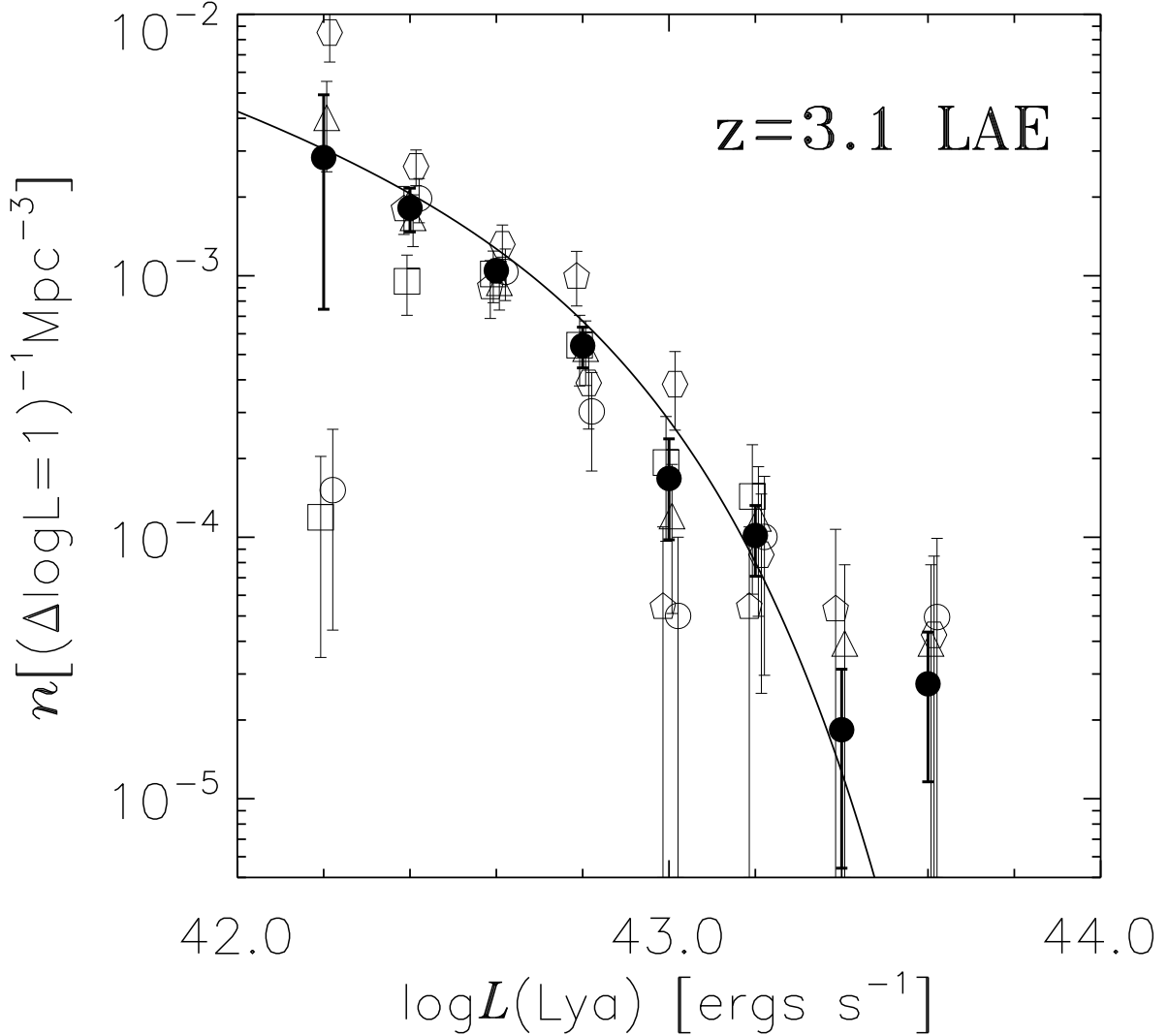


Fig. 16.— Luminosity functions (LFs) of LAEs at $z = 3.1$. The filled circles are LFs obtained by the classical method. The error bars include the field-to-field variation (see eq. 4). The open circles, hexagons, triangles, squares, and pentagons represent the LFs of five ~ 0.2 deg fields, SXDS-C, SXDS-N, SXDS-S, SXDS-E, and SXDS-W, respectively, which are also derived by the classical method. In order to avoid the overlaps of points, we slightly shift all the open symbols along the abscissa. The exact luminosity of an open symbol is the same as a magnitude of a neighboring filled circle. The solid line is the best-fit Schechter function with $\alpha = -1.5$ estimated by our simulations, but not the Schechter function fitted to the LFs of the classical method.

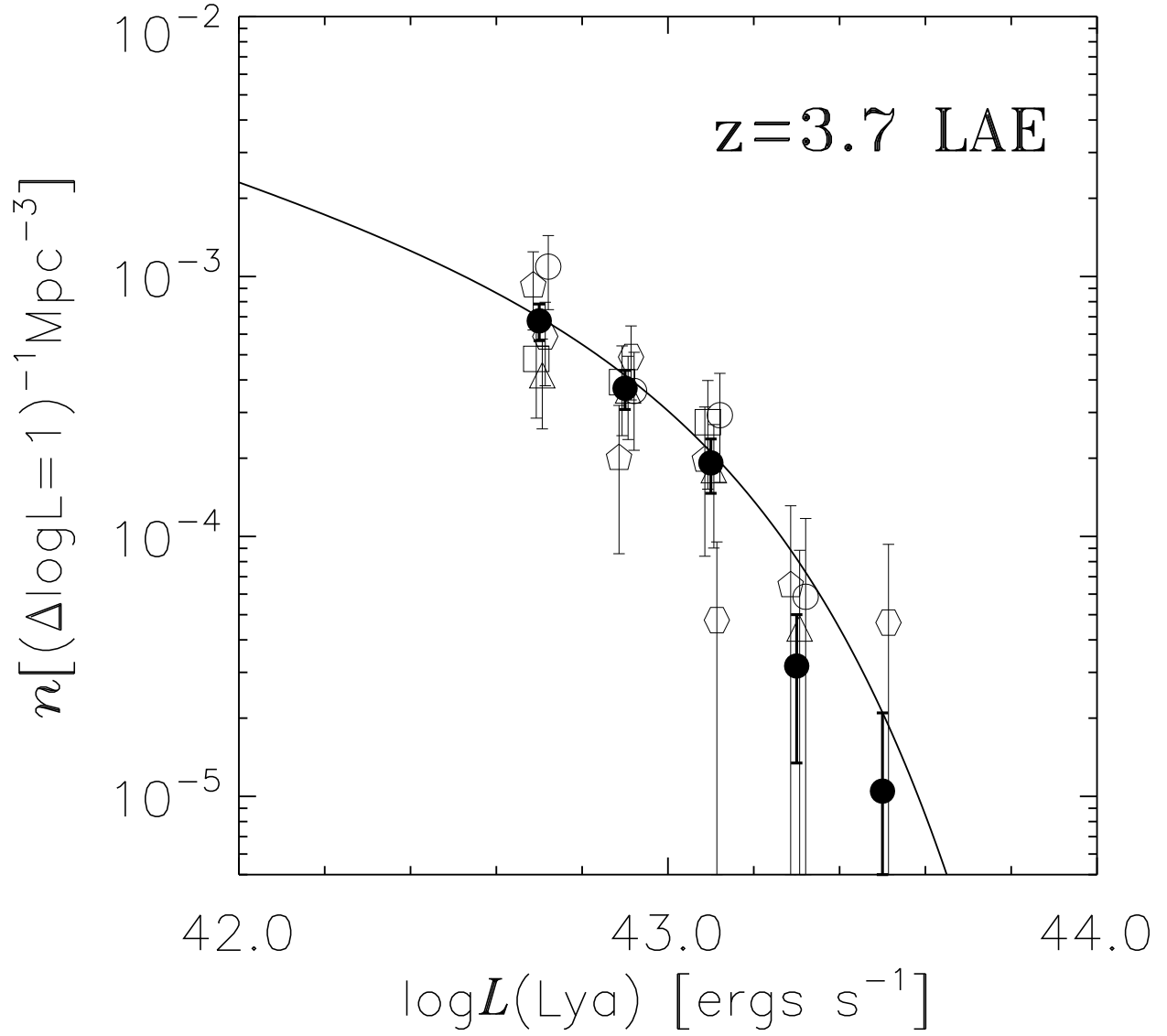


Fig. 17.— Same as Figure 16, but for $z = 3.7$.

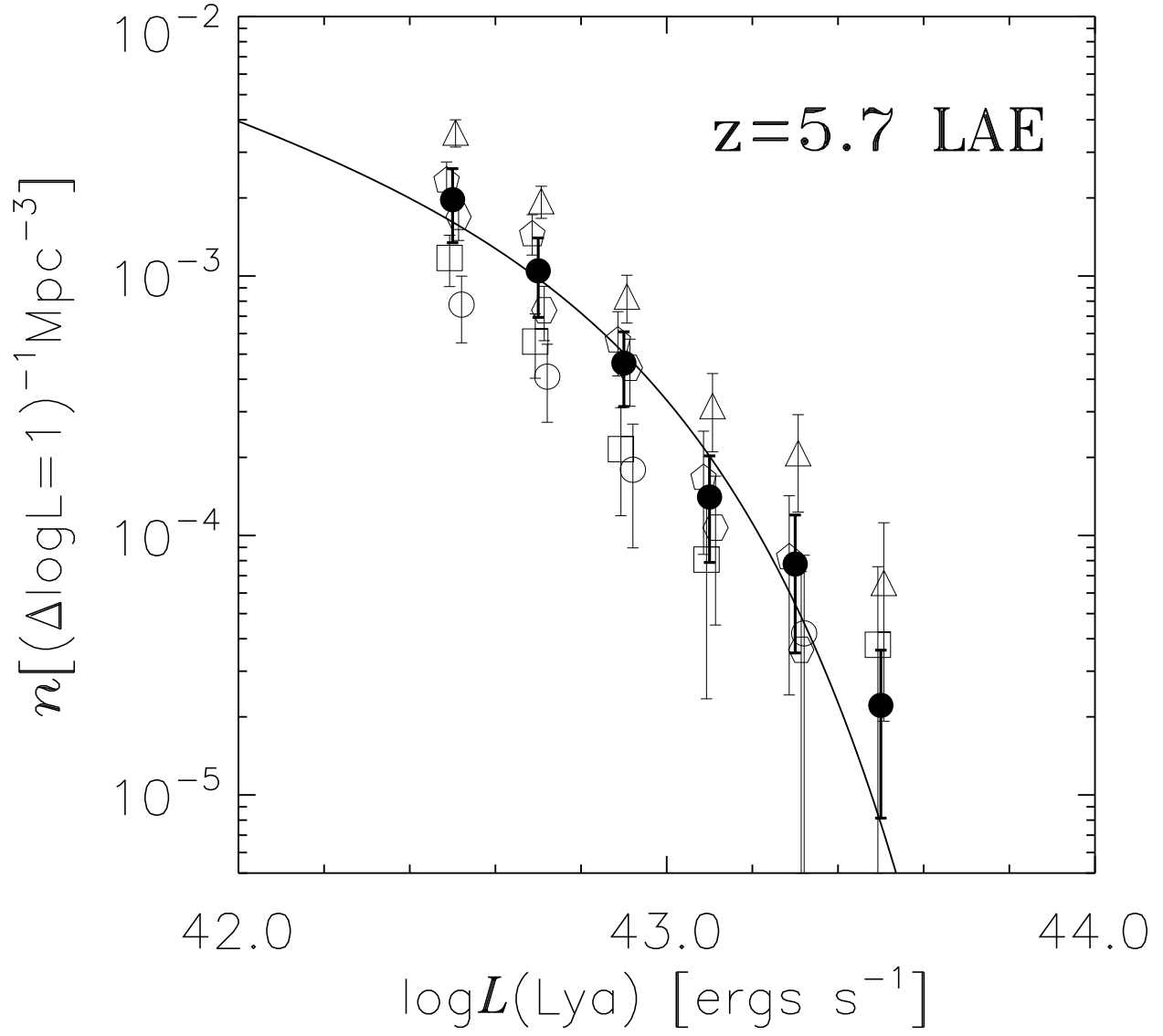


Fig. 18.— Same as Figure 16, but for $z = 5.7$.

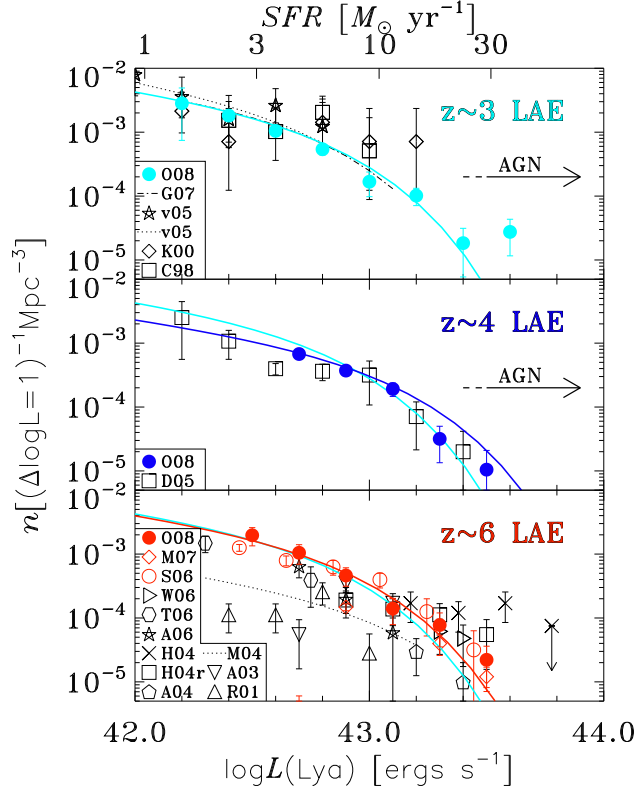


Fig. 19.— The best measurements of Ly α luminosity functions (LFs) at $z \sim 3$ (top), 4 (middle), and 6 (bottom), together with the previous measurements. The cyan, blue, and red filled circles are the LFs calculated with the classical method at $z = 3.1$, 3.7, and 5.7, respectively, that are labeled as O08 in the legend. The corresponding best-fit LFs from the simulations are plotted with colored solid lines. These filled circles and solid lines are the same as those presented in Figures 16-18. Note that the $z = 3.1$ LFs (cyan lines) are overplotted on the middle and bottom panels for references. The other symbols and dotted-lines are the previous measurements and best-fit Schechter functions whose references are indicated in the legend on each panel: *G07*—Gronwall et al. (2007), *v05*—van Breukelen et al. (2005), *K00*—Kudritzki et al. (2000), *C98*—Cowie & Hu (1998), *D05*—Dawson (2005), *M07*—Murayama et al. (2007), *S06*—Shimasaku et al. (2006), *W06*—Westra et al. (2006), *T06*—Tapken et al. (2006), *A06*—Ajiki et al. (2006), *H04*—Hu et al. (2004), *H04r*—recalculated LFs of Hu et al. (2004), *A04*—Ajiki et al. (2004), *M04*—Malhotra & Rhoads (2004), *A03*—Ajiki et al. (2003), and *R01*—Rhoads & Malhotra (2001). We recalculate the LFs of Hu et al. (2004) data, and obtain the points of *H04r* whose values are close to those of the similar re-estimation by Tapken et al. (2006). The arrows in the top and middle panes represent the luminosity range where LFs are dominated by LAEs with AGN activities (see Section 4.6). For the reader’s eye guide, we plot ticks of SFR obtained from eq. (9) on the upper abscissa axis.

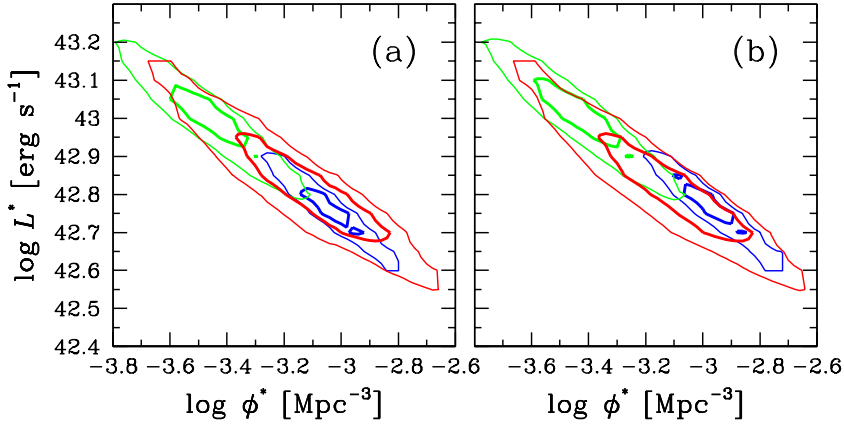


Fig. 20.— Error ellipses of our Schechter parameters, $L_{\text{Ly}\alpha}^*$ and ϕ^* . The left panel shows the ellipses for our observational data, while the right panel presents those for all LAEs with a positive emission ($EW > 0$) estimated by our simulations. Blue, green, and red contours represent $z = 3.1$, 3.7 , and 5.7 LAE-LFs with the fixed slope of $\alpha = -1.5$. Thick and thin lines indicate 1 and 2σ confidence levels, respectively.

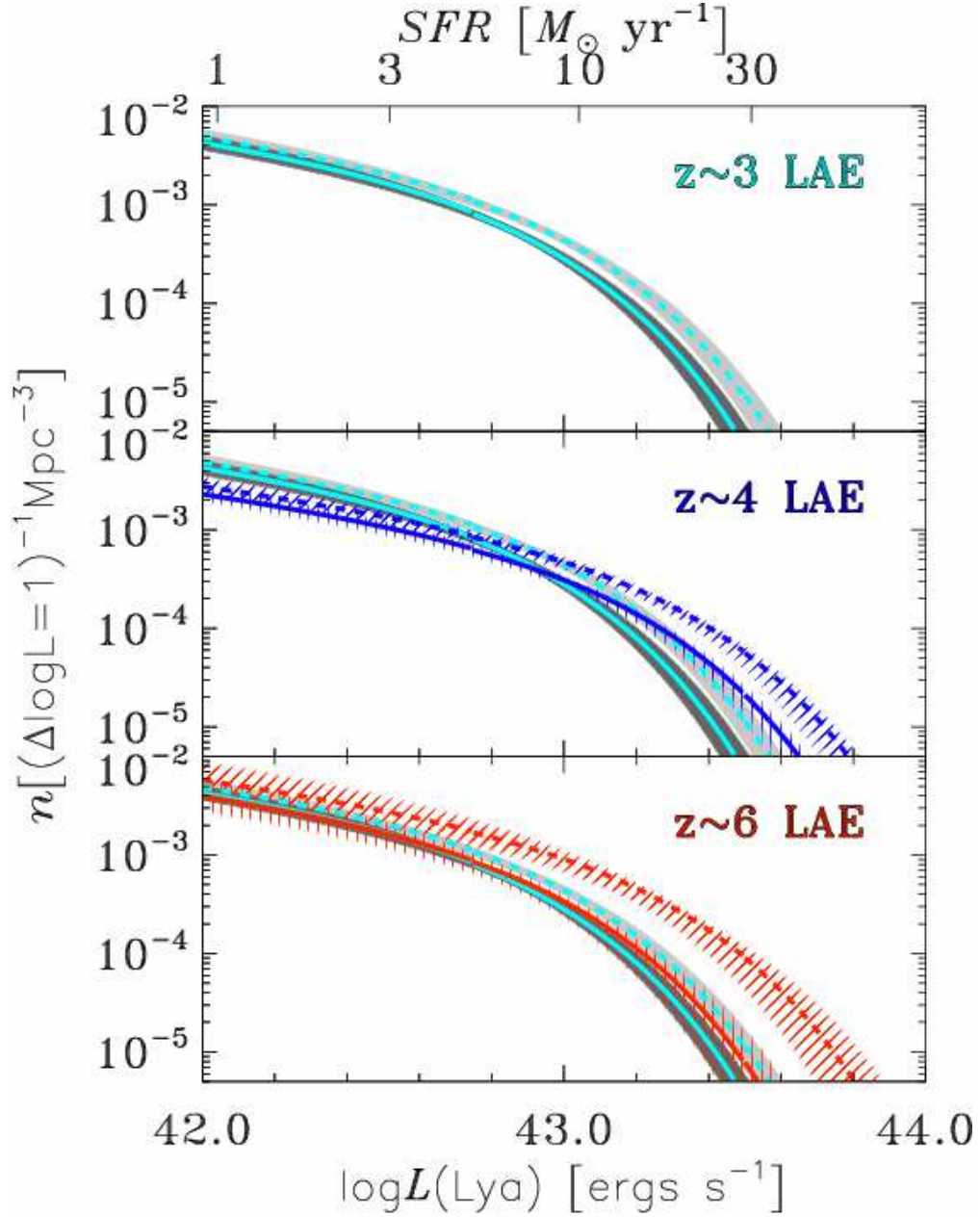


Fig. 21.— Inferred *intrinsic* Ly α luminosity functions (LFs), together with the best-estimate *apparent* Ly α LFs. Dashed- and solid-line curves are the *intrinsic* and *apparent* Ly α LFs, respectively. Cyan, blue, and red curves denote for LFs at $z = 3.1$ (top panel), 3.7 (middle panel), and 5.7 (bottom panel), respectively. Cyan lines are repeatedly plotted at each panel for comparison. Light-gray and gray shades around cyan lines indicate 1σ errors of *intrinsic* and *apparent* Ly α LFs at $z = 3.1$. Areas of vertical and hatched lines are the same, but for $z = 3.7$ (blue) and 5.7 (red) in the middle and bottom panels, respectively.

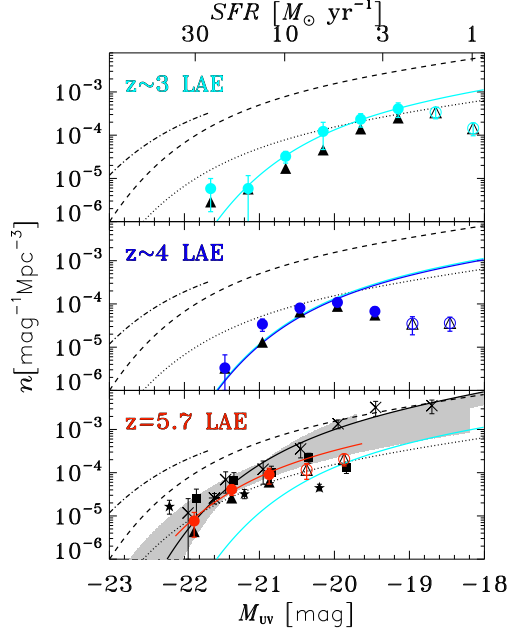


Fig. 22.— The UV luminosity functions (LFs) of LAEs at $z = 3.1 - 5.7$. The cyan, blue, and red circles indicate the best-estimates of LFs for our $z = 3.1$ (top panel), 3.7 (middle panel), and 5.7 (bottom panel) LAEs. The solid lines represent the best-fit Schechter functions for the best estimates. The best-fit Schechter function of $z = 3.1$ LAEs is presented on each panel for reference. The triangles are the lower limits of these LFs at each redshift that are derived with the aperture photometry of broad-band images (see text). For circles and triangles, we show the reliable and less-reliable measurements with filled and open symbols, which are obtained with UV magnitudes at $> 5\sigma$ and $2 - 5\sigma$ levels, respectively. We only use these $> 5\sigma$ data (filled circles) for our Schechter-function fit (see text). The filled squares and stars on the bottom panel are the UV LFs of LAEs at $z = 5.7$ obtained by Shimasaku et al. (2006) and Hu & Cowie (2006). On each panel, we also plot the UV LFs of dropout galaxies for comparison. The dashed and dot-dashed lines are the $z = 3$ LFs of Steidel et al. (1999) and (Paltani et al. 2006), respectively. The dotted line indicates the $z = 3$ LF of Steidel et al. (1999), but ϕ^* of the LF is multiplied by $1/10$. Note that the LF of $z = 4$ dropout galaxies are almost same as that of $z = 3$ (Steidel et al. 1999; Ouchi et al. 2004a; Beckwith et al. 2006; Yoshida et al. 2006). On the bottom panel, we show the UV LFs of dropout galaxies at $z \sim 6$ with crosses (Bouwens et al. 2006) and asterisk (Shimasaku et al. 2006). The gray region on the bottom panel indicates the range of the best-fit Schechter functions for i -dropouts obtained by various studies (Bunker et al. 2004; Yan & Windhorst 2004; Malhotra et al. 2005; Bouwens et al. 2006), which show the uncertainties of measurements for $z = 6$ dropout LF. For the reader’s eye guide, we plot ticks of SFR obtained from eq. (10) on the upper abscissa axis.

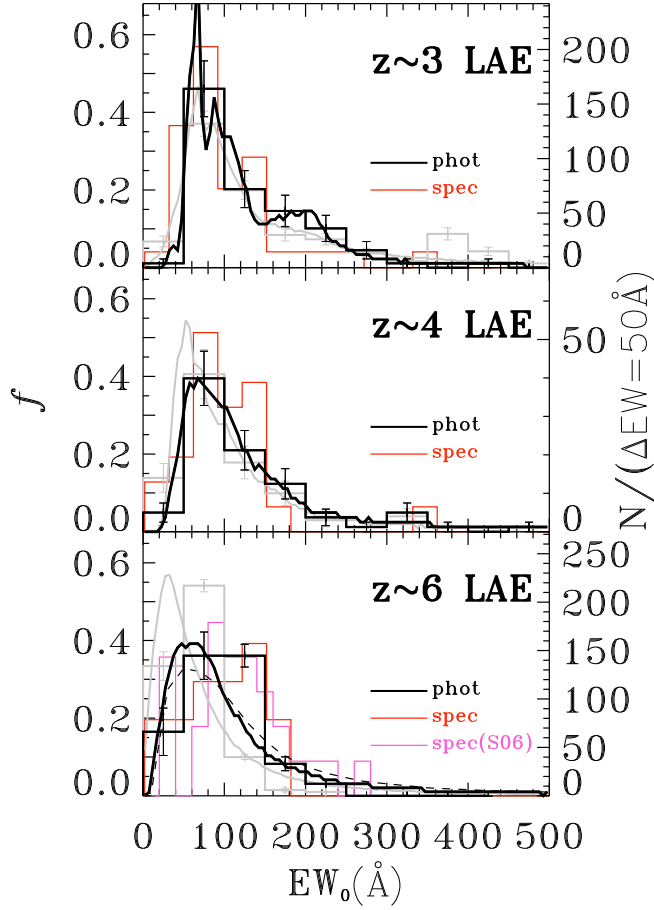


Fig. 23.— Histogram of the rest-frame Ly α equivalent widths (EW) for our LAEs at $z = 3.1$ (top), 3.7 (middle), and 5.7 (bottom). The black histograms and curves represent the best-estimate EW_0 and the EW_0 probability distribution estimated from errors of measurements, respectively, for photometrically selected LAEs with $\log L(\text{Ly}\alpha) \gtrsim 42.6$ and $EW_0^{\text{int}} \gtrsim 70\text{--}80$. The gray histograms and curves are the same, but for all the photometrically selected LAEs. The ticks of vertical axes indicate a fraction (left-hand side) and the number (right-hand side) in a bin size of $\Delta EW = 50\text{\AA}$. The right-hand ticks correspond to the number of all the photometrically selected LAEs. The red histograms present the EW_0 distribution of our spectroscopically identified LAEs. On the bottom panel, the magenta histogram and black dashed line show the best-estimate EW_0 and the EW_0 probability distribution for $z = 5.7$ LAE sample obtained by DEIMOS spectroscopy in the Subaru Deep Field (Shimasaku et al. 2006).

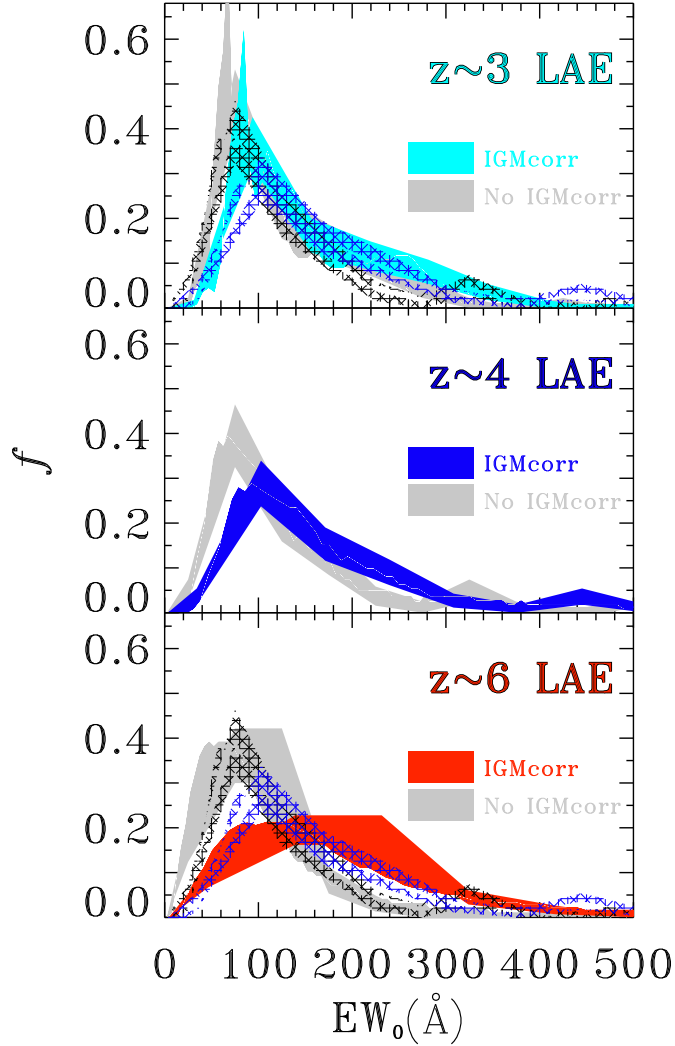


Fig. 24.— Same as Figure 23, but for the comparison of histograms for apparent (“No IGMcorr”) and intrinsic (“IGMcorr”) EW_0 from $z = 3.1$ to 5.7. At each panel, the gray region indicates the apparent EW_0 histogram with uncertainties whose area corresponds to the allowed parameters of the black curves and lines (+error bars) of Figure 23. The cyan, blue, and red areas are the same as the gray regions, but for intrinsic EW_0 corrected for the IGM absorption, assuming the average Ly α opacity (see text). For comparison, we repeatedly plot the $z \sim 4$ gray and blue areas with the black and blue meshes, respectively, on the top and bottom panels.

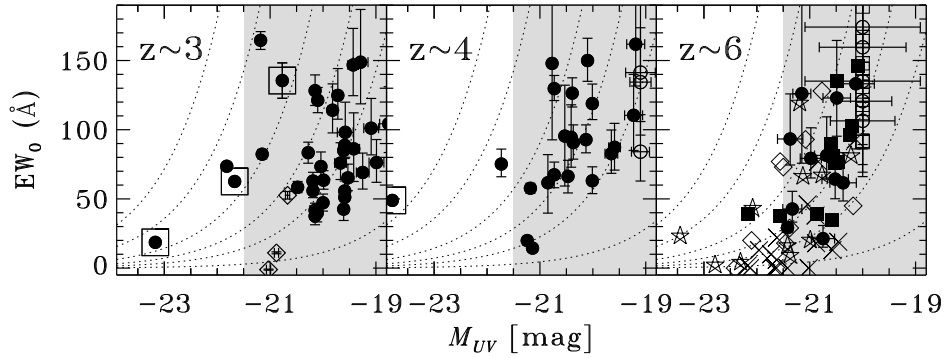


Fig. 25.— Rest-frame equivalent width (EW_0) as a function of UV magnitude for $z \sim 3$ (left), 4 (middle), and 6 (right) objects. Filled and open circles plot our spectroscopically identified LAEs with a UV magnitude brighter and fainter than our 3σ limits, respectively. The filled circles marked with an open square indicate LAEs with AGN activities. On the left panel, we show EW_0 values of $z \sim 3$ dropout galaxies obtained by Shapley et al. (2003), which are the average of the four subsamples of Steidel et al. (2003). On the right panel, the filled squares represent $z = 5.7$ LAEs of Shimasaku et al. (2006). The stars and diamonds present EW_0 of $z \sim 6$ dropout galaxies from Stanway et al. (2007) and the compilation of Ando et al. (2006). The crosses plot EW_0 of $z \sim 5$ dropout galaxies presented in Ando et al. (2006). The dotted lines are loci of the constant Ly α luminosity for 10^{44} , 5×10^{43} , 2×10^{43} , 10^{43} , 5×10^{42} , and 1×10^{42} erg s $^{-1}$ from top left to the bottom. The shaded regions present the magnitude range with EW-large emitters ($M_{UV} \gtrsim -21.5$), which is claimed by Ando et al. (2006).

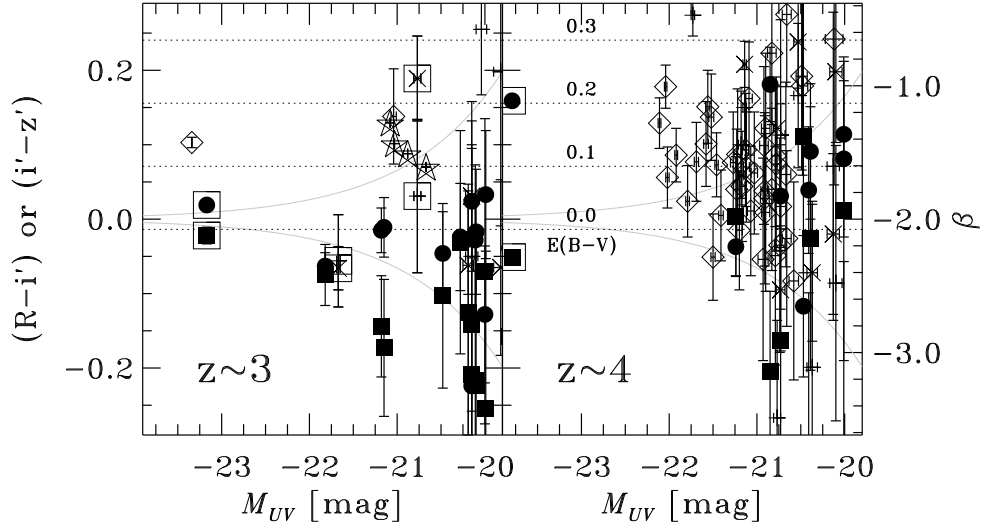


Fig. 26.— UV-continuum color as a function of UV magnitude at $z \sim 3$ (left panel) and $z \sim 4$ (right panel). The filled squares indicate a $i' - z'$ color of our LAEs at $z = 3.1$ and 3.7 from our spectroscopic samples. The filled circles are the same, but for a $R - i'$ color. For confused LAEs whose photometry appears to be contaminated by neighboring objects on a broad-band image, we use plus signs and crosses instead of filled squares and circles, respectively. We mark LAEs with AGN activities with a large open square. The diamonds plot $i' - z'$ colors of spectroscopically identified LBGs (Yoshida et al. 2006). The star marks on the left panel represent the average colors of LBGs obtained by Shapley et al. (2003). We estimate $i' - z'$ colors of Shapley et al.’s data with $E(B - V)$ and the eq. 12. The vertical axis on the right-hand side shows the UV-slope index, β , that corresponds to $i' - z'$ colors at $z \sim 4$. Note that this β is based on the original definition (See Calzetti 2001), which is different from β_{iz} defined by Ouchi et al. (2004a). The difference of β values between $R - i'$ and $i' - z'$ colors is only $\lesssim 7\%$ in the color range of $-0.3 - 0.3$. The $E(B - V)$ values corresponding to the UV colors are indicated with dotted lines. The gray curves represent the size of $\pm 1\sigma$ error for a continuum-flat ($f_\nu = \text{const}$) object.

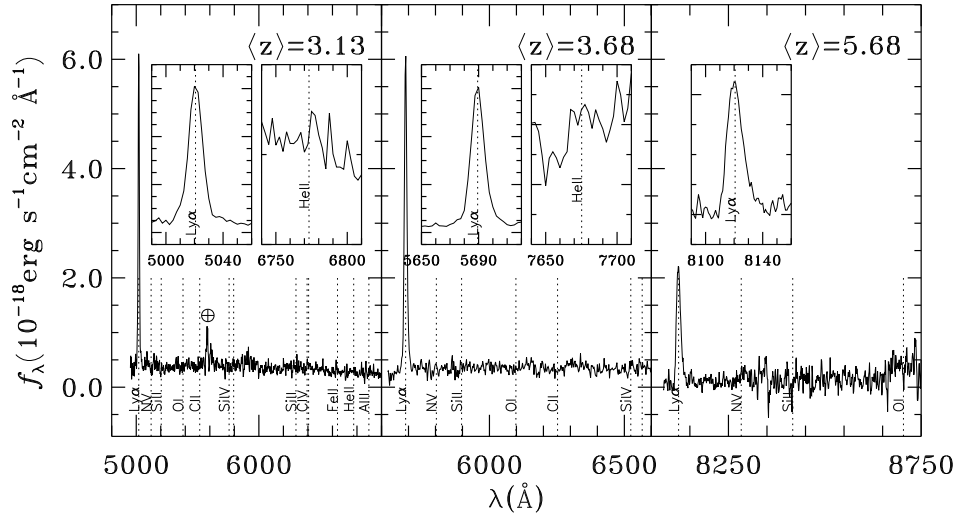


Fig. 27.— Composite spectra of our LAEs at $\langle z \rangle = 3.13$ (left), 3.68 (middle), and 5.68 (right). The dotted lines indicate the wavelengths of interstellar absorption from star formation, or high ionized emission lines from AGN activities. The plots of spectrum are magnified in the inset boxes for wavelength ranges of Ly α (left) and HeII (right). For the $\langle z \rangle = 5.68$ LAE, we only show the inset box of Ly α , since our spectrum does not cover the wavelength of HeII emission for $z = 5.7$ objects.